Dissertation

submitted to the
Combined Faculties of the Natural Sciences and Mathematics
of the Ruperto-Carola-University of Heidelberg, Germany
for the degree of
Doctor of Natural Sciences

Put forward by
Benjamin Michael Dieter Erk, M.A.
born in: Würzburg, Germany
Oral examination: 2013/01/09

Fragmentation Dynamics of Small Molecules upon Multiple Ionization by X-Ray Free-Electron Laser Pulses

Referees: Prof. Dr. Joachim Ullrich

Prof. Dr. Andreas Wolf

Abstract

Fragmentation Dynamics of Small Molecules upon Multiple Ionization by X-Ray Free-Electron Laser Pulses

The ionization and fragmentation dynamics of small molecules (CH_3SeH, C_2H_5SeH, CH_3I, and ICl) triggered by intense ultrashort soft X-ray pulses delivered by the Linac Coherent Light Source are investigated employing coincident three-dimensional ion momentum spectroscopy.

This work aims at investigating the role of the molecular environment in multiple inner-shell photoionization and the accompanying electronic relaxation processes by studying molecular systems containing a single constituent of high nuclear charge Z, i.e. selenium or iodine, such that photoabsorption is almost exclusively localized at the core-shells of these heavy atoms. By comparing the level of ionization for the molecules containing selenium or iodine with results on isolated krypton and xenon atoms, signatures of efficient charge redistribution within the molecular environment are observed. Measured kinetic energies and angular distributions of the ionic fragments in comparison to the outcome of a simple Coulomb explosion model allow tracking down the evolution of the molecular geometry, revealing considerable displacement of the nuclei on the time scale of sequential multiple ionization. The results obtained have considerable implications for coherent diffractive imaging, providing a direct measure of radiation damage (displacement of nuclei and electronic rearrangement) on the time scale of the X-ray pulse and the length scale of the individual atoms.

Fragmentierungsdynamik kleiner Moleküle nach mehrfacher Innerschalenionisation durch Röntgenpulse eines Freie-Elektronen-Lasers

Im Rahmen dieser Arbeit wird die Fragmentierung kleiner Moleküle (CH_4SeH, C_2H_6Se, CH_3I und ICl) nach mehrfacher Innerschalenionisation durch ultrakurze Röntgenpulse der Linac Coherent Light Source mittels dreidimensionaler Ionen-Impulsspektroskopie untersucht.

Ziel dieser Arbeit ist es, den Einfluss der molekularen Umgebung auf die mehrfache Ionisation und die elektronischen Zerfallsprozesse zu bestimmen. Hierzu werden Moleküle untersucht, welche genau ein schweres Atom wie Jod oder Selen enthalten. Diese Elemente besitzen, im Vergleich zu den leichteren molekularen Bestandteilen, einen um ein Vielfaches höheren Absorptionsquerschnitt. Dies bewirkt, dass die Absorption nahezu ausschließlich in den inneren Schalen dieser schweren Atome stattfindet. Durch den Vergleich der erzeugten Ladungszustände im Molekül und jener in einzelnen Edelgasatomen (Xe, Kr), welche vergleichbare Innerschalen-Elektronenkonfigurationen und Absorptionsquerschnitte haben, werden Signaturen von Ladungsumverteilung im Molekül deutlich. Die kinetischen Energien der ionischen Fragmente sowie deren Winkelverteilungen geben in Kombination mit Simulationen Aufschluss über die sich ändernde Geometrie des Moleküls. Sie zeigen, dass eine deutliche Bewegung der Kerne bereits auf der Zeitskala der mehrfachen Photonenabsorption einsetzt. Diese Resultate sind unter anderem relevant für Coherent Diffractive Imaging-Anwendungen, da sie eine direkte Abschätzung des herbeigeführten Strahlenschadens in Form von Bewegungen von Elektronen und Kernen auf der Zeitskala des Röntgenpulses und der Größenskala einzelner Atome liefern.

Contents

List of Figures

List of Tables

Chapter 1

Introduction

Since the discovery of a "new form of radiation" by W.C. Röntgen in Würzburg in 1895 [1], X-rays have been successfully utilized for structural investigations of matter. In the early days, people were fascinated by the ability to image bones in a living human hand through tissue and muscles. Soon, this groundbreaking new invention manifested itself as an application in science and everyday life and until today, X-rays play a major role in modern medicine [2].

Due to their high photon energy, and correspondingly, very small wavelength, X-rays represent an excellent tool for direct imaging of matter on the length scales of atomic structure, which is on the order of 1 Å (10^{-10} m), as is illustrated in figure 1.1. This was realized as early as 1912, when pioneering studies of M. von Laue, W.H. Bragg, W.L. Bragg and others revealed the unique capabilities of X-rays for the analysis of crystalline structures. The key idea was to add up weak X-ray scattering from the individual objects (atoms) of a periodic assembly of the sample to obtain a measurable integrated signal. First experiments employed diffraction on single crystals [3], and were later extended towards powder diffraction by P. Debey and P. Scherrer [4]. Since then, X-ray diffraction gradually developed into an indispensable technique for structure determination in a broad range of disciplines, from condensed matter physics to biology, and created most of our current knowledge on macromolecular structures including such milestone findings as the discovery of the double-helix shape of DNA in 1953 [5].

Besides crystallographic imaging applications, X-rays proved to be a unique tool for studying the electronic structure of matter and its chemical composition. Throughout the 20th century, a variety of techniques exploiting X-ray scattering, absorption

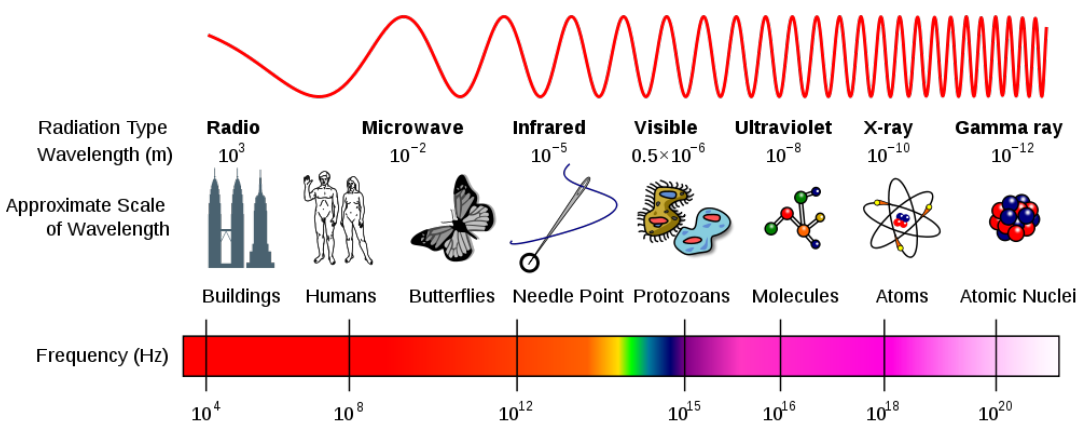

Figure 1.1: The electromagnetic spectrum with an overview of the wavelength and the corresponding size of typical objects (taken from reference [6]).

or emission (fluorescence) [7, 8, 9], as well as photoionization-based methods such as photoelectron spectroscopy [10] have been developed for studies of single atoms, molecules and extended liquid or condensed matter systems. These techniques benefit from the fact that X-rays at a given wavelength predominantly interact with a particular electronic shell of a specific atom. This site- and shell-specificity allows studying the electronic structure of the isolated atom and then to find specific signatures of this structure in different chemical environments, providing the basis for various chemical and solid-state analysis methods.

Technologically, the field of X-ray science advanced dramatically with the advent of accelerator-based synchrotron light sources [11]. These machines deliver X-ray photon beams much more intense than all previous X-ray sources such as X-ray tubes, and are readily tunable over a broad range of wavelengths. Therefore, a large portion of today's frontier X-ray research is carried out at synchrotron radiation facilities located all around the world.

In the first decade of the 21st century, a new generation of accelerator-based X-ray sources, X-ray Free-Electron Lasers (XFELs) were developed. XFELs combine the short wavelength range and tunability of synchrotron sources with a huge increase in photon numbers per pulse, shorter pulse durations, and add the coherence of optical lasers, thus delivering femtosecond X-ray bursts with a peak brilliance that is nine orders of magnitude higher than found at modern synchrotrons. Among numerous potential scientific and technological applications opened up by these new facilities, their development was especially motivated by the concept of coherent diffraction

imaging of non-crystalline objects and the opportunities of ultrafast time-resolved experiments with X-rays.

Two basic limitations of conventional X-ray crystallographic imaging are, on the one hand, radiation damage (i.e., a change in the electronic structure and the nuclear positions) induced by X-ray photons and, on the other hand, the necessity to grow crystals large enough to provide an interpretable integrated signal without exceeding the damage threshold. It was suggested in [12, 13] that XFEL pulses can deliver enough photons to generate a diffraction signal from a single non-crystalline macromolecule within an ultrashort time window, such that all radiation damage phenomena occur only after the image is already obtained. If successful, this "diffract before destroy" approach has the potential to revolutionize structural biology and to make a large impact on material science. At the same time, ultrashort (femtosecond) pulse durations of XFELs allow combining time-resolved techniques developed in modern femtochemistry based on optical lasers, with the unique imaging capabilities of X-rays, thus, nurturing the dream of producing a "movie" of molecular reactions on their natural ("atomic") length and time scales.

The world's first X-ray FEL, the Linac Coherent Light Source in Stanford, has been commissioned in 2009. During the first years of operation, numerous exciting studies, including proof-of-principle coherent diffraction imaging experiments on single nanoscale particles [14, 15, 16, 17] have been performed. It was shown that the use of intense and ultrashort X-ray pulses drastically reduces the size of the crystals necessary to obtain an image by X-rays, opening a new field of femtosecond nanocrystallography [18, 19, 20]. However, the limits in resolution set by the radiation damage [21, 20] as well as the feasibility and limitations of single-particle imaging are still the subject of active studies. Here, the key issues are the mechanisms and time scales of radiation damage on the atomic scale. Therefore, in parallel to the developments in X-ray imaging techniques, measurements aimed at understanding the behavior of simple systems such as isolated atoms [22, 23, 24], diatomic molecules [25, 26, 27] and small rare gas clusters [28] were conducted at the LCLS. These experiments revealed novel effects such as double or multiple core-hole creation and frustrated X-ray absorption [22, 25, 26, 27, 28], and showed that very high levels of ionization can be achieved (e.g., up to 36+ in xenon atoms [24]).

In a way, these experiments on small quantum systems represent an extension of the inner-shell X-ray photoionization studies on atoms and molecules, performed at

synchrotron facilities over the last few decades, into the new regime of multi-photon interactions. Although the possibility to absorb more than one photon to release a bound electron from an atom was theoretically predicted by M. Göppert-Mayer already in 1931 [29] and has been extensively studied in the infrared, optical, and ultraviolet spectral regions since the development of lasers in the beginning of 1960s [30], it was until very recently, never observed in the X-ray domain because of the limited peak intensities of the available radiation sources. At XFELs however, the multi-photon processes represent the dominant light-matter interaction mechanisms and, thus, are decisive for understanding matter response and damage phenomena. In polyatomic systems, multi-photon absorption, electronic relaxation upon inner-shell ionization, and nuclear motion in the course of photo-induced fragmentation all proceed on comparable (femtosecond) time scales, resulting in complicated and interweaved many-particle dynamics.

In this work, the ionization and fragmentation dynamics of small molecular systems irradiated by intense LCLS pulses are investigated. The highly-ionized molecules dissociate via a multitude of different pathways, producing several ionic fragments which carry information reflecting both, initial molecular geometry, as well as ionization and relaxation dynamics. In this work, these fragments are detected in coincidence using a 3D-momentum imaging spectrometer, thus determining the final charge state of the entire system, as well as charge states, kinetic energies, and emission angles of individual ions.

For this study, molecules containing a single high-Z constituent, namely selenium or iodine, represent ideal benchmark systems for several reasons. First, the large photoabsorption cross section of heavy atoms increases the total number of photons absorbed, allowing to focus on novel multi-photon effects. Second, and most important, because of the large difference in the absorption cross section between the high-Z constituent and the rest of the molecule, the initial photoabsorption is localized on this atom, allowing to study subsequent charge redistribution mechanisms and the role of the molecular environment. Finally, theoretical studies for coherent diffractive imaging with intense X-FEL pulses [31] predict that the enhanced local radiation damage in the vicinity of heavy atom constituents might significantly disturb the interpretation of diffraction data [20].

Comparing the charges induced in the molecules containing selenium and iodine with the charge levels measured for isolated krypton and xenon atoms, which have

similar inner-shell electronic configuration and absorption cross sections, it is found that a significant part of the total charge induced in the molecule is redistributed from the absorbing atom to the molecular environment. The experimental results suggest that at least part of this charge rearrangement occurs on a very short time scale. From the measured kinetic energies of the ionic fragments and from the experimental determination of the number of photons absorbed by the system, it is concluded that the atomic nuclei are considerably displaced on the time scale of the ionization process defined by the pulse duration and the lifetimes of the inner-shell vacancies with respect to electronic relaxation processes such as Auger decays. These results clearly indicate that all imaging schemes aimed at "outrunning" radiation damage effects require ultrashort pulses of few femtosecond duration, and that local "hot spots" of increased radiation damage in the vicinity of high-Z atoms (Z: nuclear charge; e.g., iron or sulfur impurities in biological systems) have to be taken into account for the interpretation of corresponding imaging data. Finally, it is demonstrated that coincident Coulomb explosion imaging can provide information on the spatial orientation of the molecule even for the case of sequential few-photon induced fragmentation. This can be exploited for determining molecular orientation as a basis for further applications, such as photoelectron spectroscopy in the molecular frame.

This thesis is structured in the following way: In chapter 2, the fundamentals of inner-shell photoionization and subsequent decay processes are discussed for atomic and molecular systems, in particular addressing the role of the molecular environment and molecular fragmentation dynamics triggered by ionization. This discussion is followed by an introduction to the Coulomb Explosion Imaging (CEI) technique for determination of molecular structures, and a Coulomb explosion simulation used for comparison to the experimental data. Chapter 3 describes properties and basic operation principles of the LCLS XFEL, and the CFEL ASG Multi-Purpose experimental endstation (CAMP) used to perform 3D-momentum imaging ion spectroscopy of the molecular fragments. In chapter 4, the experimental results for the four molecular systems, methylselenol, ethylselenol, iodine chloride, and methyl iodide are presented and discussed. Finally, chapter 5 summarizes the findings for all molecular systems studied and provides an outlook into future experiments in this actively evolving field.

Chapter 2

X-Ray Photoionization and Photofragmentation of Small Quantum Systems

The interaction of electromagnetic radiation with matter may result in the ejection of one or a few bound electrons into the continuum, which is called photoionization. It can be caused by the absorption of a single photon with sufficient energy, or by many low-energy photons. At high photon energies of 100 keV and higher, inelastic Compton scattering dominates. In molecules, photoionization often leads to the breakup of the system into few constituents, a process called photodissociation or photofragmentation. The resulting electrons and ions carry information about the initial state of the system, such as electronic structure, composition of the sample, chemical binding etc., as well as about the dynamics of the (multiple) ionization process. Therefore, photoionization studies have nowadays become a powerful research tool in atomic, molecular, and condensed matter physics, physical chemistry, and material sciences.

Ionization induced by single-photon absorption has been the subject of extensive studies using, at first, tabletop VUV and X-ray sources and later tunable synchrotron radiation, whereas multi-photon processes were, until recently, observed only at lower photon energies, mostly using intense optical or infrared lasers. A new generation of accelerator-based light sources, Free-Electron Lasers (FELs), which combine the high photon energies of synchrotron sources with the huge photon numbers and short pulse durations of modern optical laser systems, have now made

multi-photon multiple ionization in the XUV and X-ray regimes experimentally accessible. New physical processes that occur when matter interacts with short-pulsed high-frequency radiation of unprecedentedly high-intensity are under extensive experimental and theoretical investigation.

Fundamental processes triggered by the absorption of a single X-ray photon in atomic systems will be overviewed in section 2.1.1 through 2.1.3, whereas their extension into the new regime opened up by XUV and X-ray FELs will be described in section 2.1.4. It is followed by the discussion of molecular effects, in particular X-ray induced fragmentation of molecules, in section 2.2. The specific technique of Coulomb Explosion Imaging, employed to determine molecular structure and orientation, will be presented in section 2.3, including the description of a computer simulation used to model the Coulomb explosion of small molecules in section 2.3.1.

2.1 Photoionization of Atomic Systems

The simplest system in atomic physics is a hydrogen or hydrogen-like atom. It consists of a nucleus and an electron of mass m_e that is bound by the Coulomb force. The time-independent Schrödinger equation describing the wavefunction ψ of the electron and, thus, also the stationary states or orbitals of such a hydrogen system can be written in the following way, assuming the nucleus to have an infinite mass:

$$H\psi(r,\theta,\phi) = \left(-\frac{\hbar^2}{2m_e}\Delta^2 - \frac{e^2}{4\pi\epsilon_0 r}\right)\psi(r,\theta,\phi) = E\psi(r,\theta,\phi) \tag{2.1}$$

Here, ψ is given in spherical electronic coordinates r, θ, and ϕ; $\hbar$ is Planck's constant; e is the electron charge; ϵ_0 is the dielectric constant; E are the system's eigenvalues; and Δ^2 is the Laplacian operator. The wavefunction ψ can be written as:

$$\psi(r,\theta,\phi) = R_{n,l}(r)\; Y_l^{m_l}(\theta,\phi) \tag{2.2}$$

using a wavefunction that is separated into a radial part, $R_{n,l}(r)$, and an angular part, $Y_l^{m_l}(\theta,\phi)$. With this ansatz, the hydrogen atom can be described by three independent quantum numbers n, l, m_l. While the radial part $R_{n,l}$ is given by the principal quantum number n and l, the spherical harmonics $Y_l^{m_l}$ depend on the angular momentum quantum number l and the magnetic quantum number m_l. The total angular momentum also depends on the spin quantum number m_s, which is the

z-component of the electron angular spin and which can be derived from a relativistic treatment of the problem.

It is common to denote the principal numbers $n = 1, 2, 3, ...$ by K, L, $M, ...$, respectively, and the angular momentum number $l = 0, 1, 2, 3, ...$ by $s, p, d, f, ...$ The magnetic quantum number can have values $m_l = 0, \pm 1, \pm 2, \pm 3, ..., \pm l$ whereas the spin quantum number can be $m_s = \pm 1/2$.

These quantum numbers define the so-called *atomic orbitals*,and the square of the corresponding wave function yields the probability of finding an electron in this specific state. As part of the *atomic orbital model*, they represent the basic building blocks that can be used to construct (in approximation) the electron cloud of a multi-electron atom.

However, with multiple electrons in the system, each of the N_e electrons interacts with the attractive Coulombic potential of the nucleus plus the repulsive potential of the other electrons. This can be accounted for in the Schrödinger equation by adding electron correlation terms. An exact solution of this equation however is not possible, but approximation methods like, for example, (many-body) *perturbation theory* within the central field approximation [32] can provide solutions with an accuracy that is sufficient in many cases. Nevertheless, it is an active field of research being of paramount importance in astrophysics to benchmark atomic structure codes by experimental precision data [33] in order to interpret high-resolution spectra of astrophysical objects. A common way to obtain many-electron wavefunctions for electrons in the ground states of atoms is the *Hartree-Fock-Slater method* [34].

2.1.1 The Process of Photoionization

When an atom absorbs a photon of energy $E_\gamma = \hbar\omega$, with the angular frequency ω and the Planck constant $\hbar$, the electronic system can either undergo a bound-bound transition between the initial E_i and the final (many-electron) energy level E_f that fulfills the condition $E_i - E_f = \hbar\omega$ or, if the photon energy exceeds the atomic ionization potential, an electron is emitted into the continuum with the excess kinetic energy $E_{kin} = \hbar\omega - E_i$, assuming that all remaining electrons are left in their initial state.

For bound-bound transitions with a discrete energy interval ΔE around $\hbar\omega = E_i - E_f$ the so called *linewidth* ΔE is connected with the lifetime Δt of the final

bound state by the *Heisenberg uncertainty principle*:

$$\Delta E \Delta t \geq \hbar/2 \tag{2.3}$$

or, in units commonly used in spectroscopy:

$$\Delta E[\text{eV}] \Delta t[\text{fs}] \geq 0.659 \tag{2.4}$$

These transitions are also called *resonances*. Denoting the binding energy of an electron in a specific orbital of a many-electron atom with E_{bind}, the density of resonances becomes very high as the photon energy approaches E_{bind} with the electron being excited into the corresponding *Rydberg series*. Above this energy, the ever closer spaced states merge into a continuum.

Atomic photoionization can be described by the total photoionization cross section $\sigma(\omega)$, the partial photoionization cross section $\sigma_i(\omega)$, and the angular anisotropy parameters $\beta_i(\omega)$, where i stands for the quantum numbers of the ionized electron in a certain sub-shell of the atom [35]. The cross section is defined as the number of ionized electrons per unit time divided by the number of incident photons per unit time per unit area and, thus, has the dimension of length squared – usually given in cm^2 or barn ($1\text{cm}^2 = 10^{24}\text{barn}$). Total and partial cross sections are connected by $\sigma(\omega) = \sum_i \sigma_i(\omega)$ [36]. The angular anisotropy β is of crucial importance for many investigations of ionization in atomic and molecular systems, but in this work it will not be further discussed as it plays a minor role in the interpretation of the results presented here.

The interaction of a bound electron with the electromagnetic field whose vector potential is $\vec{A}$ can be approximated by the operator $\frac{i\hbar e}{m_e}\vec{A}\vec{\nabla}$ neglecting strong-field terms proportional to $\vec{A}^2$. Within time-dependent perturbation theory and using the dipole approximation for the QED single photon absorption part of $\vec{A} \sim e^{i\vec{k}\vec{r}-\omega t} \approx 1$ one obtains for the partial photoionization cross section in a one-electron picture in atomic units:

$$\sigma_i(\omega) = \frac{4\pi^2}{\omega c} |\left\langle \psi_f | \vec{r} | \psi_i \right\rangle|^2 \tag{2.5}$$

with the one-electron wavefunctions[1] of the initial state ψ_i and final state ψ_f [35].

[1] Using $\left\langle \psi_f | \vec{\nabla} | \psi_i \right\rangle \propto \left\langle \psi_f | \vec{r} | \psi_i \right\rangle \approx \langle \psi_f | \vec{r} | \psi_i \rangle$.

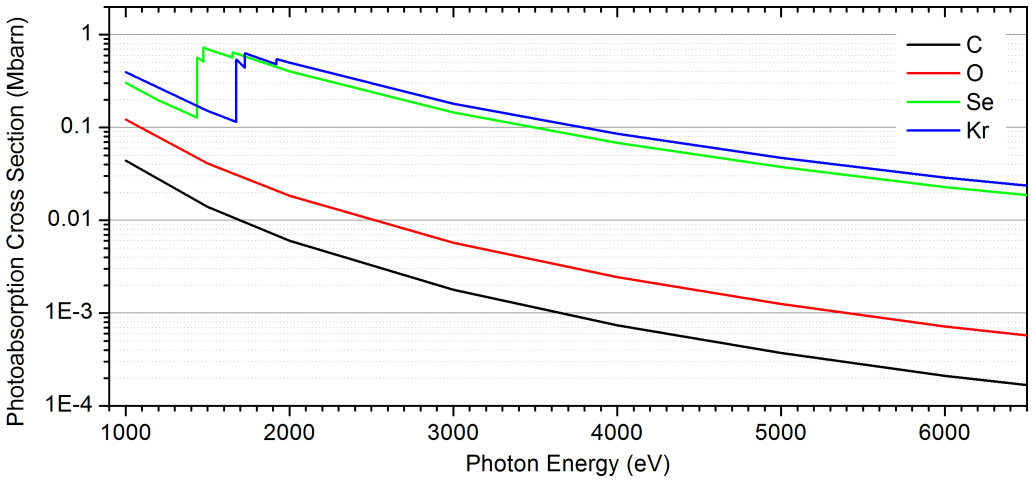

Figure 2.1: Total photoabsorbtion cross sections of atomic oxygen, carbon, selenium, and krypton. Note that the total cross section is the sum of all partial cross sections (not shown) for the individual shells of the atom. Data taken from reference [37].

2.1.2 X-Ray Ionization

With respect to the photon energy needed to ionize an atom, valence electrons are easiest to free into the continuum. This makes valence ionization accessible with for example ultra-violet (UV) tabletop lasers.

With photons of higher energy, inner-shell electrons of atoms become accessible with single photons. The energies required to ionize these electrons range from 55 eV photons for (1s) ionization in lithium, to energies beyond 10^5 eV for (1s) ionization of heavy atoms with atomic number $Z > 90$. Thus, sources with higher photon energies than those provided by tabletop lasers, e.g. X-ray tubes and synchrotrons are needed.

Generally, the photoionization cross section decreases with increasing photon energy, not taking into account the specific absorption edges. Also, the cross section is higher for higher-Z atoms. This can be seen from total photoabsorption cross sections of carbon, oxygen, selenium, and krypton in figure 2.1.

At certain energies corresponding to the ionization potential of particular electronic shells, the cross section increases significantly, forming a series of absorption edges for many electron atoms. The photoabsorption cross section is an atom specific property and the general shape away from the edges can be described with the

use of the empirical *Victoreen formula*

$$\mu(E) = cE^{-3} + dE^{-4} \tag{2.6}$$

where c and d are shell and atom specific fit parameters (see reference [38]).

Because of the strong energy dependency of the photoabsorption cross section, the photon energy can often be tuned to ionize mostly one specific electronic shell of a certain atom. Combined with the energy tunability of accelerator-based light-sources, this makes X-rays a unique tool for studying shell-specific excitation and ionization. The selectivity of photoionization and the possibilities this offers for molecular spectroscopy play an important role in this work and will be discussed in section 2.2.1.

2.1.3 Decay Processes

After X-ray photoionization, the atom has an inner-shell vacancy and is in a highly excited state. There are usually a variety of energy dissipation or decay processes that are energetically possible. In these relaxation processes, the inner-shell vacancy is filled by an outer-shell electron and the difference in binding energy is dissipated mainly via two different and competing mechanisms – fluorescence decay and Auger decay.

Fluorescence Decay, is a radiative decay where an X-ray photon of energy

$$\hbar\omega = E_i - E_f \tag{2.7}$$

is emitted while an electron from an outer-shell of energy E_i fills the inner-shell vacancy at the energy level E_f (see figure 2.2 (a) for an example). In this process, the charge state of the atom remains the same as no further electrons are excited or released into the continuum.

The probability of spontaneous emission of dipole-radiation is:

$$P_{i,f} = \frac{2e^2\omega_{\text{fi}}^3}{3\epsilon_0 hc^3} |\langle\psi_f|\vec{r}|\psi_i\rangle|^2 \tag{2.8}$$

with the dipole-matrix element $\langle\psi_f|\vec{r}|\psi_i\rangle$, where ψ_i and ψ_f are the electronic wave functions of the initial and final states [39]. With the transition energy ω_{fi} scaling

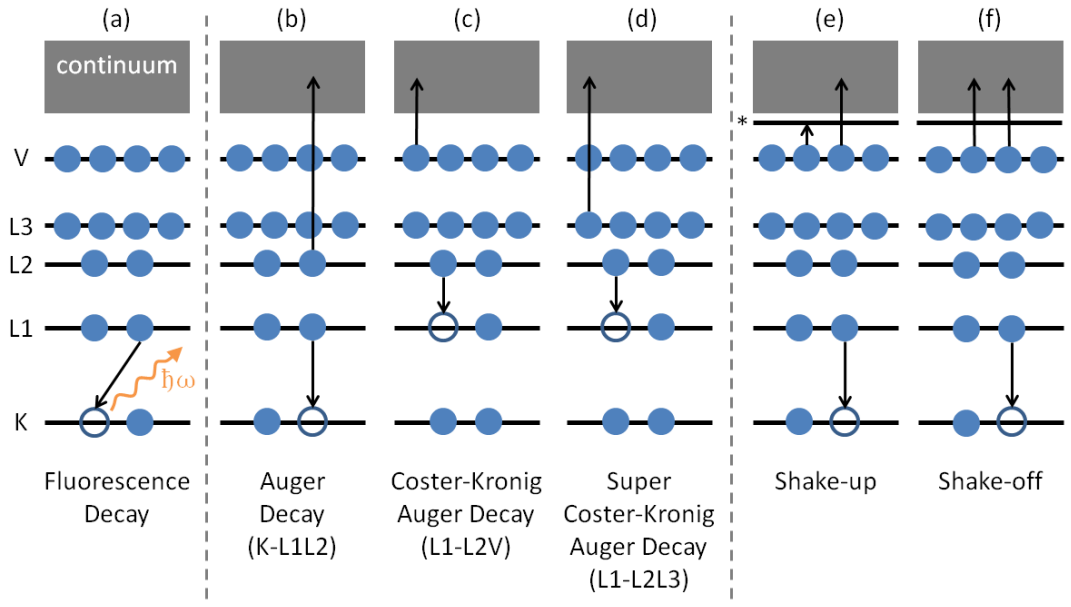

Figure 2.2: Overview of the main de-excitation processes possible after creation of an inner-shell vacancy, namely fluorescence and Auger decay. Also higher-order ionization processes, i.e. shake-up and shake-off, are sketched.

like $\omega_{\mathrm{fi}} \propto Z^2$ for a given dipole-allowed transition and assuming hydrogen-like orbitals with $r \propto 1/Z$ (because of the hydrogenic character of the inner orbitals), the probability scales as $P_{i,f} \propto Z^4$.

Auger Decay is a competing non-radiative relaxation channel. It is the release of a second electron as the transition energy of the electron filling the inner-shell vacancy is transmitted via Coulomb interaction. This second electron is carrying the excess energy

$$E_{kin} = |E_i| - |E_f| - |E_{bind}| \tag{2.9}$$

where E_{bind} is the binding energy of the freed electron.

If the excess energy is not only transformed into kinetic energy of an electron but partly into an additional excitation of an outer-shell electron, this is called a *satellite Auger transition*. For a so-called *double Auger*, the excess energy is enough to release two electrons at the same time.

The Auger decay increases the ion charge state by one, for Auger and satellite Auger, or even by two in the case of double Auger decay. A common way to name these transitions is by giving the shell of the vacancy that is filled, followed by the

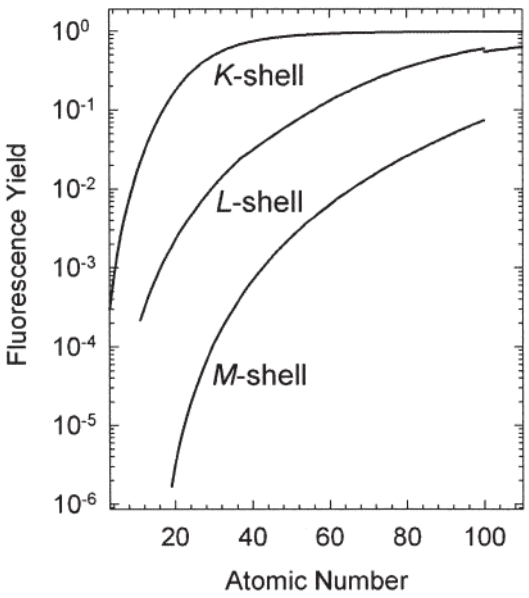

Figure 2.3: Overview of fluorescence-yield dependence on atomic number Z for K-, L-, and M-vacancy decay.[2]

original shell of the electron that is filling and the shell of the electron that is released due to the excess energy. An example of a KLL Auger decay is given in figure 2.2(b).

If the electron vacancy is in the same shell as the electron filling the inner-shell vacancy, and an electron of an outer-shell is released, this is called a *Coster-Kronig decay*, e.g. LLM decay depicted in figure 2.2 (c). If the released electron is also from the same shell, the process is named *Super Coster-Kronig*, e.g. LLL decay in figure 2.2(d). In cases where (super) Coster-Kronig decay is energetically allowed, this is the dominating Auger process and it typically has a much higher transition rate than other energetically possible Auger channels.

Auger transition rates can be calculated within perturbation theory, as they are proportional to the Coulomb-interaction between the involved electrons:

$$P_{i,f} = \frac{4\pi^2}{h} \left| \left\langle \psi_f \left| \frac{e^2}{\vec{r_1} - \vec{r_2}} \right| \psi_i \right\rangle \right|^2 \rho(E_f) \tag{2.10}$$

where $\left\langle \psi_f \left| \frac{e^2}{\vec{r_1}-\vec{r_2}} \right| \psi_i \right\rangle$ is the Coulomb-interaction-matrix element between the initial and final states of two-electron wavefunctions ψ_i and ψ_f; and $\rho(E_f)$ is the density of final states [40, 41]. The Auger transition probability is thus proportional to Z^2. Equation 2.10 shows that the rate is mainly dependent on the overlap of the

involved wavefunctions which also explains the higher probabilities of Coster-Kronig Auger decays over normal Auger decay as it involves two electrons from the same shell. The same is, of course, true for Super Coster-Kronig where the overlap is even higher as all involved electrons are from the same shell.

The ratio of fluorescence decay versus all competing Auger decay channels for core-holes, like for K-shell or L-shell vacancies called the fluorescence yield, is highly dependent on the atomic number Z, as shown in figure 2.3[2]. For example, the fluorescence yield of an L-shell vacancy in krypton is 0.2%, whereas for xenon it is roughly 1%. For light atoms, Auger decay is the dominating de-excitation process. When, however, the system is already ionized to higher charge states, fluorescence decay becomes more likely, whereas Auger-decay is less probable because of the limited number of possible transitions due to the reduced number of involved electrons.

Sometimes the term *autoionization* is also used in this context. It usually refers to the case where an atom is core-excited, rather than ionized, and the excited system decays via an Auger process, releasing an electron.

Shake-Up and Shake-Off Processes The initial direct photoionization, as well as every relaxation process, can be accompanied by excitation or emission of additional electrons whenever energetically allowed. These electrons are either excited to a unoccupied orbital, and the process is called *shake-up*, or they are excited into the continuum – a so-called *shake-off* process (see figures 2.2(e) and (f)).

In the sudden approximation, shake-up or shake-off can be understood in terms of the photoionized state with an inner-shell vacancy being not an eigenstate of the ionic many-electron system, and thus, exhibit overlap with states where one or more electrons are excited or emitted. In certain systems these shake processes can have rates as high as 20% of the primary ionization or excitation process [43, 44].

Other Decay Processes apart from those mentioned above, include many special cases of de-excitation. For example, *resonant Auger decay* happens when an inner-shell vacancy is created by resonant excitation and is filled via Auger decay, e.g. if the initial ionization happens with a photon energy that is on resonance with a bound-bound transition [45]. Resonant Auger processes are often further subdivided into so-called *spectator and participator transitions* where the initially excited electron is

[2]Source: X-ray data booklet [42], third edition (2009), figure 1-2., page 1-28.

either not taking part in the subsequent Auger decay (spectator) or is taking part in form of direct-recombination (participator).

Decay Cascades can happen in cases where an inner-shell vacancy is filled by an electron from another inner-shell. The new inner-shell vacancies can then be filled by the same decay mechanisms as described above until the system is fully relaxed. As all decay mechanisms except fluorescence decay increase the total number of vacancies with each step, Auger cascades can lead to high levels of ionization in only a few steps.

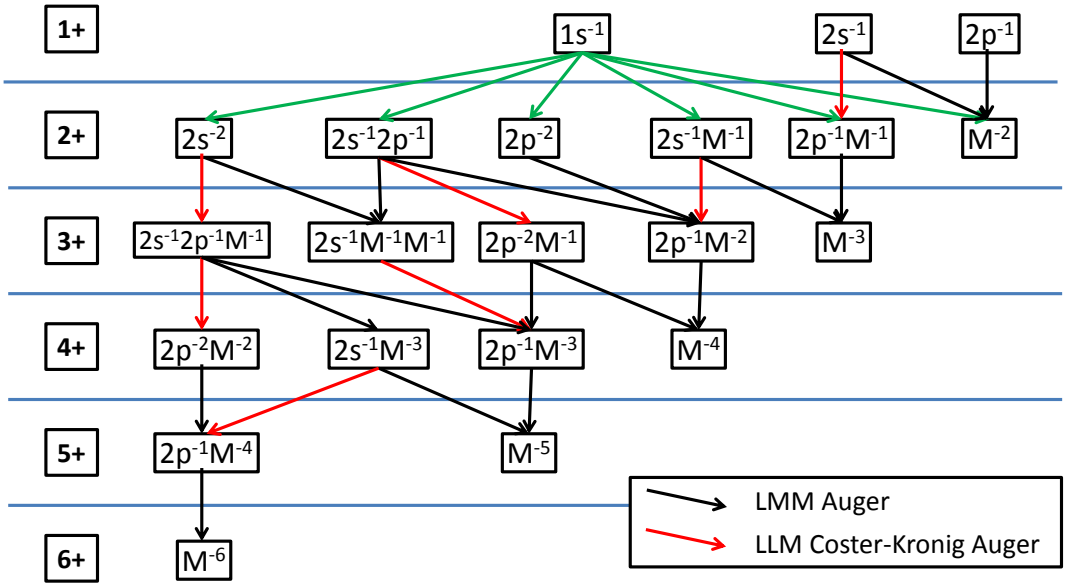

Figure 2.4: Outline of the Auger decay cascade an argon atom undergoes upon (1s), (2s) or (2p) photoionization with the total level of ionization shown on the left.

A cascade in an atom with three main shells, e.g. argon, can be started by a K-shell or L-shell vacancy. These can be filled by several decays involving L- and M-shells, as shown in figure 2.4, ending up in ionization levels of 2+ to 6+. Overall, the removal of a single core-level electron can thus result in a highly charged residual ion, created in a complex relaxation process that can include many pathways. Even higher charge states than shown in figure 2.4 can be reached by above mentioned double Auger or shake-off processes. Many experimental investigations of these interesting many-particle dynamics mechanisms were performed by single photon absorption using X-ray tubes [46] or synchrotron radiation [47].

2.1.4 Multi-Photon Absorption in Intense X-Ray Pulses

Up to now, the interaction of single photons with matter has been discussed. In intense Free-Electron Laser pulses however, in contrary to synchrotron sources, the number of photons per pulse is high enough that higher-order processes involving multiple photons come into play.

By comparing the strength of the electric field that an electron is exposed to in the atom and the field strength of the incoming light-wave, the type of interaction can be classified. This classification is common in the field of intense optical and infrared lasers, where the so-called *Keldysh parameter* is defined as:

$$\boxed{\gamma = \sqrt{\frac{I_P}{2U_P}} => \begin{cases} \gamma >> 1 & \text{multi-photon regime} \\ \gamma << 1 & \text{tunneling regime} \end{cases}} \tag{2.11}$$

where I_P is the ionization potential and U_P is the ponderomotive potential (in atomic units):

$$U_P = \frac{I}{4\omega^2} = \frac{E^2}{4\omega^2} \tag{2.12}$$

with the intensity I, E the electric field, and ω the photon's frequency [48]. This parameter compares the time an electron needs to tunnel out of the atom driven by the electric field of the laser pulse with the duration of the optical cycle of the light wave.

In the regime of optical lasers, the period of the electric field is a few femtoseconds, e.g. 2.7 fs for 800 nm, allowing the electrons in the atom to react to it. Here, one usually discriminates the region of $\gamma > 1$, where the atomic field is dominating the laser field, multi-photon effects dominate and higher-order perturbation theory is still applicable, from the region of $\gamma < 1$, where the atomic potential is treated as a perturbation of the laser field, tunnel ionization dominates, and effects such as recollision, creation of higher-order harmonics etc. can occur.

Today's X-ray FELs are providing intensities of about 10^{15} to $10^{18}\,\mathrm{W/cm^2}$, comparable to those reached with optical lasers, at photon energies of, for example, 1500 eV, corresponding to a frequency of 3.6×10^{17} Hz [22]. Here, the frequency of the light wave is more than 2 orders of magnitude larger than in the optical regime, resulting in a small ponderomotive potential leading to a Keldysh parameter that is much larger than one. In other words, the amplitude of the electric field is large

but the change of the direction of the electric field is happening too fast for the electrons to react. By the classification of the Keldysh parameter, today's X-ray FELs therefore operate in the regime where the picture of multi-photon absorption is adequate.

As mentioned above, the photon absorption process can be quantitatively described by perturbation theory. The absorption of n photons is thereby described by the n-th order perturbation theory. When using a generalized cross section σ_n, a multi-photon non-resonant transition probability can be derived as

$$\boxed{P_{fi}^{(n)} = \sigma_n I^n} \tag{2.13}$$

where I is the intensity and n is the number of photons involved.

The transition rate in a photoionization experiment with N_0 target atoms can be observed as an ion yield:

$$\frac{dN_1}{dt} = N_0 \sigma_n \left(\frac{I}{\hbar\omega} \right)^n \tag{2.14}$$

The yield is thus dependent on the intensity I to the power of n, where n is the number of photons absorbed.

However, multi-photon physics is different for the X-ray regime as compared to high-intensity optical and IR lasers. In the X-ray regime, a single photon can already be sufficient to ionize, whereas in the optical regime several photons are needed even for a single ionization. The non-linear absorption of multiple X-ray photons can be characterized by a sequence of inner-shell photoioization and Auger decays [49].

For neon, several new processes have been discovered. One of the first experiments at LCLS produced fully stripped Ne^{10+} and also observed the rapid ejection of multiple inner-shell electrons producing *double core-holes* before Auger decay, resulting in an effect called intensity-induced X-ray transparency [22].

Other experiments revealed details on non-linear ionization in neon, where two contributing processes in the production of Ne^{9+} are involved: Two-photon one-electron direct ionization; and two-photon two-electron sequential ionization involving transient excited states [23, 50].

New effects also affect the maximum level of ionization that can be reached. Resonance enabled X-ray multiple ionization was measured in heavy atoms producing charge states much higher than expected by a simple sequential ionization model [24].

Heavy atoms that are irradiated by intense X-ray FEL pulses are challenging

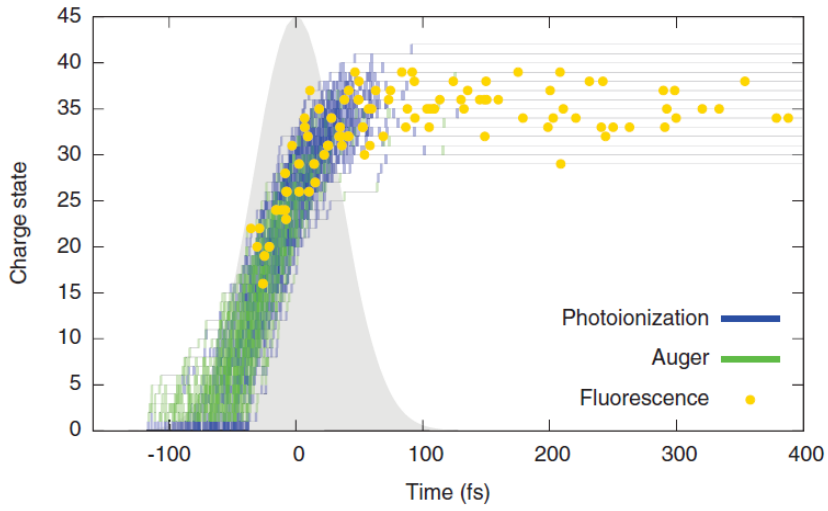

Figure 2.5: 100 exemplary ionization pathways for Xe interacting with an FEL pulse with 80 fs (FWHM) length (illustrated by the gray Gaussian) and 5×10^{12} photons/μm^2 fluence.[3]

to model because of the very large number of possible pathways involved in the ionization dynamics. Recent attempts of tracing the ionization dynamics in heavy atoms by Sang-Kil Son and Robin Santra give insight into the complex manifold of trajectories as a function of time [51]. Figure 2.5[3] illustrates this for the case of Xe atoms irradiated by an 80 fs FEL pulse with a fluence of 5×10^{12} photons/μm^2. The blue traces indicate photoionization while the green lines indicate Auger decay. These pathways show that several photons can be absorbed before the end of the Auger cascade. It also can be seen that Auger decay becomes less likely for higher charge states giving rise to fluorescence decay (indicated by the yellow dots).

[3]Source: S-K. Son et al. PR A 85, 023414 (2012), figure 2, reprinted figure with permission from reference [51], Copyright (2012) by the American Physical Society.

2.2 Photoionized Molecular Systems

The general ideas and methods for the study of photoionization of single atoms and polyatomic systems, i.e. molecules, clusters, and bulk material, are very similar, although important differences can apply when looking at specific systems [52].

To some extend, a molecule can be seen as a combination of atoms. In fact, one of the big steps towards modern quantum chemistry was the *linear combination of atomic orbitals* (LCAO) technique that can be used to estimate the molecular orbitals formed upon bonding of its atomic constituents [53].

When considering a molecule as a system of N bound electrons and M nuclei, the wavefunction is dependent on both, the movement of the electrons and the nuclei. As the nuclei have a much larger mass than the electrons, their motion is significantly slower. The fact that the electrons move much faster and are thus able to adapt to nuclear motion almost instantaneously leads to the *Born-Oppenheimer-Approximation*, where the coupling of the motion of nuclei and the electrons is neglected. With this approximation, the total wavefunction of a molecule can be written as a combination of the electronic wavefunction $\psi(\vec{r}, \vec{R})$ and the nuclear wavefunction $\chi(\vec{R})$:

$$\Psi(\vec{r}, \vec{R}) = \psi(\vec{r}, \vec{R})\, \chi(\vec{R}) \tag{2.15}$$

where $\vec{r}$ are the electron coordinates and $\vec{R}$ are the nuclear coordinates.

Like in atoms, transitions between molecular states can be triggered by the absorption of one or more photons. If these transitions happen on a time scale where the positions and the velocities of the nuclei do not change, this is called a vertical or *Franck-Condon* transition (as indicated by the red arrows in figure 2.6). However, strictly speaking, this is not the case for many inner-shell transitions that are triggered by X-ray absorption. In fact, electron transitions and nuclear motion can happen on the same timescales of a few femtoseconds, as will be discussed in section 2.2.2.

A schematic of several potential curves for a prototypical diatomic molecule is shown in figure 2.6: There are bound states such as A and B, which have at least one stable vibrational state of the nuclear wavefunction $\chi(\vec{R})$, as well as dissociative states like C. Photoionization can trigger the transition between two bound states or from a bound to a dissociative state. The excitation of the system into a dissociative state C leads to dissociation of the molecule and the excess binding energy, freed in

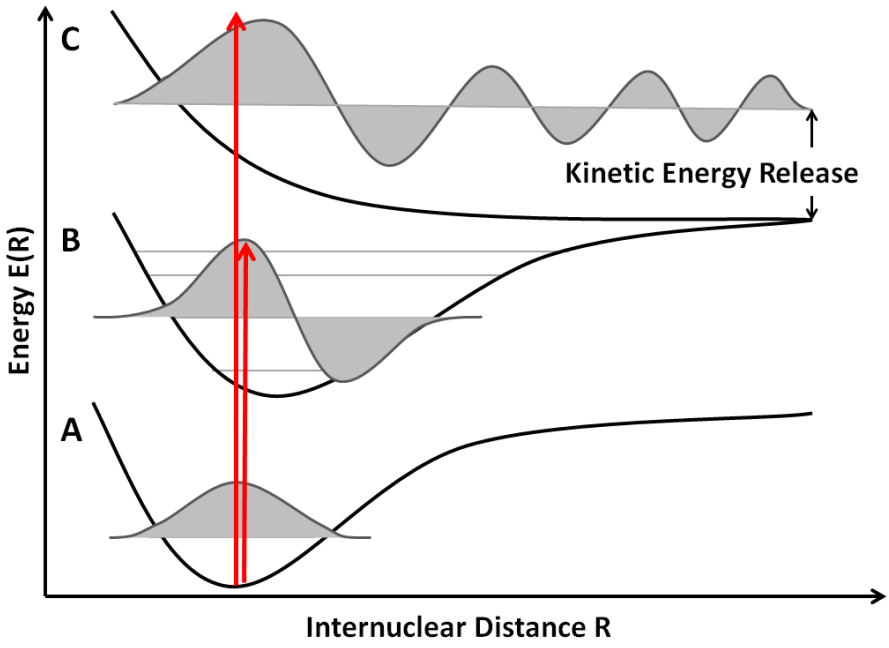

Figure 2.6: Schematic example of the photoionization of a molecule. The Franck-Condon transitions between two bound states (A $\rightarrow$ B) and from a bound to a dissociative state (A $\rightarrow$ C) are shown. Gray curves represent the nuclear wavefunction for a certain vibrational level which are indicated by the horizontal lines.

the transition, is transformed into kinetic energy of the molecular fragments. The total kinetic energy of the ionic fragments is also called the *kinetic energy release* (KER).

The transition probability between two molecular states can be calculated using the Born-Oppenheimer-Approximation as the product of the transition probability of the electronic and the nuclear wavefunctions. Thus, a one-photon transition can be written in the following way:

$$|c_f(t)|^2 = \left| \int \langle \psi_f(r,R)|H|\psi_i(r,R)\rangle_r \, \chi_f(R)\chi_i(R) \; dR \right|^2 \tag{2.16}$$

where H is the molecular Hamiltonian and indices i and f are initial and final states, respectively.

This expression can be simplified using the Franck-Condon principle, assuming that the transition happens at the same internuclear distance – such as the equilib-

rium distance R_{equ}. The transition probability then becomes:

$$|c_f(t)|^2 \sim \left|\langle\psi_f(r, R_{equ})|H|\psi_i(r, R_{equ})\rangle_r\right|^2 \left|\int \chi_f(R)\chi_i(R)\ dR\right|^2 \tag{2.17}$$

where the second part is called the *Franck-Condon factor* that determines the intensity of a vibronic transition.

2.2.1 Fragmentation of Core-Ionized Molecules

The photoionization of a molecule, especially of deep inner-shell electrons, proceeds very similar to the ionization of a single atom. Consequently, X-ray photoabsorption spectra of molecules show resonances close to the core-ionization edges of its atomic components [36]. In fact, the relatively small difference in electron binding energy between a free atom (elemental state) and the same atom in a chemical environment (chemical state), also known as the *chemical shift*, is used in X-ray photoelectron spectroscopy (XPS). As the binding energy is dependent on the chemical environment, one can not only identify the constituents of the molecule but also their composition because one can distinguish photoelectrons that are emitted from the same atomic species having different neighboring atoms [10].

Due to the relatively large difference in binding energy of the inner-shell electrons in *different* atom species and the resulting difference in respective absorption cross sections, the energy of the incident photon can be tuned to be predominantly absorbed by one atomic species in the molecule [54]. For certain heteronuclear molecules, the core-ionization or -excitation can thus be site-specific to a rather large extent – with ratios between the different atomic cross sections of 50 to 1 and higher.

Many of the subsequent decay processes in a molecule are very similar to the ones in an atom, described in section 2.1.3, but as the molecule consists of several atomic constituents, the picture gets more complex. In fact, the relaxation processes occurring after inner-shell photoionization in a highly excited molecular system are a manifold of competitive or sequential events including radiative decay, Auger decay, and dissociation into neutral, singly or multiply charged fragments. In the case of fluorescence decay, the de-excitation happens radiative, as discussed in section 2.1.3, and the fluorescence yield is dependent on the atomic number Z. For K-shell ionization of constituents like carbon and oxygen, the yield is $\sim 0.01\%$.

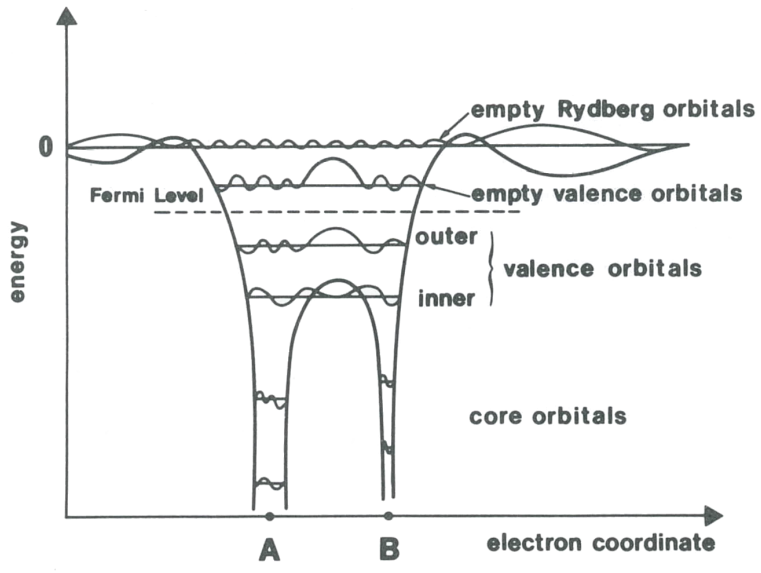

Figure 2.7: Schematic of the electronic potential of a molecule AB with occupied and unoccupied orbitals. The schematic also shows the localized character of the core orbitals, as compared to the delocalized or "shared" valence electron orbitals.[4]

For L-shell ionization of heavier constituents such as selenium, the yield is $\sim 2\%$; and for iodine, the yield is $\sim 10\%$ for transitions with a singly charged initial state. This shows that for the de-excitation of core-vacancies discussed in this work, Auger decay is the dominant process.

One of the questions arising in this context is, if and how the initially localized excitation spreads spatially within the molecule in the course of multiple decays and fragmentation processes. To understand the *inter-* or *intra-atomic* character of the de-excitation, meaning whether a decay involves electrons that are located on the same or a different atomic site than the core-vacancy, the different characters of the orbitals have to be considered. The electronic potential of a diatomic molecule, AB, with occupied and unoccupied orbitals, is schematically shown in figure 2.7[4]. While core-levels are basically localized on each atom, valence electrons can be completely delocalized, especially outer valence or "bonding" orbitals, or may be able to tunnel such as in the case of inner valence electrons. This nature of bonding valance orbitals and the overlap of orbitals of atoms A and B is important for the

[4]Source: I. Nenner and P. Morin, P., VUV and Soft X-Ray Photoionization, 1. edition, chapter 9, page 293, figure 2, Springer (1996); with kind permission from Springer Science+Business Media B.V., reference [52].

intra- and interatomic character of the transition.

To answer the question of charge localization, during and after the decay cascade, one has to distinguish between "shallow" and "deep" initial core-holes, or, in other words, consider the number of localized shells that are above the ionized inner-shell.

Most small organic molecules that occur in nature are molecules that contain atomic constituents with $Z < 10$, e.g. carbon, nitrogen or oxygen. If these molecules are core-ionized at the 1s-level, only the valence shell lies above the created hole, the case of a "shallow" initial core-hole. This allows for KLL Auger decay involving the localized hole and the delocalized valence electrons. For these molecules, the question whether the Auger decay happens intra- or inter-atomically, as well as the distribution of the two final holes was found to be highly dependent on the type of chemical bond in the neutral molecule – either *covalent* or *ionic* [52].

In the case of covalent (polar) bonding species, such as CO, the holes are most likely localized on the initially ionized site. This was shown by distinct differences in the Auger electron spectra of CO, depending on whether the initial ionization targeted the carbon or the oxygen site (see reference [52] for details). For ionic compounds, such as SiF_4, however, the final holes are more likely found on the ligand rather than on the site of the initial core-vacancy [55, 56].

A field that is closely related to the question of inter- and intra-atomic electron transitions and that has become increasingly popular in recent years is the investigation of excited ionized states of weakly-bound systems, such as van-der-Waals clusters. These studies have shown that de-excitation of an ion can involve its environment (at relatively long distances), enabling autoionization pathways that are forbidden in an isolated ion [57, 58].

One of theses processes is the so-called *interatomic Coulombic decay* (ICD), where an inner-shell vacancy created, e.g. by photoionization, is filled by an electron from the same atom and an electron is emitted from a species in the immediate neighborhood of the initial vacancy [59, 60, 61, 62]. A second process is the so-called *electron transfer mediated decay* (ETMD). Here, the vacancy is filled by an electron from a neighboring site and an electron is released either from the electron donator or from a third neighboring species [63, 64]. Both of these interatomic processes are mediated only by electron correlations and do not require nuclear dynamics.

Looking at Auger decay in molecules with higher-Z constituents of the third (or 4th, 5th etc.) row, the situation immediately becomes a lot more complex. This also

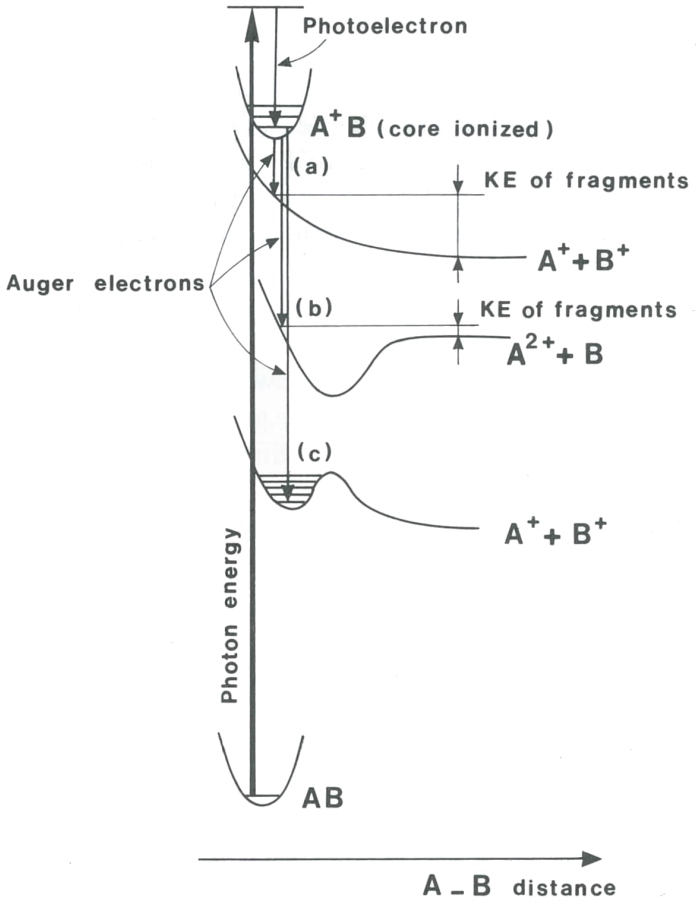

Figure 2.8: Schematic of the dissociation of an inner-shell ionized diatomic molecule AB that undergoes Auger decay and subsequent fragmentation: (a) for a pure Coulomb explosion; (b) dissociation with charge localized on one particle; (c) non-dissociative state.[5]

becomes clear when looking back at the atomic case of argon shown in section 2.1.3, figure 2.4. Here, an initial K-shell vacancy, a "deep" initial core-hole, can lead to 5 final states involving 13 intermediate transitions, whereas an initial L_1-shell vacancy only leads directly to two final states. This, of course, also has implications on the localization of the decay processes in a molecule. Now, for K-shell ionization the first Auger decay involves electrons from (localized) core-levels and only afterwards induces several holes in the valence shell via multi-step Auger cascades. A complete description of the Auger process in a molecule requires spectroscopic data on the final cationic state, which is, for most molecules, very complicated because of the large density of states and differences in geometry compared to the ground state [52].

A molecule that is charged up in the course of a decay cascade can dissociate,

distributing the charge among its fragments. Figure 2.8[5] shows an example of an initially core ionized diatomic molecule AB, which has lost two or more electrons by Auger decay. The resulting state can either be of a pure Coulomb potential (case (a)) with two repulsing ions involved ($A^+ + B^+$), a dissociation with both charges on one of the fragments ($A^{2+} + B$) (case (b)), or, in some cases, a non-dissociative dicationic state (case (c)).

Sometimes the $A^+ + B^+$ potential curves are not purely Coulombic. The kinetic energy (KE) of the fragments (indicated in figure 2.8) depends on the shape of the potential curve and, in practice, there are many states with potential surfaces where electronic, vibrational and rotational couplings are of importance. This is especially true when considering fragmentation into neutral and singly charged ions.

In some cases, the highly excited molecule is not fragmenting immediately but undergoes geometrical changes as a reaction to the change in electron configuration. Vibrations in the molecule happen on a time scale of sub-picoseconds, and thus can interfere with Auger processes that happen on a time scale of a few to several tens of femtoseconds. Using the high resolution power of third generation synchrotron radiation sources, it is possible to resolve vibrational structures in photoabsorption and photoelectron spectra. A review of this topic is given in reference [65]. Rotational effects, however, are mostly out of reach for photoabsorption and photoelectron spectra. This is mainly due to the slower motion of rotations on the picosecond time scale that are longer than any autoionization process and also require a very high (microelectronvolt) energy resolution [52].

When the photon energy is close to but below an absorption edge, the inner-shell electron is not freed into the continuum but rather excited into a valence or Rydberg orbital. This molecule is then called *core-excited*. The main differences to a core-ionized molecule are in the effects that happen before the first Auger decay or autoionization takes place. In the core-excited case, the molecule can be either in a bound or a repulsive state, which can be predicted by using the equivalent core or "Z+1" model. This allows the molecule to change geometry before the first electron leaves the system. In the $Z + 1$ approximation, a core-excited atom can be thought of as replaced by the subsequent atom in the periodic table as far as the prediction of structural and electronic behavior of the molecule is concerned [66].

[5]Source: I. Nenner and P. Morin, VUV and Soft X-Ray Photoionization, 1. edition, chapter 9, page 294, figure 3, Springer (1996); with kind permission from Springer Science+Business Media B.V., reference [52].

If the photon energy is far beyond the absorption edge, the electrons are ejected into the continuum and core-ionization is dominant. This is the case in this work, where the X-ray photon energies are more than 50 eV above the corresponding edges.

In the simplest case, the dynamics following core-ionization can be treated as a stepwise process, where the Auger decay happens first, producing a multiply charged parent ion, which then fragments due to dissociative potentials. In this picture, it is left unclear whether the molecule is still in a close-to-ground-state geometry or if the bond distances and angles have changed to a point where one can no longer speak of a molecule in the classical sense. In the case of "shallow" core-holes or valence ionization, this 2-step model of ionization followed by dissociation is certainly valid for many systems, but in the case of "deep" core-level ionization, nuclear motion and Auger cascades happen on the same timescales such that Auger decay(s) and fragmentation can no longer be considered as strictly sequential events.

2.2.2 Molecular Dynamics in Intense X-Ray Pulses

The high photon flux provided by Free-Electron Laser light sources enables the absorption of multiple photons in a single, few to few-hundred femtosecond light pulse, thus adding another time-dependent process to the multiple ionization besides single Auger decay or Auger cascades. In a molecular environment, this makes a purely sequential picture of "ionization before dissociation" very unrealistic. In the interaction of molecules with short X-ray FEL pulses, sequential photoionization and electron relaxation, both present also in an atomic system, are complemented by a third reaction, the nuclear motion. All three processes, that happen on the same time scale, effectively influencing each other have been discussed previously in general, but their time scales have only been mentioned briefly. In the following, the time sequence of each individual reaction and interactions between them will be discussed.

Auger Decay lifetimes are measured by high-precision Auger electron energy spectroscopy where the center energy determines the Auger transition and the width is linked to the lifetime via the Heisenberg uncertainty principle (equation 2.3). A table of elemental values of Auger linewidths is given in reference [67] and a set of lifetimes relevant for this work is given in table 2.1.

Auger lifetimes in singly core-ionized systems typically range from ~ 10 attosec-

Atom Subshell	K	L1	L2	L3	M1	M2	M3	M4	M5
C	8.24								
O	4.71								
Cl	1.16	0.44	5.99	5.99					
Kr	0.24	0.18	0.53	0.55	0.19	0.41	0.60	9.41	9.15
Se	0.29	0.17	0.63	0.65	0.24	0.30	0.30	10.14	9.98
Xe	0.06	0.33	0.22	0.23	0.06	0.19	0.14	1.10	1.10
I	0.06	0.31	0.22	0.24	0.06	0.20	0.15	1.18	1.18

Table 2.1: Table of Auger lifetimes (in fs) for a set of elements (calculated from reference [67]).

onds to a few tens of femtoseconds. In the cases discussed here, these time scales are only valid for the first vacancy after core-ionization and can serve as an estimate for the time scales of Auger decays that happen in multiply ionized and highly excited systems. In addition, the atomic values merely provide an order of magnitude for the corresponding time scales in molecules, where the true core-hole lifetime can be different due to additional electrons from the other constituents in the system and delocalization of orbitals in the molecule. Auger lifetimes therefore depend on the chemical environment [68, 52].

Note also that the lifetimes represent half-life times of exponential decay rates. Thus, combinations of Auger decays that follow each other rapidly, such as Auger cascades, can take place in less time than the mere sum of the individual decay steps.

Multiple Photoionization in the X-ray regime, at the intensity levels achievable today (up to $\sim 10^{18}\,\mathrm{W/cm^2}$), is dominated by a sequence of one-photon ionization and relaxation events [49, 22, 25, 23]. Because of the large number of photons in a single ultra-short FEL pulse, further photoionization can happen before the relaxation via Auger decay is completed [49, 69]. This is clearly different compared to third generation X-ray synchrotron sources, where one-photon absorption is dominant.

For the case of two-photon absorption, one can distinguish between the processes

producing double-core-holes – where the sequence of events is photoabsorption, photoabsorption, Auger decay – and those where the formation of a core-hole by photoabsorption is followed directly by an Auger decay. The probability of double-core-hole formation is governed by the statistical nature of the FEL pulse and the Auger lifetime of the system [69]. Production of double-core-holes by X-ray FELs have been experimentally demonstrated for simple prototypical systems such as Ne and N_2 by Young et al. [22] and Hoener et al. [25], respectively.

Measurements on sequential multiple photoionization of N_2 molecules [25] investigated ionization dynamics and ion yields of this prototypical system. An effect of frustrated absorption comparable to the case of Ne was found and the importance of valence electron dynamics in the molecule was shown. Double-core-holes are (in [25]) produced by sequential photoionization of 1s electrons in nitrogen. This process is only possible if the second core-ionization happens before the first vacancy is filled by an Auger decay, which requires the high-fluence pulses of an X-ray FEL.

In a later paper, the N_2 molecule was further investigated by means of Auger electron spectroscopy of the double core vacancy. In that setup, it was possible to distinguish the cases of a two-site double core-hole, where both N atoms have one core vacancy, or a single-site double core-hole with both vacancies located at one of the nitrogen atoms [26, 70]. Two-site double-core-holes (TSDCH) were further investigated in N_2, N_2O and CO_2. Differences in the $O^{-1}C^{-1}$ TSDCH states of CO_2 and CO support the theoretical prediction of high sensitivity of TSDCH states to the molecular environment [71, 27].

Nuclear Motion defines the third time scale that is relevant for molecular systems. Once the excited molecular system is in a dissociating state or the bonding strength is weakened, the nuclei move apart from each other. For higher charged systems, this dissociation can be assumed to be Coulombic. In this case, the motion of ions can be estimated considering Coulomb's law:

$$\vec{F}_{12}(\vec{r}_1) = \frac{q_1 \cdot q_2}{4\pi\varepsilon_0 \cdot |\vec{r}_1 - \vec{r}_2|^2} \frac{(\vec{r}_1 - \vec{r}_2)}{|\vec{r}_1 - \vec{r}_2|} \tag{2.18}$$

where q_i is the charge, $\vec{r}_i$ is the position vector of the particle i, ε_0 is the permittivity and $\vec{F}_{12}(\vec{r}_1)$ is the force vector that acts on particle 1. The potential energy E_{pot} of

a simple two-ion system can be expressed as a function of internuclear distance r:

$$E_{pot} = \int \vec{F} \cdot d\vec{s} = \frac{1}{4\pi\varepsilon_0} \frac{q_1 \cdot q_2}{r} \tag{2.19}$$

For an N_2 molecule, which fragments into N^+ and N^{2+}, this would yield a total kinetic energy of 26.2 eV. The time it takes to reduce this potential energy by a factor of two, i.e. to double the internuclear distance from 1.1 Å to 2.2 Å can be calculated to be 9.5 fs by solving the equation of motion. This will be discussed for more atoms and a more complex geometry in section 2.3.2. The time scale of less than 10 fs in the above example shows that nuclear motion can happen on the same time scale as Auger decay and sequential photoabsorption. This introduces an additional level of complexity because it means that the effective separation of nuclear and electronic terms (shown in equation 2.15) breaks down as the motion of the nuclei and the electrons can no longer be approximated as decoupled.

The interplay of Auger decay cascades and nuclear motion is especially relevant for H ions because of their fast motion. This is particularly true for very rapid phenomena like the transfer of H+ from one atom to another or concerted breakup of several hydrogen bonds and formation of H_2^+ [72].

So far, most experiments performed on the interaction of X-ray FEL pulses with molecular systems, were focused on small diatomic and triatomic molecules of low Z constituents, namely carbon, nitrogen and oxygen. One of the next logical steps in molecular FEL science, is to investigate larger polyatomic molecules with heavier atomic constituents, which will be discussed in the following chapters. This work is also motivated by the fact that experiments on heavier atoms, e.g. Xe [24] and Kr, at LCLS have revealed extremely high levels of ionization (as mentioned earlier).

Last but not least, a strong motivation comes from the envisioned application of FEL radiation for (coherent) imaging of nano-crystals and single molecules. Proteins often contain heavy elements such as Fe, S, Mg and others which effectively increase X-ray absorption locally, leading to enhanced local damage that cannot be accounted for via traditional methods [20]. The detailed understanding of localized X-ray absorption and the up-charging of the environment, its dynamics as well as the local extension of damage seems crucial for the success of imaging experiments on single particles utilizing ultra-intense FEL pulses.

A suitable class of benchmark molecules is represented by systems consisting of

two or more atoms, where one constituent has a significantly higher atomic number than the other constituents. For a carefully chosen photon energy this can imply that the initial photoabsorption is almost exclusively localized on the heavy-atom site.

Single-photon experiments of this class were first performed by T. A. Carlson and R. M. White on methyl iodide [73] and ethyl iodide [74]. Here it was shown, for the case of single photon absorption at the iodine L-shell, that the molecule is highly ionized and undergoes complete fragmentation producing high-energy ionic fragments. In this context, calculations of a simple Coulomb explosion were employed to model the measured kinetic energies of ionic fragments.

2.3 Coulomb Explosion Imaging

One proposed key application for FELs is the ability to explore dynamic processes on the atomic scale measuring the structure of nanoscale objects on a single shot basis – eventually as a function of time and, thus, realizing the dream of a "molecular movie". For large biomolecules, this is pursued mainly by means of coherent photon diffraction. For single small molecules, the number of scattered photons is too low due to small cross sections and other, more promising approaches are developed. One of these techniques is the so-called *Coulomb Explosion Imaging* (CEI). This method was first demonstrated by utilizing a high kinetic energy ($\sim 10^6$ eV) molecular ion that is shot through a thin foil [75]. In this process, the molecule gets stripped off most of its electrons on a timescale of ~ 100 as and undergoes fast dissociation driven by the Coulomb repulsion forces, resulting in a so-called *Coulomb Explosion* (CE). From this explosion, the initial structure of the molecule can be reconstructed by measuring the vector momenta of the individual fragments. If the ionization happens on time scales much smaller than the characteristic time of nuclear motion, the molecular geometry is directly mapped to the fragment momenta. This is based on the assumption that the potential describing the interaction of the stripped ions is known.

Because of the continuously increasing interest in the development of time-resolved approaches in the pursuit of the "molecular movie", the possibilities offered by CEI exploiting optical laser systems are being actively explored. There, molecular dynamics are initiated with one laser pulse, called pump pulse. The snapshots – like in a movie – of evolving molecular structure are then taken by CEI of the molecule, which is induced by a second (probe) laser pulse, arriving after a certain time delay. This approach can be employed only if the molecular geometry does not change significantly during the time which is needed by the probe pulse, for the removal of a sufficient number of electrons to induce CE. This implies, that the probe pulse has to be short as compared to the characteristic time scale of the motion of the atomic constituents in the molecule.

When Coulomb Explosion is driven by an optical laser [76, 77], e.g. a femtosecond pulsed Ti:Sa laser (~ 800 nm wavelength), the interpretation of the fragmentation process often becomes rather complex. The removal of the first electron often triggers molecular dissociation, which proceeds on the potential surfaces distorted by

the laser field. Depending on the laser parameters, further electrons can be removed on the time scale comparable to that of the dissociation. This results in the experimental observation that even for rather short, 50 fs laser pulses, precise CEI of the molecular structure is only possible for heavy molecules such as iodine [78]. Nevertheless, with few-cycle optical laser pulses of less than 10 fs duration, CEI of the lightest molecules, such as hydrogen [79] or deuterium [80], comes into reach. CEI of D_2O and SO_2 molecules, comparing 45 fs and 8 fs laser pulses, is discussed in reference [81].

Besides the time scales involved, the basic process of ionization with an intense optical laser, like a Ti:Sa at 800 nm wavelength, sets a fundamental limit to how well the molecular structure can be determined by CEI. This is due to the fact that the probability to ionize a molecule at this wavelength is very sensitive to the ionization potential which is strongly correlated to the nuclear coordinates, i.e. the distance between the constituents [81].

In order to overcome this limitation, it was proposed to employ short-wavelength (e.g., EUV) radiation as a probe in CEI since the ionization probability for high-energy photons is much less sensitive to the details of the molecular potential. With the availability of intense, short-pulsed EUV and soft X-ray pulses, delivered by FELs, this approach was successfully tested for a few prototype molecular systems such as D_2 [82], N_2 and O_2 [83]. A review of this topic is given in references [84, 85].

2.3.1 Principles of CEI

The key assumption underlying the method of Coulomb Explosion Imaging is that the process of ionization happens on a time scale that is smaller than the time it takes for significant movement of the ions away from their equilibrium positions. By removing a sufficient number of electrons, usually the binding molecular potential is transformed into a Coulombic dissociative potential that causes the ions to fly apart, i.e. the molecule "explodes".

In the case of a diatomic molecule, the relation between the kinetic energy of the fragments after explosion and the inter-nuclear distance is straightforward assuming immediate, or so-called vertical, ionization as shown in figure 2.9.

The two ions with respective charges Q_1 and Q_2 and masses m_1 and m_2 start

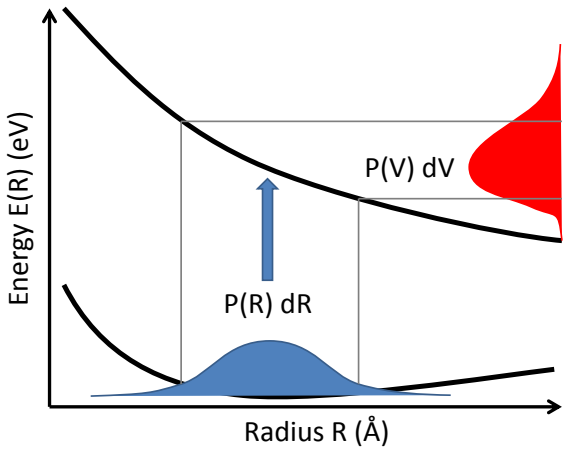

Figure 2.9: Schematics of the vertical transition from a bound potential to a dissociative Coulomb potential. The blue wavepacket is the sum of vibrational states of a diatomic molecule and the red curve is (in the center of mass system) the kinetic energy distribution after dissociation.

with a distance $r(t_0) = R$. For this system the total energy is given by:

$$E_{total} = \frac{Q_1 Q_2}{R} = \frac{Q_1 Q_2}{r(t)} + \frac{1}{2}\mu v(t)^2 = \text{const.} \tag{2.20}$$

where $\mu = {}^{(m_1 m_2)}/_{(m_1+m_2)}$ is the reduced mass and $v(t)$ is the relative velocity of the particles. The final velocity V is given by the limit of $t \to \infty$ and can be calculated from:

$$V(R) = \sqrt{\frac{2Q_1 Q_2}{\mu R}} = 0.023\,\text{au} \times \sqrt{\frac{Q_1 Q_2}{\mu[\text{u}] R[\text{Å}]}} \tag{2.21}$$

With $|P(V)dV| = |P(R)dR|$, one gets the transformation formula between real space, i.e. internuclear distances, and velocity space, i.e. the measured momentum space:

$$P(V) = \sqrt{\frac{Q_1 Q_2}{2\mu}} R^{-3/2} P(R) \tag{2.22}$$

This allows for the calculation of the real space density from a measured velocity distribution. However, this only holds for the assumption made in the beginning that the ionization happens immediately and that there are no other effects disturbing the pure Coulombic potential.

This simple picture of course only works for diatomic molecules that undergo instant ionization. In a real dissociation, even for simple diatomic molecules, there

will be cases where the above assumption of *vertical ionization* to a dissociative state is not valid. This is particularly the case for inner-shell ionization.

Coulomb Explosion upon Inner-Shell Ionization

Ultrashort, few femtosecond X-ray pulses, as delivered by modern XFELs like LCLS, can trigger substantial ionization in the molecule, which is, in contrary to optical lasers, to a large extend not sensitive to the molecular geometry because of the small wavelength. After inner-shell ionization, the molecule is, at first, transformed into an electronically excited state that is, in most cases, still bound but has a different potential and, thus, has different vibrational and rotational states. This may lead to a change in bond length and angles in the molecule. Another possible scenario is the fragmentation of the molecule before de-excitation is over, as discussed before. This increase in the charge of the ionic fragments during the dissociation results in final kinetic energies of ions that do not only reflect the initial, equilibrium nuclear distances. In this case, the interpretation of the results becomes more complex and insight into the ionization dynamics is needed to reconstruct the precise molecular geometries. However, the assumption becomes more valid the shorter the FEL pulses are and the faster the Auger decays happen.

2.3.2 Simulation of Coulomb Explosion

To be able to interpret the results discussed in chapter 2.1.3 in a more detailed way, a simple numerical model of Coulomb explosion was designed. It is intended to run on a personal computer and to make calculations for systems containing up to 10^4 ions in a time-frame of up to few hours. The presented simulation is based on a model that has been used to treat the Coulomb explosion dynamics of small noble gas clusters with less than 2000 atoms [86].

The simulation only considers the ions and does not take into account any electronic or photon-matter interaction dynamics. It is clear that this assumption does not represent the full physics of the processes that happen during (and after) the interaction of the FEL and the molecule. Nonetheless, the model is able to provide a rough idea of the energies which can be expected from a Coulomb Explosion experiment for a given molecular geometry.

Classical Particle Dynamics

The initial positions of the ions at time $t = 0$ are those of the atoms in the molecular equilibrium state. These initial positions are taken from molecular energy minimization algorithms. The positions, bond lengths, and angles for the molecules considered in this work are given in the appendix B.

The motion of the individual ions is determined by Newton's second law $\vec{F} = m\vec{a}$. To propagate the positions and velocities of all the particles in three-dimensional space, a set of differential equations has to be solved. In this case, these are three coupled equations of the form:

$$\frac{d^2y}{dx^2} + f(x)\frac{dy}{dx} = gx \tag{2.23}$$

These second order differential equations can be reduced to two first order differential equations

$$\frac{dy}{dx} = \zeta(x) \tag{2.24}$$

$$\frac{d\zeta}{dx} = g(x) - f(x)\zeta(x) \tag{2.25}$$

by introducing a new variable $\zeta(x) = \frac{dy}{dx}$. These two new differential equations of first order standardize the problem and, thus, allow for the use of standard algorithms described below.

For the problem considered here, the equations of motion of a fragment ion of the molecule for one direction (here the x-direction) are given by:

$$\frac{dx}{dt} = v_x \tag{2.26}$$

$$\frac{dv_x}{dt} = \frac{F_x}{m_{ion}} \tag{2.27}$$

where v_x is the particle velocity in x-direction, m_{ion} is the mass of the ion, and F_x is the force acting on the particle in x-direction. The force on the particle is determined by the Coulomb forces between this particle and all the other charged particles in the system. As the force is only dependent on the distance between the particles at a given time t, the time becomes the independent variable in which the system is evolved.

This is done by taking the initial values of the coordinates and by solving the functions for a given time t, and by then multiplying the result with a small step size value δt. This is a way to track the particle's position and velocity as time evolves by step sizes of δt. Smaller step sizes result in an increased accuracy but also increase the required computation time. The simplest way to solve these kind of differential equations is *Euler's method*, which follows exactly what is described above, but is not sufficient for most practical applications, as the errors at each step add up and finally become too large.

A common and much more sophisticated approach is the so-called *Runge-Kutta method*. Here, a solution is processed over a given time interval combining the information from several steps with Euler's method that is then used to match a Taylor series expansion up to a certain order. When using an expansion of only the first order, this again reduces to the simple Euler method. Although this technique has a significantly lower error and the accuracy can be very good, one has to keep in mind that all these numerical methods introduce small errors. For the Coulomb Explosion simulation presented here, a fifth-order Runge-Kutta algorithm, using Dormand Prince [87] parameters, is used. The framework provided by the GNU Scientific Library [88], was used for the calculations. This library includes the use of an adaptive step size that was changed automatically to keep the overall error of the iteration steps as small as possible. The particles in this simulation are treated purely classical. They start with a fixed charge that is set for every particle individually and that does not change during the simulation.

When designing these kinds of simulations, one important factor is computation time, i.e. the time it takes to run the calculations. N particles that move in three-dimensional space have to be considered, and to determine the forces acting on a single particle, the interactions with all other particles have to be calculated. This results in $3N^2$ calculations to compute the movement of all particles for one time step δt. For a molecule with 6 atoms, this equals 108 calculations per time-step .

Note that the simulation is designed to provide information on the kinetic energy of the particles at a point far away (in space and time) from the FEL-molecule-interaction region for comparison with experimental data. Thus, it is designed to process the coordinates of individual particles until they hit the detector after some microseconds. The time steps thereby are automatically adapted to ensure for a sufficiently low numerical error.

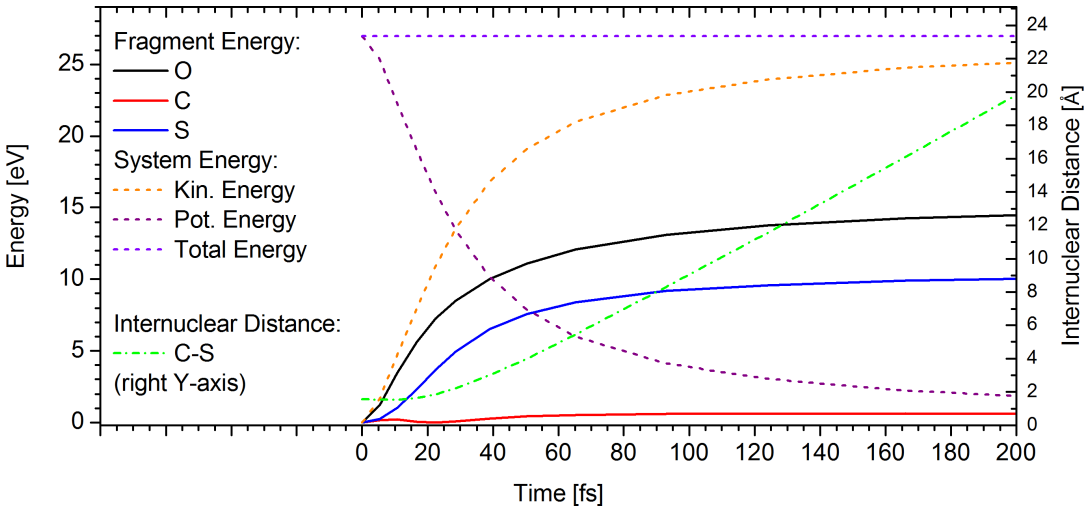

Figure 2.10: Example of the simulation output for an OCS molecule for the fragmentation channel $[OCS]^{3+} \longrightarrow O^+C^+S^+$.

This can be seen for the example of the linear OCS molecule in figure 2.10. At $t = 0$, all particles are at rest and the total energy is simply the summed potential energy. As the system evolves, the sum of potential and kinetic energy stays constant. The kinetic energy increases, and at a certain time, the potential and the kinetic energy are equal. This time can also be interpreted as the expansion time of the system. In the following section the model is applied to the molecules that are discussed in this work.

Simulation Parameters

As already mentioned above, the main parameters in the simulation are the initial charges of the particles and the equilibrium geometry of the molecule. It is also possible to change specific bond lengths to simulate vibrations or rotations away from the equilibrium values.

Within the scope of this work, the following molecules, shown in figure 2.11, were investigated with this simulation: Methylselenol, ethylselenol, iodine chloride, and methyl iodide.

The initial parameters for each of theses molecules such as atomic positions, bond lengths, and angles are given by their equilibrium geometry; the charge states of individual ions is chosen according to the final charge state of the molecule that is simulated. The output of the simulation are either the time-dependent positions

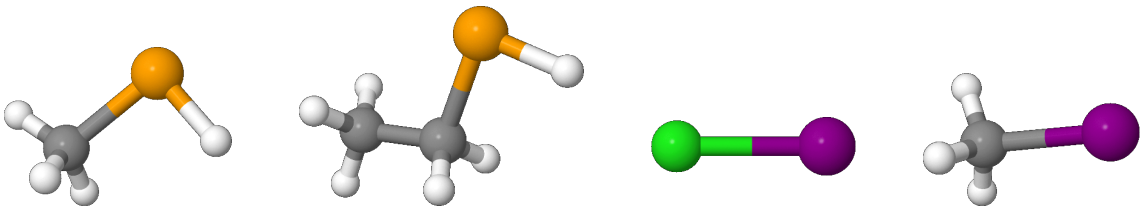

(a) Methylselenol (b) Ethylselenol (c) Iodine chloride (d) Methyl iodide

Figure 2.11: Equilibrium molecular geometry of the small molecules studied in this work.

of the particles or the final kinetic energy of the particles and the directions of their momentum vectors.

An example for the results of the simulation is given in figure 2.10. Several interesting observations can be made: First, as OCS is a linear molecule (O=C=S), the kinetic energy of the center atom remains very low as the forces from the charges on either side cancel each other out, which is also known as "obstructed fragmentation" [89]. The second interesting feature is that the distance between the C and S ion starts to increase only 20 fs after the pulse. This gives some upper timescale for the ionization process to fulfill the vertical ionization assumption.

Chapter 3

Experimental Setup: Coincident Ion Momentum Spectroscopy at the LCLS

This chapter discusses the experimental arrangement used in this work to study the interaction of intense, short-pulse X-rays with small molecules, by means of coincident ion momentum spectroscopy.

Basic operation principles of X-ray Free-Electron Lasers (X-FELs) and their technical realization, are discussed in section 3.1, for the case of the Linac Coherent Light Source (LCLS) at SLAC National Laboratory. This is followed by the description of the LCLS parameters and beam diagnostics relevant for this work (section 3.1.3).

The design of the CFEL ASG Multi-Purpose (CAMP) endstation is introduced in section 3.2.1. The specific setup, optimized for imaging the fragmentation of small, gas-phase molecules by ways of coincident ion momentum spectroscopy, is described in section 3.2.2. Specific parameters of the cold molecular jet and the 3D-momentum imaging ion spectrometer are discussed in section 3.2.3 and 3.2.4, respectively. In section 3.3, data-acquisition and data-processing steps are presented.

3.1 The LCLS – The World's First X-Ray Free-Electron Laser

The world's first X-ray Free-Electron Laser, the *Linac Coherent Light Source* (LCLS), is in operation since fall 2009. At a total of six beamlines – all designed for specific applications – the LCLS provides X-ray pulses in the wavelength range from 1.2 Å to 22 Å, containing up to 10^{13} photons per pulse, with pulse durations tunable from $\sim$ 500 fs down to just a few fs [90]. Other operating and proposed Free-Electron Lasers include FLASH [91] and the SCSS test accelerator [92], in the EUV range, as well as SACLA [93] and the European XFEL [94] in the X-ray regime.

In the following, an overview will be given on how X-ray FEL pulses are generated, considering particularly the example of the LCLS. This is followed by a short discussion of some relevant FEL parameters and the diagnostic tools used to monitor them at the LCLS.

3.1.1 Electron Acceleration

The first step in the generation of intense X-FEL pulses is to produce short bunches of electrons. These electrons need to have a sufficiently high phase-space density to achieve the so-called *self amplified spontaneous emission* (SASE), as described later.

An important parameter in this matter is the *emittance*, which is the average spread of particle coordinates and momenta in the phase-space. In fact, although the idea of an FEL was proposed as early as 1971 [95], and the first IR FEL was realized in 1975 [96], it only became possible in 2001 to achieve the required level of the electron beam emittance, resulting in the operation of the first optical FEL [97].

To create and maintain short electron pulses in a linear accelerator – as the one used at the LCLS – several methods are applied. First, the electron bunch is produced in a photocathode radio frequency (RF) electron gun. At the LCLS, a copper cathode is irradiated by 3 ps short ultraviolet (UV) laser pulses with a repetition rate of 30 to 120 Hz, thus defining the repetition rate of the electron bunches and consequently the X-ray pulses. At the point of injection into the main linear particle accelerator (linac) the electrons have a kinetic energy of 135 MeV (see figure 3.1[6]). They are then further accelerated up to 250 MeV in an S-band

[6]Source: P. Emma et al. Nature Photonics 4, 641-647 (2010), figure 1, Copyright by the Nature Publishing Group, reference [90]

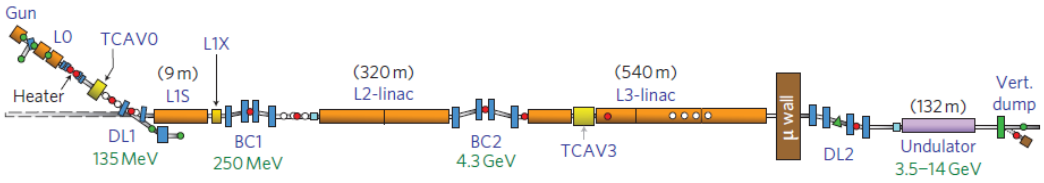

Figure 3.1: Overview of the LCLS accelerator sections.[6]

(2.856 GHz) linear accelerator using standing waves produced by klystrons in the cavities designed for resonant acceleration. After this acceleration the bunches enter a so-called *bunch compressor* chicane (BC), where the bunch length is shortened, thus increasing the peak current. Due to space-charge effects the compression of the bunch is limited by the total charge in the pulse. For the so-called low-charge mode at the LCLS, using only a 20 pC bunch charge instead of the typical 250 pC, the electron bunches can be compressed down to less than 10 fs length [98, 99].

After exiting the first bunch compressor (BC1), the electrons are further accelerated in two more linac sections (L2 and L3), with a second bunch compressor (BC2) in between, and exit the accelerator section with a final energy of 3.5 GeV - 14 GeV. The bunches are then passing through a 350 m long beam transport line into the 132 m long undulator section.

3.1.2 Undulators and the SASE Process

An *undulator* is a periodical array of dipole magnets, creating an alternating magnetic field along the beam propagation direction, as shown in figure 3.2[7]. Once the electron bunch enters the undulator, the Lorentz force $\vec{F} = q\vec{v} \times \vec{B}$ acts on the particles with charge $q = e$. The force is perpendicular to the velocity vector $\vec{v}$ and the undulator's magnetic field $\vec{B}$. Because of this induced transverse acceleration, the electrons spontaneously emit so-called *synchrotron radiation*. For electrons with high kinetic energy, i.e. $\beta = v/c \approx 1$, the radiation is emitted in a narrow cone of opening angle $1/\gamma = \sqrt{1-\beta^2}$ in the propagation direction [101].

The period of the magnet array, also called the *undulator period* λ_U, and the magnetic field B_0 are typical design parameters defining the deflection of the electrons in the undulator, by means of the deflection parameter $K = \frac{e}{2\pi m_e c}\lambda_U B_0$. The

[7]Source: B. W. J. McNeil and N. R. Thompson, Nature Photonics 4, 814-821 (2010), figure 2, Copyright by the Nature Publishing Group,reference [100].

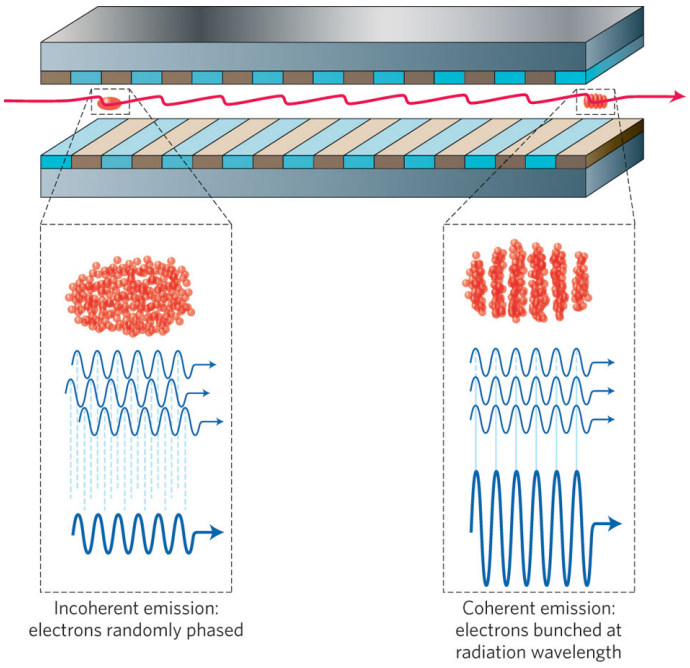

Figure 3.2: Microbunching in an FEL undulator: At the beginning of the undulator, the electrons are mostly randomly phased and, thus, emit radiation incoherently. Due to collective interaction of the electrons with their emitted radiation, small coherent fluctuations in the radiation field arise and lead to a bunching of the electrons. Towards the end of the undulators, the electrons are strongly bunched at the radiation wavelength and emit coherently.[7]

deflection angle can be approximated by $\pm K/\gamma$. For typical undulators $K \approx 1$, such that the deflection of the electrons is comparable to the radiation emittance angle $\pm 1/\gamma$. This allows for a maximized spatial overlap of the radiation, emitted at different points in the undulator, and the electron trajectories.

A transfer of energy between the electrons and the radiation field is the basic working principle of an FEL – in this sense, the relativistic beam of free electrons is the amplification medium for *light amplification by stimulated emission of radiation* compared to classical lasers [102]. In order to change the energy of the electrons, a component of the electron's velocity vector and the electric field of the radiation have to be parallel. This is the case inside the undulator, where the electron performs a sinusoidal motion due to the external magnetic field, as shown in figure 3.2. As the electron bunch has a spacial extension that is larger than the wavelength of the radiation, their interaction leads to modulations in the electron density on the length-scale of the emitted wavelength, which is called *microbunching*. The electrons become concentrated at the positions where the energy transfer to the radiation field

has a maximum. This is illustrated in figure 3.2. This bunching of the charge on the radiation length scale enables the electrons to radiate in phase, thus increasing the radiation power drastically.

The power P of the radiation emitted by $N \gg 1$ electrons in an undulator is given by:

$$P \propto \left| \sum_{\mathrm{j}=1}^{\mathrm{N}} E_{\mathrm{j}} e^{i\varphi_{\mathrm{j}}} \right|^2 = \sum_{\mathrm{j}=1}^{\mathrm{N}} E_{\mathrm{j}}^2 + \left| \sum_{\mathrm{j}=1}^{\mathrm{N}} \sum_{\mathrm{k}=1}^{\mathrm{N}} E_{\mathrm{j}} E_{\mathrm{k}} e^{i(\varphi_{\mathrm{j}}+\varphi_{\mathrm{k}})} \right|^2 \tag{3.1}$$

where φ_{j} are the relative phases of the electric fields E_j that are emitted. For uncorrelated phases, the terms in the second sum of equation 3.1, $\propto N^2$, tend to interfere destructively, and the power scales linearly with the number of electrons. The afore discussed microbunching in a FEL assures that $\varphi_j \approx \varphi_k$ for all electrons, giving rise to the much larger coherent term (second sum on the right hand side) in equation 3.1, scaling with N^2 [100].

With typical electron numbers of $N \approx 10^9$, this so-called *high-gain FEL interaction* produces photon pulses that have a 10^9 times higher peak brilliance as compared to third-generation synchrotron radiation sources (such as PETRA III at DESY). The whole process is initiated by spontaneously emitted photons at the beginning of the undulator structure, and is named self-amplified spontaneous emission [103].

The local increase in electron density during the SASE process due to the exchange of energy from the electrons to the radiation field continues up to the point where the electrons regain energy from repulsion and re-absorb energy from the radiation field, thus, reaching an equilibrium. A parameter that describes this saturation effect is the *gain length*, i.e. the typical distance traveled in the undulator where the power of the emitted radiation increases by a factor of e.

Since only specific wavelengths that propagate ahead of the electron by an integer number n of the wavelength over the length of one undulator period λ_{U} will constructively interfere, the n-th harmonic of the resonant radiation wavelength is given by:

$$\lambda_{\mathrm{n}} = \frac{\lambda_U}{2n\gamma^2} \left(1 + \frac{K^2}{2} + \gamma^2\theta^2 \right) \tag{3.2}$$

where θ is the radiation opening angle to the beam axis.

The wavelength of the photons generated in the undulator, can thus be controlled by the amplitude and the periodicity of the magnetic field in the undulator, as well as by the energy of the electrons entering the undulator. This enables the precise

tunability of the photon energy and represents one of the key features of FELs. The wavelengths produced by FELs range from 10.6 μm [96] for the first FEL build in 1975, to new machines, such as the LCLS, operating in the X-ray regime at wavelengths of 1.2 Å and even below, if one considers higher harmonics that are also produced in the undulator [90].

Due to the finite length of the undulator, the bandwidth of the n-th harmonic radiation produced in the undulator is given by:

$$\frac{\Delta\lambda_{\mathrm{n}}}{\lambda_{\mathrm{n}}} = \frac{1}{n\,N_{\mathrm{U}}} \tag{3.3}$$

where N_{U} is the number of undulator periods.

Because of the statistical nature of the initial SASE process, most of the parameters of the FEL radiation can fluctuate significantly on a shot-to-shot basis [104, 105, 106], as discussed in the following. Operation schemes to improve these properties are a very active field of research and development today. Among other approaches, seeding by external lasers in the UV and XUV wavelength regions [107, 108], as well as schemes like the so-called self-seeding scheme in the X-ray region are developed. The latter uses the light, produced in a first group of undulators, and a subsequent monochromator to seed lasing in a second group of undulators at a certain well-defined wavelength. This self-seeding scheme was recently designed and tested at the LCLS [109, 110].

3.1.3 FEL Photon Beam Parameters

The SASE based Free-Electron Lasers in operation today have unique properties providing intense, coherent radiation in pulses of lengths between a few and some hundred femtoseconds. Although, the statistical nature of the SASE process introduces shot-to-shot fluctuations of some parameters, the properties of statistical averages can be described well. The LCLS facility offers elaborated machine diagnostics necessary to monitor the pulse parameters, and to control experimental conditions. This enables correction or sorting of the data with respect to the parameters of interest. The parameters and the diagnostic tools, that were used in the analysis of the measurements reported in this work, are discussed in the following.

Photon Energy

As expressed by equations 3.3 and 3.2, FEL radiation has a finite bandwidth around an adjustable photon energy. At the LCLS, this bandwidth is between 0.2 % and 1 % of the nominal photon energy with a jitter of 0.2 % (rms). The photon energy of the fundamental can be tuned from 300 eV to 10 keV [90].

Pulse Length

One of the main new features of X-FELs is the availability of ultra-short pulses with a pulse length of less than 100 fs, possibly even going down to $\sim$ 1 fs duration [111]. These short pulses allow the study of ultra-fast phenomena that happen on a time scale of a few femtoseconds, using wavelengths that are on the order of a few Ångstrom.

Intense FEL pulses contain 8 orders of magnitude more photons per pulse than fs pulses which can be generated at 3rd generation synchrotrons by the so-called slicing technique [112, 113]. The synchrotron-based designs use $\sim$ 50 - 100 fs laser pulses to modulate the energy of a slice of the electrons, out of the few tens of ps long electron bunch, producing $\sim$ 100 fs long synchrotron pulses. Synchronization with optical lasers was also demonstrated in a laser pump, X-ray probe experiment, reaching 85 fs (rms) time resolution [114].

Other sources of coherent soft and in future even hard X-ray pulses is by means of optical laser driven high-harmonic generation (HHG). At photon energies < 100 eV, these pulses can be as short as a few tens of attoseconds and contain typically not more than 10^6 photons per pulse (train) at repetition rates reaching the 10 kHz regime. Recently, a keV-broad continuum has been generated by HHG [115] nurturing the vision to generate few-attosecond keV photon pulses, naturally synchronized with the generating IR laser such that this technique might become competitive or at least complementary, if one thinks about ultra-fast time scales.

When talking about temporal pulse lengths at FELs, there are two types of pulses to distinguish. First, there is the electron bunch that passes the undulators (as described in section 3.1.2) and second, there is the photon pulse that is generated in the undulators. These two kinds of pulses are closely related to each other – most obviously by the fact that the electron pulse-length gives an upper limit to the length of the photon pulse which is produced by the electrons.

Measuring the length of FEL photon pulses is a challenging task. One of the methods employs splitting the FEL pulse into two parts and delaying one part with respect to the other. By scanning the respective delay between the two pulses and looking at a signal that has a non-linear dependence on the FEL intensity, as discussed later, an autocorrelation spectrum can be taken. This was done at FLASH in the XUV range by studying multi-photon induced fragmentation of N_2 [116].

In the X-ray regime, very challenging requirements on the optical setup have so far hindered an all X-ray autocorrelation measurement of the pulse length even though respective beam-splitters are under construction. However, an X-ray-optical cross-correlation measurement was performed at the LCLS, showing that electron bunches of durations of 75 fs and 175 fs produce effective X-ray pulses of 40 fs and 120 fs length, respectively [117]. This is in agreement with earlier findings by comparison of experimental data and simulations on yields from higher-order photoabsorption processes [22]. So far, the cross-correlation is not part of the standard diagnostic tools available to users at the LCLS and only the electron bunch lengths can be controlled and measured online.

FEL Pulse Intensity

Many effects that are studied with X-FELs are dependent on the number of photons that interact with the sample in a given time window. In principle, there are three main values that define most FEL pulse characteristics.

The *pulse energy* E_{pulse} is given by:

$$E_{\text{pulse}} = N_{\text{photons}}\,\hbar\omega \tag{3.4}$$

where N_{photons} is the number of photons and $\hbar\omega$ is the energy of a single photon.

The *fluence* Φ takes into account the focus area A_{focus} and is given by:

$$\Phi = \frac{E_{\text{pulse}}}{A_{\text{focus}}} \tag{3.5}$$

The *pulse intensity* or irradiance I_{pulse} includes the pulse length Δt_{pulse} and is given by:

$$I_{\text{pulse}} = \frac{E_{\text{pulse}}}{\Delta t_{\text{pulse}}\,A_{\text{focus}}} \tag{3.6}$$

The LCLS pulse energy is parasitically measured on a shot-to-shot basis by the

Gas Energy Detector (GED), which is installed before the beam enters the experimental hutches. It consists of four detectors, a pair of which is placed in the beamline before and after the attenuation setup. This allows for the simultaneous measurement of both, the incident beam and the attenuated beam pulse energy for individual single FEL shots.

The measurement of the pulse energy is performed using X-ray induced photoluminescence of N_2 [118]. The device consists of a 30 cm long chamber that can be filled with nitrogen up to a pressure of 2.5 mbar, regulated by a gas inlet. Due to the low density of the gas the total amount of absorbed photons is very low (0.06% for 8.3 keV photons). This allows for the use of the GED as an online diagnostics that does essentially not affect the beam proceeding to the experiment. The photons are mainly absorbed through K-shell photoionization of N_2 followed by a fast Auger relaxation cascade. In order to confine both, the photo- and the Auger-electrons and thus increase luminescence, a 200 Gauss magnetic field, produced by an external solenoid, is used. The excited molecular nitrogen relaxes via radiative decay producing ~ 300 nm to ~ 400 nm photons [118]. This ultra-violet (UV) light is then amplified and detected by two photo multipliers installed parallel and perpendicular to the FEL polarization vector. A near-UV filter allows only the transmission of wavelength between 300 nm and 390 nm [119]. From the amount of measured UV photons, the pulse energy can be derived using a calibration curve, where gas pressure, magnetic field and photon energy have to be taken into account. The calibration of the GED is done by comparison with the electron beam loss, i.e. the difference in electron beam energy before and after the undulator.

Pulse energy attenuation is provided as a way to control the pulse energy at the target. At the LCSL, attenuation of the photon pulses is achieved by two different measures, where the attenuation level is, in both cases, dependent on the photon energy because the absorption cross sections are changing as a function of energy.

First, there are several solid-state attenuators, i.e. seven beryllium plates of several thicknesses (2×0.5, 1, 2, 4, 8 and 16 mm), that can be inserted into the beam path separately. This results in an adjustable total attenuator length of beryllium from 0 to 32 mm, in 0.5 mm steps, corresponding to at least 3 steps for every decade of attenuation. The second measure available to attenuate the beam is a gas-cell of 4.5 m length, that can be filled with N_2 up to a pressure of 16 mbar. This results in an attenuation of up to a factor of 10^3 at 1.5 keV photon energy [120].

FEL Beam Transport, Transmission, and Focus Size

The number of photons, interacting with the target, depends on the total number of photons in the pulse, but also on the spatial properties of the photon beam and the target. These include wave-front and focus shape, where the latter is mostly defined by the optics that deliver the beam to the experiment.

The beam is directed to the AMO beamline using three boron-carbide (B_4C) coated silicon mirrors. Horizontal as well as vertical focusing is achieved by two parabolic-curved gracing incidence Kirkpatrick-Baez (KB) silicon mirrors with the same coating. As the combined reflectivity of these five mirrors drops rapidly for wavelengths smaller than 0.62 nm (photon energies larger than 2000 eV), higher harmonics of fundamental photon energies larger than 1000 eV are effectively suppressed. The transmission of the AMO beamline, from the GED to the experiment, is a machine parameter that is not completely determined by measurements. While calculated values for the total transmission based on the mirror reflectivity at 800 eV, 1050 eV, and 2000 eV photon energy are 0.663, 0.699, and 0.584, respectively, experiments on gas targets assumed different transmission values in order to reproduce their measurements with theoretical models [22, 24]. In this work, we assume a transmission of 35% at 2 keV and 18-20% at 1.5 keV based on prior experiments on rare gas targets [24, 121].

For experiments that rely on high FEL intensity, the focus size is a crucial experimental parameter. A widely used technique to measure the focus of X-FELs is based on radiation damage inflicted on a solid target placed directly in the focus. These so called *imprint measurements* make use of material-specific ablation thresholds fluences [122]. The size and depth of the ablation can be measured using optical microscopy. If the measurement is repeated at different positions along the beam propagation direction and the pulse energy is measured in addition, this provides information on the focus intensity profile as well as on the Rayleigh length, i.e. the distance from the focal point where the focal diameter is doubled. This focus scan can also identify astigmatism in the beam profile. Other methods to study spacial properties of the FEL beam include pine-hole imaging, luminescent crystals and phosphorescent coated glasses [122]. Recently, coherent scattering off nano-spheres with well-defined diameters has been used to characterize the FEL beam focus as well as its wavefront [123].

Most of the approximations used in these focus investigations however, are strictly

no longer valid if the beam is distorted or non-homogeneous. This can be introduced by mirror surface imperfections [21] or by the SASE process itself. Another effect that has to be considered is that the target particle may not always interact with the center of the focused beam but can also be found at the edges of the beam, where the intensity can be significantly lower. This is especially relevant for gas phase single particle experiments, as has been observed for rare gas clusters [124], but also for fixed targets, as the pointing of the FEL beam is not perfectly stable.

3.2 Ion Coincidence Measurements in the CAMP Instrument

With the unique parameters of Free-Electron Lasers discussed in the last sections, many interesting and novel experiments can be conducted. The new properties of course also imply new experimental conditions and instrumentation requirements, which are, in many aspects, different from experiments using optical lasers or synchrotron light sources. To address the latter, a novel experimental endstation (CAMP) aiming for a simultaneous detection of charged particles, and scattered or fluorescent photons, was designed and successfully employed in numerous experiments showing its great versatility. One specific application of the apparatus, namely the study of photoionization and fragmentation of small molecules using ion-ion coincidence techniques, is presented in this work.

3.2.1 The CAMP Chamber

The *CFEL ASG Multi-Purpose* instrument (CAMP) is designed and operated by a large scientific collaboration led by the *Max Planck Advanced Study Group* (ASG) at the *Center for Free-Electron Laser Science* (CFEL). The properties of this instrument and some of its experimental capabilities are described in reference [125]. This end station allows to combine a large variety of spectrometers and detectors (for example large-area pnCCD photon-detectors and momentum imaging ion or electron spectrometers) with a large variety of possible targets – ranging from single atoms [24] to large biomolecules [18], viruses [14], nanoparticles [16], rare-gas clusters [15], and solid-state samples [126].

An overview of the main CAMP chamber with its dimensions, as well as the main ports for the connection of the spectrometers, detectors, and the target injection devices is presented in figure 3.3. The instrument ports are designed to allow for highest experimental flexibility and for collection of the most complete data sets on simultaneous electron, ion and photon momentum imaging – aiming at large solid angles for all particles.

As the chamber is designed to connect not only to the LCLS AMO beamline (as for the work presented here) but possibly to numerous different beamlines at present and future FEL and synchrotron facilities, the support was designed such that all

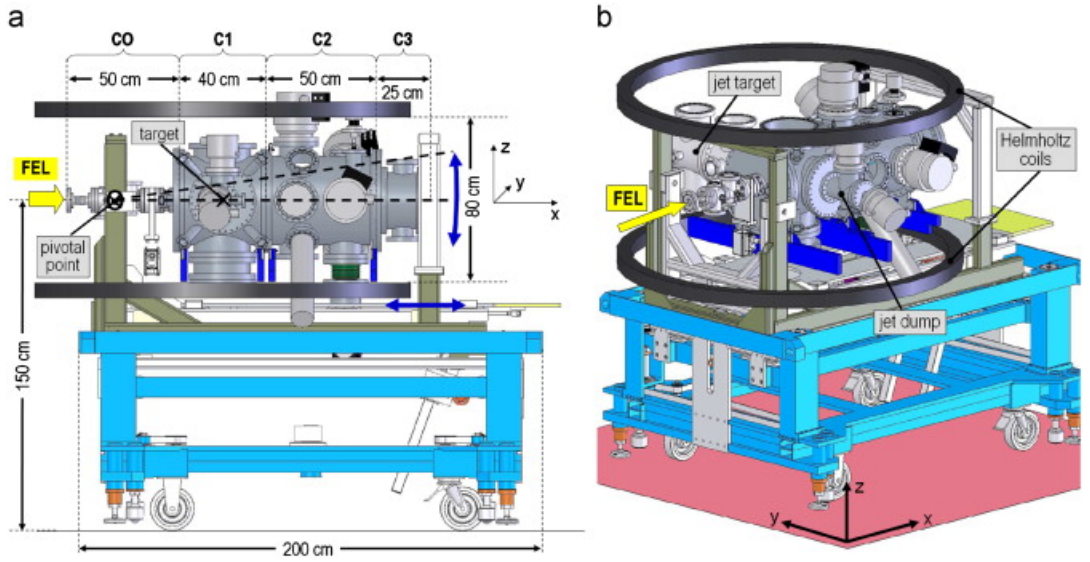

Figure 3.3: Overview of the general dimensions and the setup of the CAMP instrument. The FEL beam is entering the chamber from the left. The vacuum setup consists out of 4 connected chambers. C0 is for differential pumping to the beamline. C1 is the actual interaction chamber of the FEL and the target, and capable of housing a variety of particle detectors and spectrometers. C2 houses a movable set of pnCCD detectors for energy selective detection of scattered or fluorescence photons, while C3 houses an identical but fixed set of pnCCDs.[8]

parts of the experiment can be moved in all three spacial directions and can be tilted in a horizontal and vertical motion around a pivotal point (see figure 3.3[8]) at the connection to the beamline. These motions can be controlled remotely via precision stepper motors.

In the next sections, the specific detectors and target injection system used to conduct the experiments presented in this work are discussed, starting with an overview of the setup and a discussion of experimental requirements.

3.2.2 Setup for Fragmentation Studies of Small Molecules

The experiment presented in this work, aimed at coincident 4π solid-angle detection of multiple high-kinetic-energy ions from small molecules ionized and exploded by an FEL pulse. To achieve this, the following setup was used.

The center piece of the setup is the ion 3D-momentum imaging spectrometer

[8]Source: L. Strüder et al., Nuclear Instruments and Methods in Physics Research Section A: Accelerators, Spectrometers, Detectors and Associated Equipment 614, 483-496 (2010), figure 1, copyright by Elsevier LTD., reference [125].

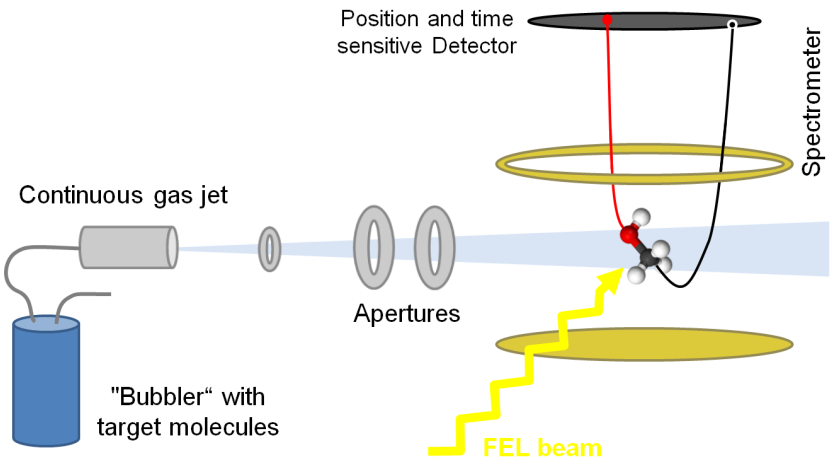

Figure 3.4: Overview of the spectrometer and the target injection setup in the CAMP chamber to perform coincident ion momentum spectroscopy on small organic molecules ionized with an X-ray FEL. The schematics shows the main parts of the setup which are the incoming FEL beam, the continuous gas jet of molecules, and the spectrometer which is built around the interaction point.

(described in section 3.2.4). Inside this spectrometer, as shown in the schematics in figure 3.4, the focused FEL beam is overlapped with a continuous gas jet of molecules. Operation conditions for conducting (ion-)coincidence experiments impose high requirements on the vacuum level, and restrict the target density that can be used. In order to be able to measure several ionic fragments originating from a single molecule, and avoid having events that result from more than one molecule (false coincidences), the number of ionization events per shot has to be kept low. To achieve a 95% probability of true coincidences, the average number of ionized molecules per shot should be below 0.35, according to Poisson statistics (also see [127]). To keep the ionization rate low, either the target density or the number of ionizing photons has to be reduced – while the latter is not favorable for the study of multiple photon absorption effects, since they depend non-linearly on the number of photons per pulse.

Ions are not exclusively produced from the target molecule but also from the ionization of residual gas in the vacuum chamber. Due to the fact that high-energy photons of X-ray FELs easily ionize any material in the chamber with just a single photon, maintaining a low vacuum pressure is crucial. Compared to optical laser setups, where a lot of photons are needed to ionize – a condition only realized in a

small focal volume – the ionization in the X-ray case can happen anywhere along the beam path or can even be caused by stray-light away from the direct trajectory of the beam eventually increasing the amount of unwanted background signal to an intolerable level.

On the other hand, the significant reduction of the absorption cross sections far above the deepest absorption edges of light elements ($Z < 10$) relaxes vacuum requirements for the experiments at keV X-ray FELs compared to similar measurements at VUV or XUV frequencies. For typical elements in the rest-gas, namely nitrogen, oxygen, and carbon, the photoionization cross sections (at 2 keV photon energy) are 11.07 kbarn, 18.43 kbarn, and 6.017 kbarn, respectively. Considering the large number of photons in the beam ($N_{\text{photons}} \approx 10^{12}$ photons per pulse), the amount of unwanted ions produced can be substantial.

The number of ionization events N_{events} inside the spectrometer is given by:

$$N_{\text{events}} = \rho_{\text{gas}}\, l_{\text{spec}}\, \sigma\, N_{\text{photons}} \tag{3.7}$$

Assuming a cross section $\sigma = 10\,\text{kbarn}$ and an interaction length $l_{\text{spec}} = 80\,\text{mm}$ through the spectrometer two ionization events occur per pulse, for a residual pressure of $1 \cdot 10^{-9}$ mbar. Thus, in the experiments at the LCLS presented in this work, a background pressure of less than $3 \cdot 10^{-10}$ mbar was achieved, using several turbo-molecular pumps and a cryo-pump.

3.2.3 Cold Molecular Jet

In order to produce a cold jet of target molecules for this experiment, a system consisting of a gas-mixing cell, a so-called bubbler, and a continuous supersonic jet was used. The components of this assembly are described in detail below.

The Supersonic Jet used in this work provides a continuous beam of cold target atoms or molecules. This is realized by expanding gas from a reservoir of high pressure p_{gas}, which is in this case either the bubbler vessel or a gas bottle, into a volume of low pressure p_{vacuum}. Is the ratio between the two pressures $p_{\text{gas}}/p_{\text{vacuum}}$ higher than ~ 2, the expansion happens such that the speed of the gas particles is larger than the local speed of sound, e.g. a supersonic expansion is realized, and the expansion process happens adiabatically.

Then, for an ideal gas under optimum conditions, the free enthalpy plus the kinetic thermal energy is transfered into kinetic energy in the beam direction in the following way:

$$E_{\text{thermic}} + pV = 3/2Nk_BT + Nk_BT = 5/2Nk_BT = 1/2m\vec{v}^2 \tag{3.8}$$

producing a fast and internally (in the moving reference frame) cold beam. The velocity of an ideal atomic gas jet thus is:

$$v_{\text{jet}} = \sqrt{5k_bT/m} \tag{3.9}$$

where m is the mass of a gas particle. For the case of helium ($m \approx 4\,\text{amu}$) at room temperature, the jet velocity is $v_{\text{jet}} \approx 1700\,\text{m/s}$. This momentum component in the jet propagation direction has to be considered in the analysis of the momenta of the particles as it introduces an offset.

The target jet has to be cold in order to keep the thermal distribution of momenta of the molecules narrow which otherwise can affect the momentum resolution of the measurement. Moreover, a cold jet reduces the internal vibrational and rotational energies of molecular targets, preparing them in less excited state, which improves the accuracy of the molecular geometry measurements through ion kinetic energies.

The interaction of the expanding gas with the gas in the expansion chamber has to be considered as well. The supersonic jet creates a shock wave that compresses the residual gas. Only before the first shock, e.g. in the so-called *zone of silence* the gas can expand freely. The distance of this shock front, the Mach disk, is calculated by

$$d_{\text{machdisk}} = \frac{2}{3} d_{\text{nozzle}} \sqrt{\frac{p_{\text{gas}}}{p_{\text{vacuum}}}} \tag{3.10}$$

where d_{nozzle} is the diameter of the jet nozzle through which the gas is expanded [128]. To preserve the cooled beam, the inner part has to be cut out by a skimmer at less than the Mach distance away from the nozzle.

In the present setup (see figure 3.5) this is done using a $180\,\mu$m skimmer placed at a variable distance of 0 to 20 mm away from the nozzle opening that has a diameter of $30\,\mu$m.

As the jet is operated continuously, the gas load in the first chamber after the continuous nozzle is significant. To ensure that the UHV in the main chamber is

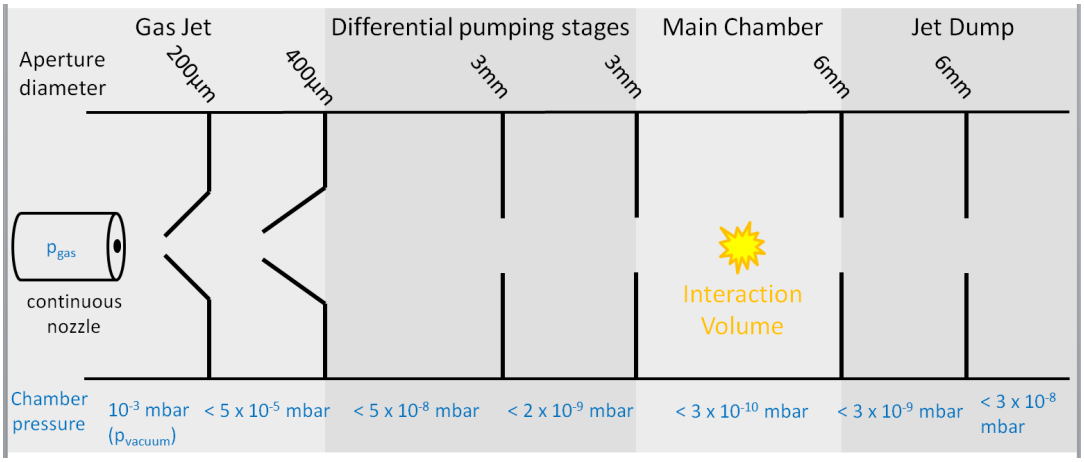

Figure 3.5: Schematics of the supersonic gas jet and the apertures to collimate the particle beam.

not affected and to collimate the beam, a second skimmer with a 400 μm diameter limiting the transversal momentum of the particles, is placed 18 mm away from the first one. Two further, downstream apertures of $\varnothing$3 mm are used to create a set of two differential pumping stages before the main chamber. This way, a pressure difference between $\sim 5 \times 10^{-4}$ mbar in the first stage of the jet and $\sim 2 \times 10^{-9}$ mbar in the last differential pumping stage before the main chamber can be realized. In the main chamber, a pressure of $\sim 3 \times 10^{-10}$ mbar was achieved. The diameter of the jet inside the spectrometer was less than 4 mm and kept small in order to limit the size of the interaction volume with the FEL beam. After passing through the spectrometer the jet enters the so-called jet-dump through a $\varnothing$6 mm aperture. It consists of two differential pumping sections that are separated from one another by another $\varnothing$6 mm aperture and are capturing the beam to reduce the gas load on the main chamber.

The Bubbler is a liquid containing pressure vessel where vapor from the liquid target can be mixed with a carrier gas – in this case helium. A schematic of the setup is depicted in figure 3.6. The flow of vapor from the bubbler is directly related to the vapor pressure in the vessel which is a function of temperature and depends on the characteristics of the liquid. An example of a vapor pressure curve for the case of methyliodid is given in figure 3.6. Values for the boiling temperature and the vapor pressure, of the target molecules used in this work are given in table 3.1.

As the vapor pressure strongly depends on the temperature of the liquid, a conve-

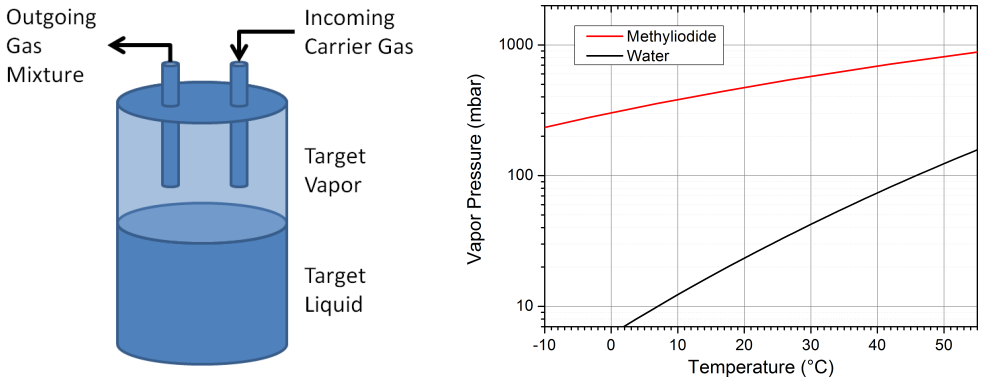

Figure 3.6: Bubbler schematics and vapor pressure curve for methyliodide and water.

Target Molecule	Boiling Temperature [°C]	Vapor pressure at 25°C [mbar]
Methylselenol	24	1044
Ethylselenol	29	869
Iodine chloride	97	42
Methyliodide	64	540

Table 3.1: Boiling temperature and vapor pressure at room temperature for the molecules studied in this work.

nient control of target flow is possible by external temperature regulation. However, high temperatures can also cause chemical degradation of the target substance which has to be considered. Another way to control the flow of the target into the jet is by controlling the carrier gas flow. This is conveniently done by using a pressure regulator in order to change the pressure ratio between the target vapor and the carrier gas. However, for most of the molecules used in this work, it turned out to be sufficient to connect the bubbler, containing the liquid target directly to the gas jet without the use of additional carrier gas. This method works well for some small molecules because of their high vapor pressure at room temperature, as listed in table 3.1, at moderate expansion conditions such that cluster formation is sufficiently suppressed.

3.2.4 3D-Momentum Imaging Ion Spectrometer

High-resolution momentum spectrometers were first developed for ion-atom collision experiments [129]. They allowed for the measurement of the target-ion recoil momentum with resolutions sufficient to resolve momentum transfers from the ejected electrons. To resolve this small momentum transfer, the target gas has to be cold, as described above, which led to the *cold target recoil momentum spectroscopy* (COLTRIMS) technique. If the electrons are detected in addition to the ions, a so-called *reaction microscope* (REMI) is realized [130]. Today, these instruments are used for a broad variety of experiments investigating atomic and molecular dynamics, for example in photoionization, intense- or attosecond laser interactions etc. [130]. Here, the fragments are extracted by a combination of constant electric and magnetic fields. Thus, ions are accelerated towards one side of the spectrometer onto one detector, whereas electrons are projected onto a second detector sitting on the other end of the spectrometer. This allows to conduct *kinematically complete experiments* where the momentum components of all fragments in their final state can be measured [130].

In the experiment presented in this work, only the ions produced in the reaction were detected with the specially designed spectrometer described in the following section.

3.2.4.1 Spectrometer Parameters

The spectrometer shown in figure 3.7 is divided into two main parts, an extraction and a drift region, separated by a copper mesh. In the extraction regime, a constant electric field is created between grid 1 and grid 2 by nine equally spaced electrodes. Each electrode has a thickness of 1 mm and is made of aluminum with a gold-plating to avoid voltage-inhomogeneities caused by insulating aluminum oxide layers. The individual electrodes are held by two aluminum spacers that are isolated towards the next electrode by ceramic (AlO_3) discs and the distance between two electrode surfaces is 9 mm. In order to apply potentials to each electrode, creating a homogeneous electric field, without contacting all electrodes individually they are interconnected using resistors (2MΩ), thus creating a voltage divider.

The ions are produced in the center of the extraction region where the FEL beam and the target jet overlap. The second region of the spectrometer is between the

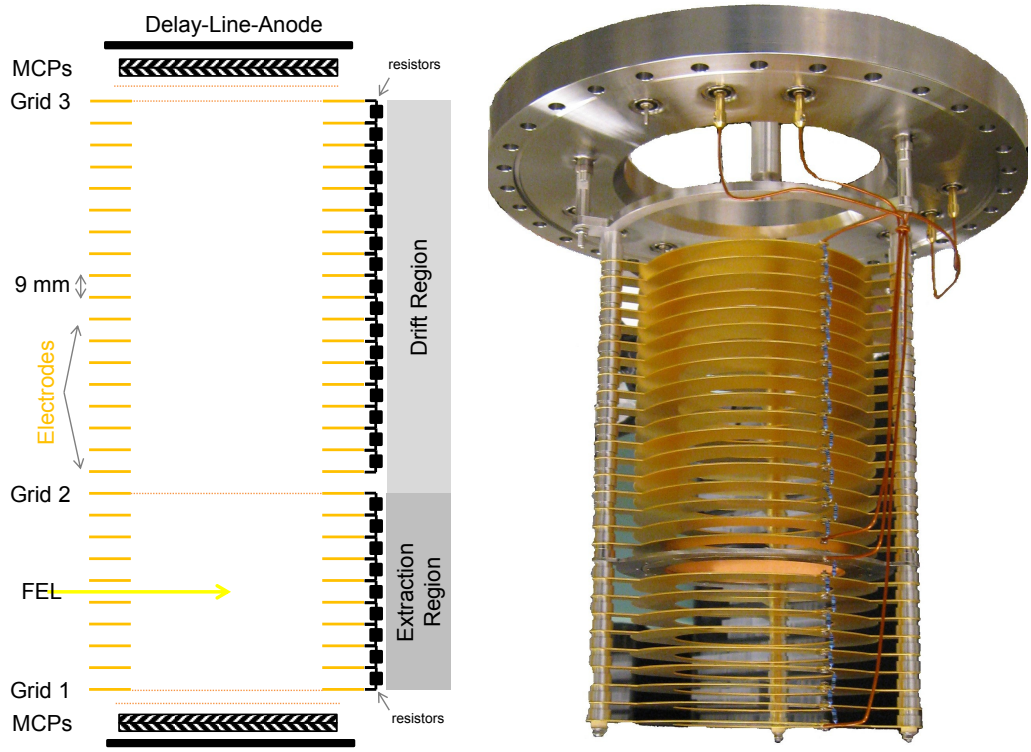

Figure 3.7: Schematic of the spectrometer (left) and photograph of the assembled spectrometer (right).

center grid and the first grid of the far detector. This region can either be used as a second acceleration region, or, as it has been used in this work, as a field-free drift region. Which increases the difference in flight time between different ion species, thus increasing the time resolution of the spectrometer. To avoid field inhomogeneities the ends of the spectrometer are closed by grids.

The spectrometer axis, i.e. the axis connecting the two detectors at each end of the setup, is oriented perpendicular to both the FEL beam propagation and the gas-target jet direction. At the LCLS, the X-ray beam is linearly polarized, with the polarization direction parallel to the the gas jet.

3.2.4.2 Time- and Position-Sensitive Detectors

The charged particles are detected by a combination of *microchannel plates* and *delay-line anodes* [131]. With this combination, the flight-time and the impact position of the ions on the detector can be simultaneously determined. The two afore mentioned main parts of the detector will be explained in more detail in the

following.

Microchannel Plates (MCPs) are thin high-resistance glass plates with millions of small parallel capillary tubes that are tilted with respect to the surface. Both sides of these plates are coated with low-resistance material allowing to apply high voltage across the plate and along the micro-channels. Impacting (charged) particles – with sufficient energy – create secondary electrons in the capillary. These secondary electrons are accelerated by the field applied transverse to the plate along the channels and can gain enough energy to produce more electrons upon impact on the walls. For a typical voltage of 1 keV over a single plate, the cascade triggered by one particle can produce 10^3 to 10^4 secondary electrons (amplification factor).

In the setup used in this work, the amplification was done with a stack of two MCPs in a chevron configuration, where the capillaries of the two plates are forming a V-shape. This configuration increases the detection efficiency, as no particles can fly directly through the capillaries without hitting the walls, which also suppresses ion feedback, and doubles the amplification to a total factor of 10^7. The emission of secondary electrons leads to a short voltage breakdown over the MCP that can be coupled out using a capacitor and fed into an oscilloscope to serve as a time-signal for a detected particle (see section 3.3.2).

The detection efficiency of the MCP is determined by the ratio of total area covered by capillaries versus the rest of the detector area. This is between 50% and 60%. Together with the 78% transmission of the grids, with a wire thickness of 30 μm and a grid-width of 224 μm, the total theoretical detection efficiency for charged particles is $\sim 30\%$.

Delay-Line-Anodes were used to determine the position where a particle hits the detector. Here, the secondary electrons emitted from the back of the MCP are collected on an arrangement of orthogonal double-wires called "delay-lines" (see figure 3.8[9]), where they produce voltage pulses that propagate along the double-wires (Lecher-Line) in both orthogonal directions until they are detected at times t_1 and t_2 at both ends of each Lecher-Line, respectively. As the propagation speed is constant, the position X where the electron cloud did hit the respective wire can be

[9]Source: I. Ali et al., Nuclear Instruments and Methods in Physics Research Section B: Beam Interactions with Materials and Atoms 149, 490-500 (1999), figure 2, copyright by Elsevier LTD., reference [131].

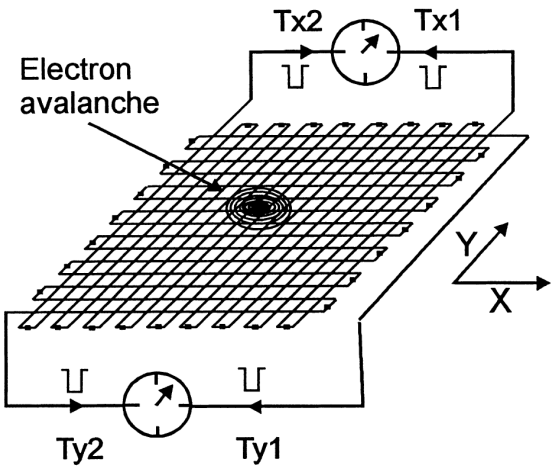

Figure 3.8: The function principle of the delay-line-anode. The position where the electron avalanche cloud from the MCPs hits the anode is obtained from the signal propagation time along the wires.[9]

calculated from the arrival-time difference of the two signals:

$$(t_{x,1} - t_{x,2}) \sim X \tag{3.11}$$

For the measurements presented in this work, a quadratic delay-line detector from the company RoentDek [132] was used. In this setup, two sets of wire-pairs that are oriented perpendicular to each other are used to determine the X and Y positions on the detector. For more detailed information see reference [131]. The spatial resolution is not limited to the distance between the wires, but can be further increased by interpolation of the signals from different wires and a position resolution of 0.1 mm is achievable. As described, for each direction, the delay-line consists of two separate wires, forming a so-called *Lecher-Line* that reduces the impedance for high-frequency signals and enables reduction of electronic noise by inherent subtraction.

3.3 Data-Acquisition and Analysis Techniques

In this section, some data analysis methods used in this work are briefly addressed. This includes the basic data-handling that is used to process the "raw" data, as well as algorithms to correlate and present the observed variables. Specific techniques such as ion time-of-flight and coincidence spectroscopy are introduced. The correlation of the data from the spectrometer with the LCLS parameters as well as the main data processing was carried out using the *CFEL–ASG Software Suite* (CASS) [133].

3.3.1 LCLS Machine Data

The machine data that is recorded at the LCLS includes both, fast data that is collected for every shot, such as photon-energy, pulse-energy, etc., as well as slow data, collected at 1 Hz which includes voltages, pressures and other settings of various control devices. While the slow data is useful to control experimental parameters over the course of longer measurements, the fast data can be used to correct the information collected on a shot-to-shot basis.

3.3.2 Time-of-Flight Spectrum – Single-Ion Yield

Time-of-flight (ToF) spectra are a basic tool to determine the mass-to-charge ratio of ions produced in an ionization process and to measure the particle momentum component parallel to the spectrometer axis. The signal can be directly measured using the spectrometer described in section 3.2.4 by decoupling the signal from the MCP voltage supply through a capacity.

The flight time t_{ToF} of the measured ions is proportional to the mass m and the charge q in the following way:

$$t_{\mathrm{ToF}} \propto \sqrt{\frac{m}{q}} \tag{3.12}$$

By knowing the possible masses of the (ionic) fragments, the peaks at different times in the time-of-flight spectrum can be allocated to ions with their respective masses and charge states. A ToF-spectrum for the case of air, containing N_2 and O_2, is shown in figure 3.9. This spectrum shows ions of oxygen and nitrogen with charge states ranging form $q = 1+$ to $q = 3+$. An example of a detailed calibration of a time-of-flight spectrum to the mass-to-charge ratio and the further analysis is given in the following paragraph.

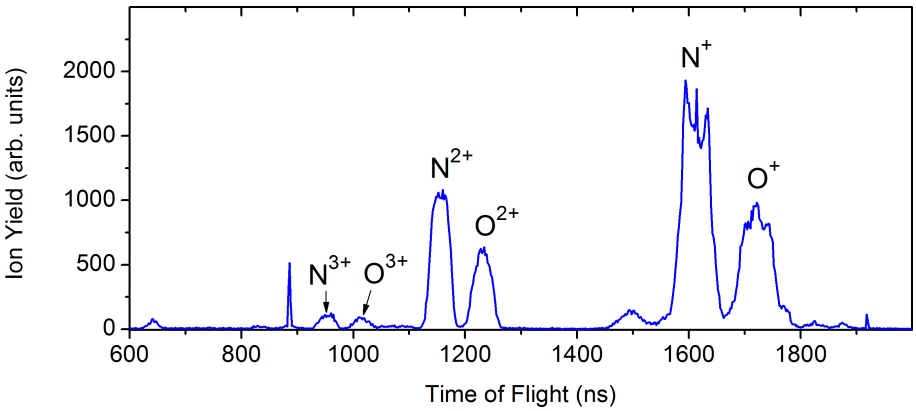

Figure 3.9: Example of a ToF spectrum of N_2 and O_2.

Calibration of a ToF Spectrum

A precise way to calibrate a ToF-spectrum is to simulate the flight times of all fragments measured in the experiment taking into account the geometric and electrical properties of the spectrometer. As the fields are either constant or zero for all the parts of the spectrometer, the simulation formula achieved is the following:

$$t_{\mathrm{ToFsim}} = t_{\mathrm{offset}} + \sqrt{\frac{m_{\mathrm{ion}} d_{\mathrm{extraction}}}{2\, q_{\mathrm{ion}} U_{\mathrm{extraction}}}} \left(\sqrt{4x_1} + \sqrt{\frac{x_2^2}{x_1}} \right) \tag{3.13}$$

where $d_{\mathrm{extraction}}$ and $U_{\mathrm{extraction}}$ are the length and the applied voltage over the extraction region, x_1 is the flight distance the ion travels along the spectrometer axis inside the extraction field, x_2 is the length of the drift region, and t_{offset} is the difference between the detector trigger timing and the time the laser pulse hits the target.

This yields a calibration curve of t_{ToFsim} versus $\sqrt{m/q}$ that can be directly compared to the measured t_{ToF}. From this curve, all the fragments can be directly identified from the modeled spectra.

To extract the ion yield, i.e. the number of ions, of certain species one can integrate over the respective ToF peak(s). This can be either done for all the isotopes (if there are several natural isotopes) or for a specific isotope only.

3.3.3 3D-Momentum Coincidence Spectroscopy

With the use of ToF spectra, all the ions produced in the interaction can be determined. However, as a molecule consists of several atoms, a way to determine

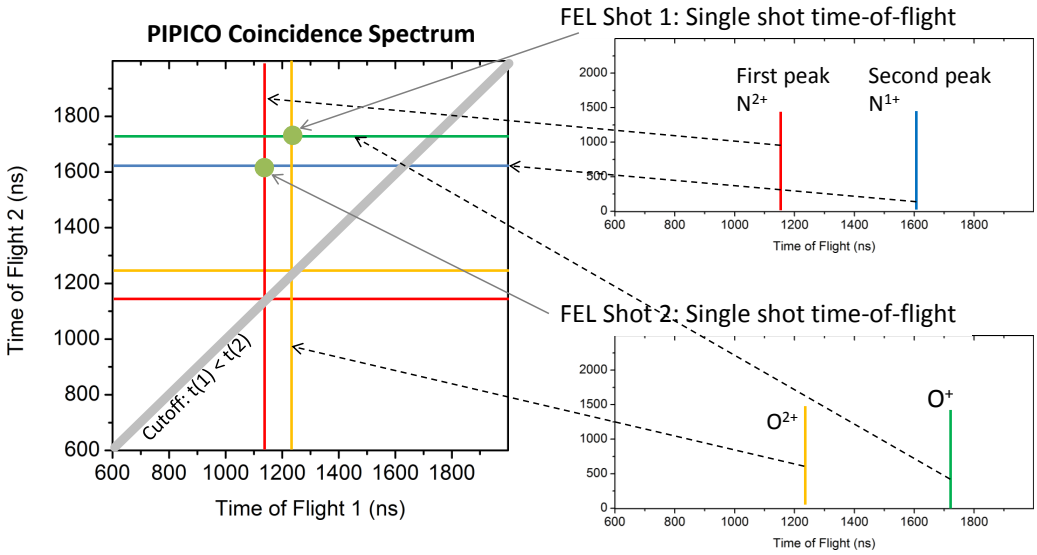

Figure 3.10: Example of how a PIPICO-spectrum is created from single-shot ToF traces (after CFD) in the case of nitrogen (N^+N^{2+}) and oxygen (O^+O^{2+}) ion coincidences.

specific fragmentation channels of the molecule, for example the breakup of N_2 into $N^{2+} + N^{3+}$, is needed.

An easy way to pick out specific fragmentation channels of diatomic molecules is by means of a so-called photoion-photoion-coincidence spectrum (PIPICO) that directly shows ion-ion coincidences. In this method the time of flight of the first arriving ion is plotted against the flight time of the second one on a shot-by-shot basis, as illustrated in figure 3.10.

The coincident fragmentation channels form sharp lines in this spectrum that reflect the conservation of total momentum in the Coulomb explosion process, since the sum momenta of the emitted electron as well as of the photons absorbed are comparably small.

Events, where more than one molecule was fragmented and fragments are detected, produce ion pairs that are uncorrelated and form a washed out background underneath the sharp lines as shown for the case of N_2 in figure 3.11. As discussed earlier, this background of "false coincidences" can be reduced by reducing the total number of ionization events, thus, increasing the relative probability of only one molecule being ionized in a single FEL pulse, rather then producing several ionized

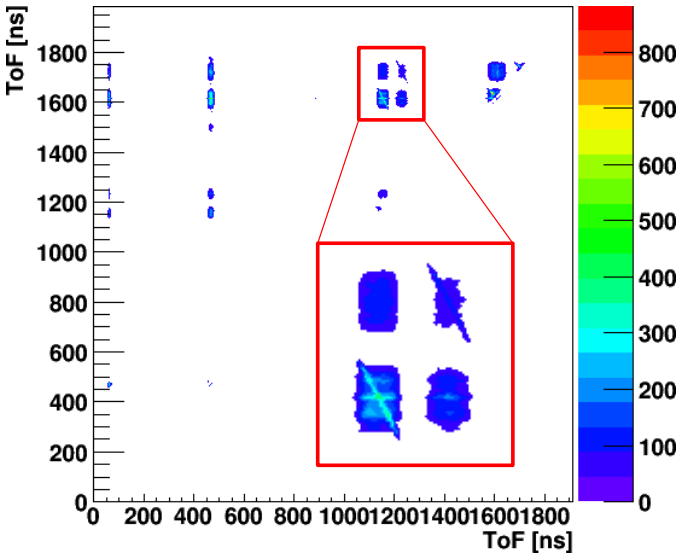

Figure 3.11: Example of a PIPICO-spectrum for air jet of N_2 and O_2 where the individual fragmentation channels can be identified as tilted sharp lines.

molecules in one shot.

Another reason for broad coincidence lines in the PIPICO spectrum is dissociation into more than two ionic fragments for larger molecules. In these cases conservation of momentum between the two detected fragments is no longer given and the width of the line is directly correlated to the momenta of the undetected fragments.

In order to filter the data for a certain fragmentation channel by way of two-fold coincidence, first two time-of-flight windows are set for the targeted ions, respectively. Next, the sum of the momenta of the two ions has to be in a small window around zero. By applying these conditions, one can select every fragmentation channel identified in the PIPICO spectrum and do further data analysis only on the data corresponding to this channel – meaning on a dataset containing mostly events where a certain final charge state of the target molecule was measured. In the following, this will be called a fragmentation channel or sometimes the final charge state of the molecule. An example would be $Se^{2+}C^{+}$ for the measured coincidence of a selenium $q = 2+$ ion and a carbon $q = 1+$ ion.

In the same fashion, filters for isotopes can be implemented as they have a different mass and form a separate line in the PIPICO spectrum.

Calculating Ion Momenta

By utilizing a position- and time-sensitive detector system as described in section 3.2.4.2, it is possible to reconstruct the 3D momentum vector of the detected charged particle in the following way.

For each particle, the position on the detector (X, Y) and the time of impact t is known. By calculating the kinetics of charged particle in a homogeneous electric field, the position on the detector can be calculated:

$$X = \frac{P_{\mathrm{x}}}{m}t \tag{3.14}$$

$$Y = \frac{P_{\mathrm{y}} + P_{\mathrm{jet}}}{m}t \tag{3.15}$$

$$Z = \frac{E_{\mathrm{a}}qt^2}{2m} + \frac{P_z}{m}t + Z_{\mathrm{drift}} \tag{3.16}$$

where X, Y, are the positions on the detector (relative to center) and Z is the distance from the interaction point to the detector. P_{x}, P_{y}, and P_{z} are the particle momenta, m is the mass of the particle, E_{a} is the accelerating electric field and Z_{drift} is the length of the drift tube. The asymptotic momentum vectors can then be calculated by solving these equations for P_{x}, P_{y}, and P_{z}. With the information of $(P_{\mathrm{x}}, P_{\mathrm{y}}, P_{\mathrm{z}})_{\mathrm{i}}$ for several particles measured in coincidence, angles between ion trajectories and correlated kinetic energies can be studied.

Chapter 4

Multiple Ionization of Small Molecules in Intense X-Ray FEL Pulses

In this section, the results obtained during two measurement campaigns at the LCLS are presented. The data were taken using the CAMP chamber at the AMO beamline with the setup described in detail in the previous chapter.

The atomic and molecular targets studied in this work are listed in table 4.1.

Sample Name	Chemical Formula	Ionized Shell / Photon Energy	Section
Krypton	Kr	Kr L (2s, 2p) / 2000 eV	4.1
Methylselenol	CH_3−SeH	Se L (2s, 2p) / 1700 eV, 2000 eV	4.2
Ethylselenol	CH_3−CH_2−SeH	Se L (2s, 2p) / 1700 eV	4.3
Xenon	Xe	Xe M (3s, 3p) / 1500 eV, 2000 eV	4.4
Iodine Chloride	Cl−I	I M (3s, 3p) / 1500 eV, 2000 eV	4.4
Methyl Iodide	CH_3−I	I M (3s, 3p) / 1500 eV	4.5

Table 4.1: List of the samples investigated in this work. The chemical formula show the composition of the molecular constituents. The "ionized shell" indicates the electronic shell of the atom (in the molecule) that has the highest partial photoabsorption cross section for single photon absorption.

As discussed in the introduction, a specific class of molecules containing a single high-Z atom, namely selenium or iodine, was chosen for this study. The high photoabsorption cross section of the heavy atom constituent results in overall high ionization of the molecule and ensures that initial photoabsorption is localized. This allows studying the influence of the molecular environment on multiple X-ray ionization, subsequent charge redistribution mechanisms, and the role of intra- and interatomic decay mechanisms. To highlight the effects of the molecular partners, isolated atomic species with similar absorption cross sections and electronic structure, namely krypton and xenon, were studied under the same experimental conditions.

4.1 Multiple Ionization of Krypton

Before the more complex molecular systems with heavy atom constituents are studied, some basic processes induced by intense ultra-short X-ray pulses are discussed for isolated krypton atoms. As mentioned above, these results also provide a natural reference data set for the later discussion of similar processes in selenium-containing molecules.

Charge State Distribution

Figure 4.1 shows an ion time-of-flight spectrum for atomic krypton taken at an FEL pulse length of 5 fs (nominal), a photon energy of 2 keV with a mean pulse energy of 0.4 mJ (0.2 mJ FWHM), corresponding to a fluence of $\sim 15\,\mu\mathrm{J}/\mu\mathrm{m}^2$, or an intensity of $3 \cdot 10^{17}\,\mathrm{W/cm}^2$.

The charge states with the highest abundance are Kr^{5+} and Kr^{6+}, whereas the highest charge state observed is Kr^{16+}. Comparing these results with earlier measurements for single photon absorption [134, 135, 136, 137], where charge states up to Kr^{8+} were observed, it is clear that, although single photon absorption processes still dominate, pronounced multi-photon contributions are present. In particular, the charge states above Kr^{8+}, which are not present in the single photon spectra, are an unambiguous indication for multi-photon effects.

The number of photons absorbed by a single krypton atom to reach a certain final charge state can be experimentally determined by measuring the ion yield of this charge state as a function of FEL pulse energy, which is proportional to the pulse

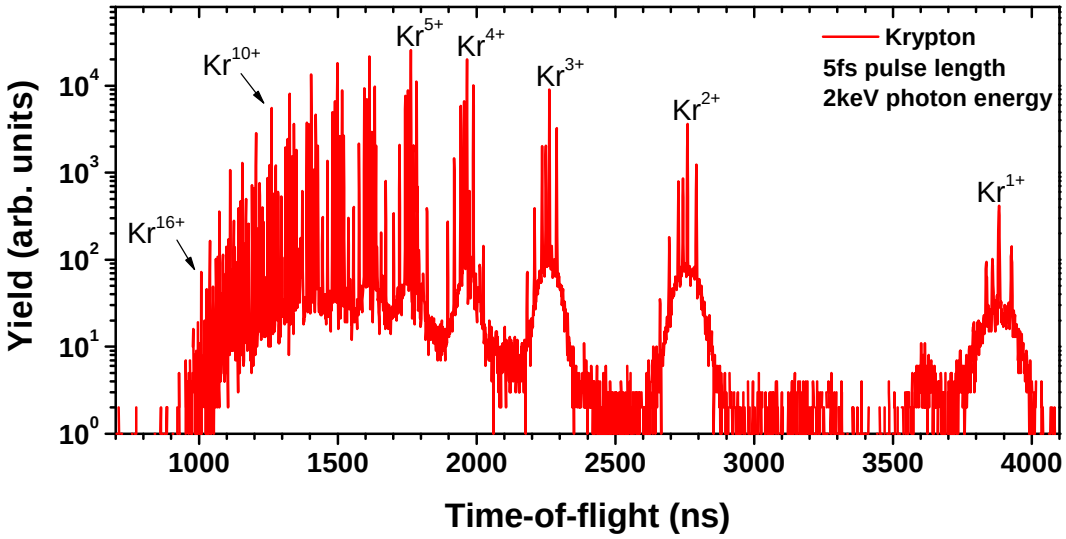

Figure 4.1: ToF-spectrum of krypton with 5 fs FEL pulses, 0.4 mJ pulse energy, at a photon energy of 2000 eV.

intensity. Using equation 2.14, the power dependence n, and, thus, the number of absorbed photons can be determined by using the following expression for the pulse energy E dependent yield Y:

$$Y = CE^n \tag{4.1}$$

where C is a fit constant.

In figure 4.2(a), the ion yield as a function of FEL pulse energy is shown for seven Kr charges states between Kr^{6+} and Kr^{16+} in a double logarithmic plot. In addition, the lines given by equation (4.1) for $n = 1, 2, 3, 4, 5$ are shown. From the comparison of experimental data and the calculated curves, it can be seen that the lowest depicted charge state, Kr^{6+}, is in good agreement with $n = 1$ and is thus produced mainly by one photon absorption. This is also the case for the lower charge states of Kr that are not shown in the figure. For higher charge states, the slope n increases and four photons are absorbed to reach Kr^{14+}.

In order to understand the charge-state distribution, the sequential Auger processes (cascades) that happen during de-excitation of the (2s)- or (2p)-vacancy have to be considered. For the case of single photon absorption, this is shown in figure 4.2(b). The core-holes created in Kr at the (2s) and (2p) levels decay mostly into (3d) vacancies and these, in turn, decay to the valence levels. The measured relative ion yields reflect the branching ratios of different pathways ending up in the

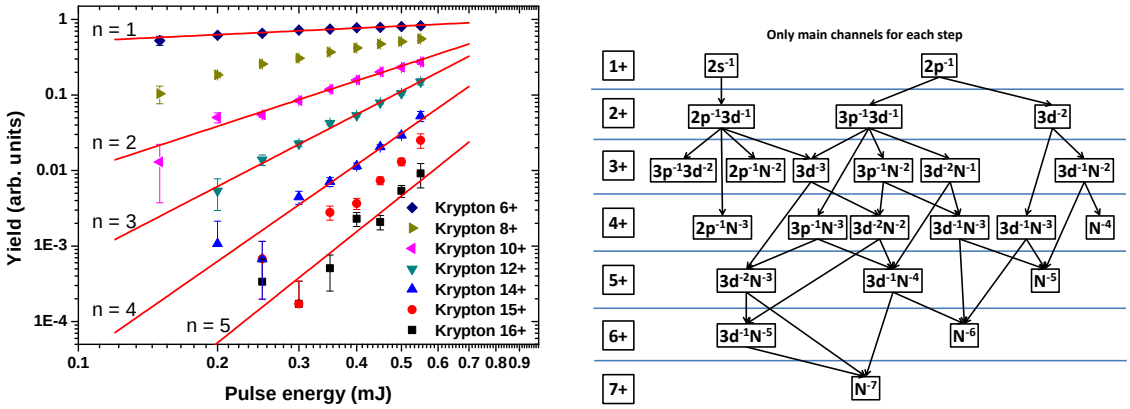

(a) Krypton ion yield versus pulse energy

(b) Krypton Auger cascade schematics

Figure 4.2: (a) Krypton ion yield versus FEL pulse energy to identify the number of photons n absorbed to create a certain charge state. The values for n are given next to the power dependence curves (representations of equation 4.1; solid lines). (b) Scheme of possible Auger decay cascades after (2s) or (2p) photoionization of Kr. For reduced complexity of the schematics only the main decay channels are shown.

respective final state upon single photon absorption [137].

In the case of FEL X-ray pulses, several photons might be absorbed within the (nominal) pulse length of 5 fs. Then, the Auger cascade is very likely not completed, i.e. the atom is not completely de-excited, at the time when a second photon is absorbed. Considering the Auger lifetimes shown in table 2.1 section 2.2.2, it can be estimated how far the cascade, triggered by the first photoabsorption, can proceed until the second photon is absorbed. The average time between the absorption of two photons can be estimated by the pulse length of 5 fs and the number of photons absorbed. For the highest charge states in krypton, this is up to 5 photons in 5 fs resulting in a photon absorbed about every 1 femtosecond. According to the Auger lifetimes and the schematic of a possible cascade, this shows that most likely only the first fast LLM- and LMM-Auger decays in table 4.2 will happen before the absorption of the second or even third photon occurs. The additionally absorbed photons do not stop the cascades started after the first core-vacancy, but rather induce new ones that decay in parallel, resulting in very complex electron dynamics. For more detailed discussions on multi-photon ionization of rare gases see reference [121].

Auger decay	Transition	Lifetime
LLM	Kr^{+} $(2s^{-1}) \rightarrow Kr^{2+}(2p^{-1}3d^{-1})$	160 as
LMM	Kr^{2+} $(2p^{-1}3d^{-1}) \rightarrow Kr^{3+}(3d^{-3})$	560 as
MMN	Kr^{3+} $(3d^{-3}) \rightarrow Kr^{4+}(3d^{-2}\ 4s^{-1}\ 4p^{-1}\ )$	7 fs
MNN	Kr^{4+} $(3d^{-2}\ 4s^{-1}\ 4p^{-1}\ ) \rightarrow Kr^{5+}(3d^{-1}\ 4s^{-2}\ 4p^{-2}\ )$	18 fs
MNN	Kr^{5+} $(3d^{-1}\ 4s^{-2}\ 4p^{-2}\ ) \rightarrow Kr^{6+}(4s^{-2}\ 4p^{-4}\ )$	155 fs

Table 4.2: Auger lifetimes in a possible pathway of a cascade after Kr (2s) ionization.

4.2 Methylselenol Fragmentation Dynamics after Inner-Shell Photoionization

Methylselenol (CH_3SeH) represents one of the simplest organic molecules containing selenium compounds. It consists of only two heavy constituents, carbon and selenium, which give the molecule a geometrical reference axis, and four additional hydrogen atoms, three at the carbon and one at the selenium site, as shown in figure 4.3.

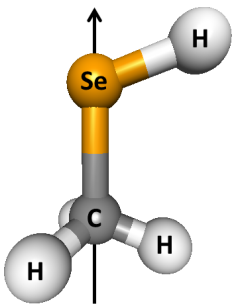

Figure 4.3: Illustration of the equilibrium geometry of methylselenol.

4.2.1 Fragmentation Channels of Methylselenol

When methylselenol, is photo-ionized, it can undergo complete fragmentation into several multiply charged fragments in the following way:

$$CH_3SeH + n{\cdot}\hbar\omega \xrightarrow{\text{photoionization}} [CH_3SeH]^{a+} \xrightarrow{\text{dissociation}} Se^{b+} + C^{c+} + 4\,H^{d+}$$

where a, b, c and d are integer numbers starting from 0 and $a = b + c + d$. The molecule thus can dissociate into a mix of charged and neutral atomic fragments or into larger molecular ions such as, for example, $[SeH]^+ + [CH_3]^+$.

With the experimental setup used in this work, only the ionic fragments can be detected. However, as previous investigations have shown, photoionization of methyl compounds at one of the deep inner-shell edges of a heavy atom constituent generally leads to a complete fragmentation of the molecules into atomic ions [73]. Thus, the contribution of neutral fragments is expected to be small. The ions are detected using the 3D momentum ion spectrometer as described in section 3.3.3.

Figure 4.4 shows the time-of-flight spectra of ions produced in the interaction of intense LCLS pulses with methylselenol molecules at photon energies of 2000 eV and 1700 eV. For the same (nominal) pulse duration of 80 fs (figure 4.4 traces (a) and (b)), there are only very subtle differences in the ion yields of the molecule after ionization at these two photon energies, which are both sufficient to produce (2s) and (2p) core-holes in selenium. Although the photoionization cross sections are different – 0.6 Mbarn at 1.7 keV and 0.4 Mbarn at 2.0 keV – the yields of the higher charge states of Se relative to Se^+ are comparable. A reason for this could be that at 2 keV, secondary multiple ionization processes, such as shake-off and shake-up, become more likely because of the higher excess energy, compensating somewhat lower photoabsorption cross section. Some of the small differences in the spectra can also be caused by changes in other machine parameters at the two different wavelengths and pulse durations that cannot be monitored and compensated by renormalization.

From the time-of-flight spectra, ionic fragments of Se^{1+} to Se^{9+} and C^{1+} to C^{3+}, created from the target molecule, are identified. It has to be noted that the flight times of selenium Se^{5+}, Se^{6+}, and Se^{7+} have significant overlap with O^{1+} and C^{1+}, which makes it challenging if not impossible to distinguish these fragments by simple ToF spectroscopy. In addition to the atomic fragments, there is a small signal at flight times of the singly charged parent ion as well as signatures of $CH_n{}^+$ fragments (with $1 < n < 3$), which have a count rate that is about 10 times lower than that of Se^{1+}. The spectrum also shows O^{1+} and O^{2+} ions from the residual gas in the main vacuum chamber as well as from impurities in the bubbler and the injection systems.

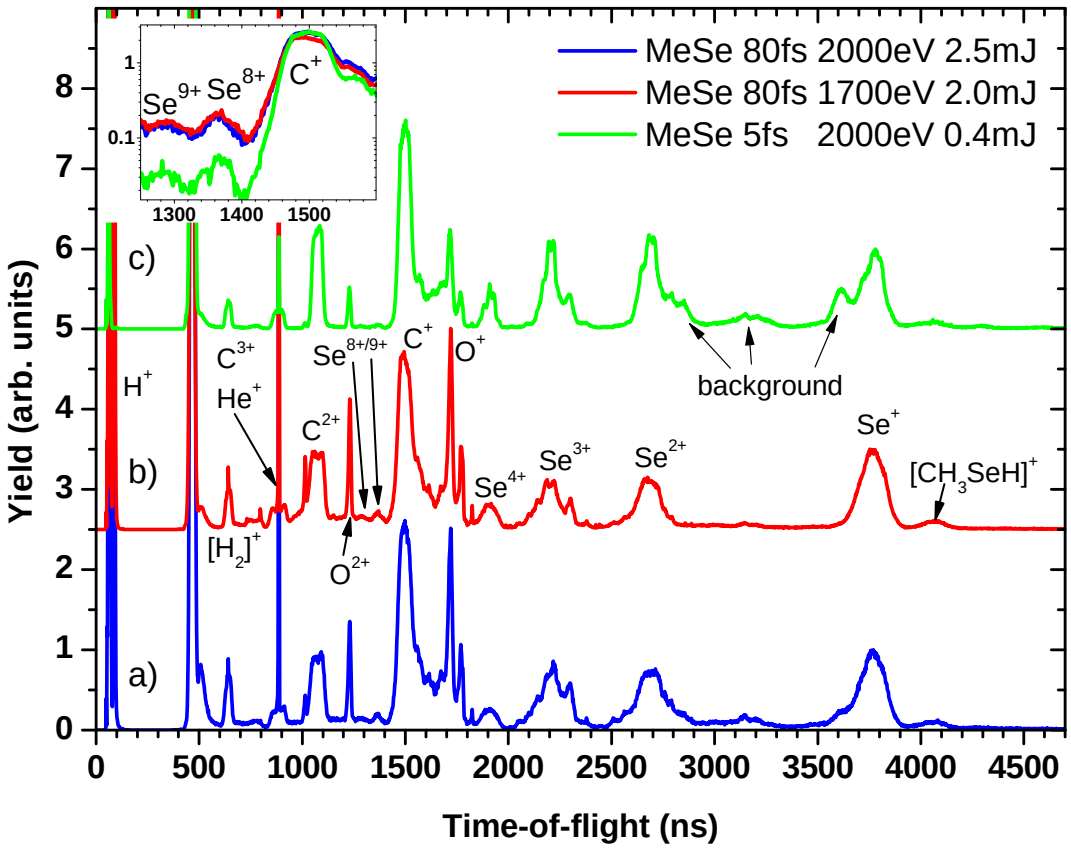

Figure 4.4: Ion time-of-flight spectra resulting from methylselenol fragmentation for different photon energies and pulse durations: (a; blue) 2 keV, 80 fs, and 2.5 mJ; (b; red) 1.7 keV, 80 fs, and 2 mJ; (c; green) 2 keV, 5 fs, and 0.4 mJ. All three curves are normalized on the Se^+ peak. The inset in the upper left corner shows the region of higher Se charge states on a logarithmic scale. The changes in the background signal (indicated by the arrows) are due to the lower target density used for the measurement with 5 fs pulses. Note, that curves b) and c) have an offset in yield for better visibility that is not present in the zoomed in inset.

Figure 4.4 (c) shows the time-of-flight spectrum of the ions produced by ultra-short 5 fs LCLS pulses at 2000 eV photon energy. Although the spectrum is overall similar to the results obtained with longer pulses, a pronounced difference can be seen in the highest charge states of Se (shown in the inset of figure 4.4). The yields of Se^{8+} and Se^{9+} are considerably suppressed for the ultra-short pulses, which is most likely the consequence of the lower pulse energy[10]. For the conditions of this experiment, effects of frustrated X-ray absorption for short pulses, discussed in reference [22, 25], are not expected to play a significant role, given the very short Auger lifetimes of the Se L-shell vacancies of less than 1 fs.

Another apparent difference is visible in the relative peak heights of the Se^{2+}, Se^{3+}, and Se^{4+} fragments as compared to Se^{1+}. The Se^{2+} to Se^{4+} peaks appear higher for the short pulse, although the integrated yield for each of these channels is roughly the same for both pulse durations. The peaks for the 5 fs pulse are narrower, reflecting the lower average kinetic energy of the fragments which are most likely due to the overall lower level of ionization (see section 4.2.4 for a detailed discussion of fragment kinetic energies in the 5 fs case).

Non-coincident time-of-flight spectra such as those shown in figure 4.4 only reveal information on the yield of individual ionic fragments. However, as described in section 3.3.3, there are correlations between ions originating from the same molecule, that remain unresolved in simple ToF spectra, but can be exploited by coincidence spectroscopy in order to identify the final state of the whole molecular system, and to disentangle different fragmentation channels.

A typical photoion-photoion coincidence (PIPICO) spectrum for methylselenol irradiated with 5 fs X-ray pulses of 2 keV photons and an average power of 400 μJ, corresponding[11] to a fluence of $\sim 15\,\mu J/\mu m^2$, or an intensity of $3 \cdot 10^{17}\,W/cm^2$, is shown in figure 4.5. There are a total of 27 different fragmentation channels that can be identified by looking only at the coincidences between the two heavy ions, Se^{n+} and C^{m+}. It should be noted that in the fragmentation of methylselenol, most of the momentum is carried by the two heavy fragments selenium and carbon, which makes it possible to identify correlated coincidence lines in the PIPICO spectrum considering only these two constituents. For channels with high yield and longer

[10] This represents the highest pulse energy 0.4 ± 0.2 mJ that could be achieved using the "short bunch" mode that produces sub 10 fs pulses.

[11] Assuming a pulse length of 5 fs and a focus size of $3 \times 3\,\mu$m, where the latter is based on simulation parameters used in reference [121] to model the charge-state distribution in krypton.

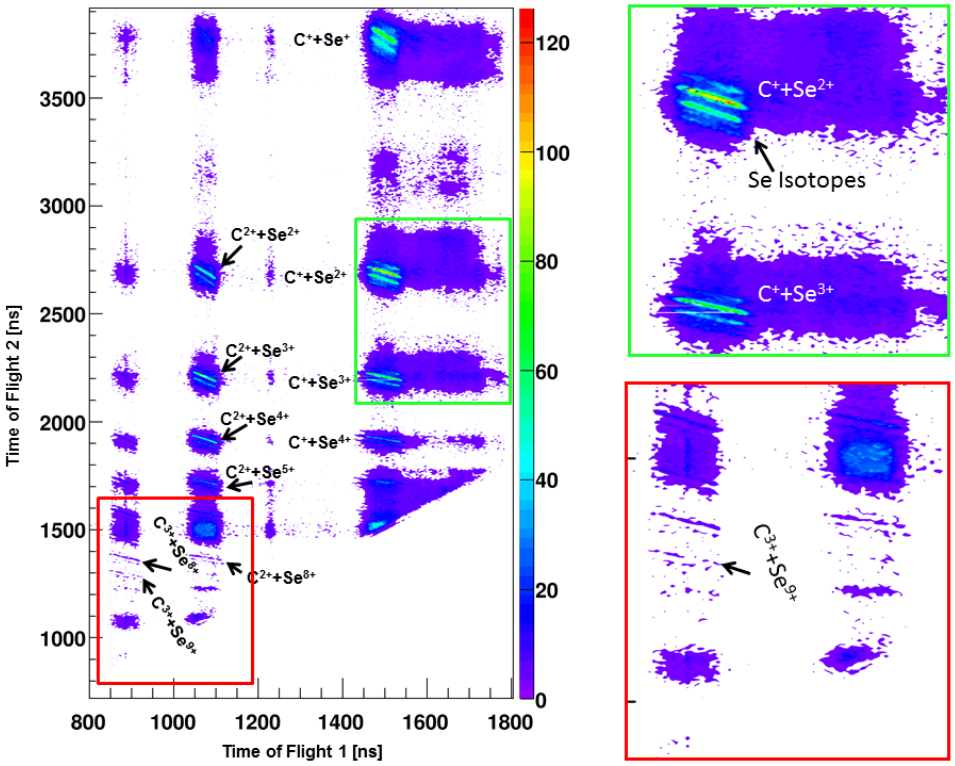

Figure 4.5: PIPICO spectrum of methylselenol fragmentation after interaction with 5 fs FEL pulses of 2 keV photon energy and a pulse energy of 0.4 mJ. The two insets are zooms into low (green) and high charge channels (red). For strong channels, the five main isotopes of selenium can be identified in the spectrum as distinct parallel lines.

flight times, the five main isotopes of selenium can be distinguished as parallel lines in the PIPICO spectrum. These five lines can also be identified in the sum of the momenta of coincident selenium and carbon ions. Examples of momenta sums for a few channels are shown in figure C.1 of the appendix. By selecting only ion pairs whose momentum sum lies in the main peak close to zero, the ambiguity of different isotopes can be removed from the coincidence spectra. Moreover, this also eliminates false coincidences with ions from the background or of ions originating from different molecules[12].

In the following sections the data are filtered according to the momentum conservation conditions described above in order to extract the yields and 3D momentum vectors of the ions originating from particular fragmentation channels.

[12]For methylselenol, this cut in the momentum sum of the two heavy ions was only done in the Z-component (calculated from the ToF). X- and Y- components remained untouched as lower momentum resolution along these directions makes distinguishing the isotopes very challenging.

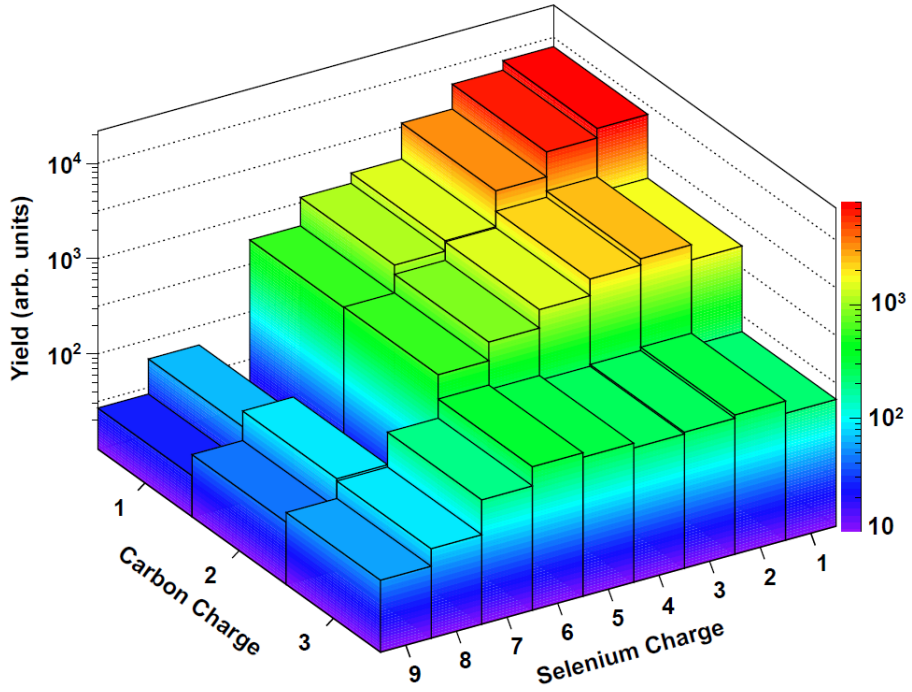

Figure 4.6: Yield of heavy-ion-fragment coincident channels from methylselenol as a function of charge state for a pulse energy of 0.4 mJ, 5 fs pulse length, and a photon energy of 2000 eV. Note that the $Se^{7+}C^{1+}$ and $Se^{7+}C^{2+}$ channels were omitted because of false coincidences due to Se^{1+} and C^{1+} having the same mass to charge ratio.

4.2.2 Ionization Yields

After identifying the fragmentation channels from the PIPICO spectrum, it is possible to extract the relative yields of the individual channels. These relative yields shown in figure 4.6 reflect the probability of the system ending up in a given charge state and, thus, provide first information on the processes triggered by inner-shell photoionization at the selenium site (L-shell).

When examining the yields of different charge-state combinations in figure 4.6, it can be seen that the channels with the lowest total charge have the highest abundance and that the abundance in most cases decreases with increasing charge states. In addition, channels that have higher charged carbon ions than selenium ions, i.e. $q_C > q_{Se}$, such as $Se^+ + C^{3+}$, have lower relative yields. This can be understood by considering that the ionization cross section of the selenium L-shell is much higher than for any carbon shell[13], which means that it is much more likely that photons

[13]Se cross section 406 kbarn at 2 keV; C cross section 6.02 kbarn at 2 keV (XCOM NIST)

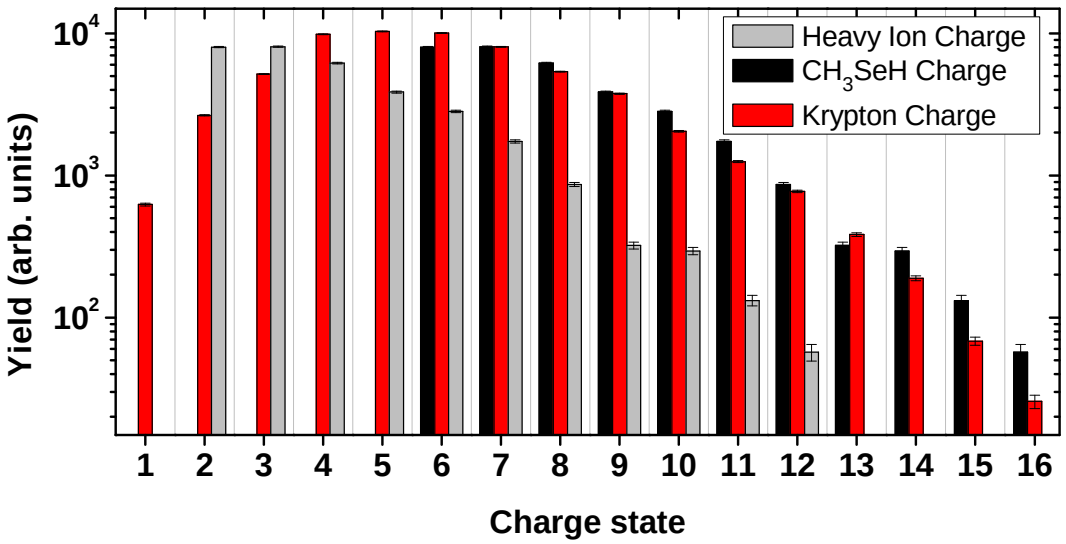

Figure 4.7: Total charge induced on the methylselenol molecule compared to the charge-state distribution observed in Kr under the same conditions. Heavy-ion charge represents the sum of Se and C charges measured in coincidence, whereas CH_3SeH charge denotes the total charge of the molecule assuming that four H^+ ions were produced. The Kr and methylselenol data were taken at a pulse energy around 0.4 mJ, 5 fs pulse length, and 2 keV photon energy.

are absorbed by the selenium atom. Considering all coincident ion pairs, the average charge state for carbon ions is $\bar{q}_{\mathrm{C}} = 1.41$, and for selenium ions is $\bar{q}_{\mathrm{Se}} = 2.55$.

In order to deduce the total charge induced in the molecular system, the sum of selenium and carbon charge ($q_{\mathrm{Se}} + q_{\mathrm{C}}$) is determined for each channel, and the yields of all channels with the same $q_{\mathrm{Se}} + q_{\mathrm{C}}$ are added together. This reduces the 27 carbon-selenium coincidence channels to 11 groups, which are in the following referred to as heavy-ion charge states. Their abundances are shown in figure 4.7 (gray bars).

As coincident detection of all six ionic fragments could not be achieved, assumptions have to be made in order to conclude on the final charge of the molecule. Although some proton fragments were detected in coincidence, they are not considered for the determination of the total charge state of the molecule, because of the intrinsically low multi-ion detection efficiency and the rather low repetition rate of 120Hz at the LCLS made it impossible to gather enough statistics for coincidences of more than three particles in the beam time given. Assuming that all the four hydrogen fragments are charged by 1+ each, i.e. adding a charge of four to every heavy-ion charge state, results in a distribution that represents an estimate of the

total molecular charge (solid black bars). At least for higher heavy-ion charge states, this estimate seems valid [138], while there may be considerable deviations for low charge states.

Comparing the total molecular charge created from methylselenol with the charge of atomic krypton (deduced from figure 4.1) measured under the same experimental conditions, good agreement between the atomic and the molecular case is found. Both distributions show charge states of up to 16+ and the general shapes of the distributions are very similar for $q > 6+$.

The average charge state induced in Kr, is $\bar{q}_{\mathrm{Kr}} = 5.92$, whereas for methylselenol, the average heavy-ion charge is $\bar{q}_{\mathrm{Se+C}} = 3.97$ and the average total molecular charge, assuming creation of four H+ fragments, is $\bar{q}_{\mathrm{MeSeH}} = 7.97$. The discrepancy between Kr and the molecule can be explained by the fact that while the assumption of all four hydrogen atoms being charged is certainly close to reality for high charge states, where carbon and selenium are both missing two or more electrons (as was observed for the protons of SiH_4 after Si ($1s \rightarrow \sigma^*$) excitation [138]), it is much less accurate for the low charge states, where it is more likely that some of the hydrogen atoms dissociate as neutral fragments.

Another difference is the increased yield of total molecular charge states above 14+ as compared to Kr. This can be accredited to the fact that methylselenol has more electrons in total than Kr and, even more important, a higher density of states, as well as an increased total number of electrons in the valence orbitals. This results, e.g., in a higher probability of higher order ionization processes such as shake-off [136][14] in the molecule as compared to the single atom. This behavior is most prominent in channels where the number of absorbed photons is higher, as will be discussed in the next section.

To summarize the discussion of figure 4.7, it can be stated that the total overall charge created in atomic krypton and the selenium containing molecule, which both have similar absorption cross sections at a photon energy of 2 keV, is in good agreement, whereas the maximum charge state in selenium (Se^{9+}) is significantly lower that in krypton (Kr^{16+}). This clearly indicates charge redistribution within the molecule that transfers the charge initially localized at the Se site towards the neighboring carbon and hydrogen atoms. In order to further understand the processes

[14] Shake-off probability in Kr after first (2s) or (2p) ionization is around 12% for (4p); 2% for (4s); 3% for (3d); and less for other shells, according to reference [136].

underlying these charge redistribution effects, more information can be extracted from the data as discussed in the following sections.

4.2.3 Multi-Photon Absorption

To gain insight into the dynamics of multi-photon absorption in a molecular system, the FEL pulse-energy dependence of the system's charge states, as introduced for krypton, is investigated.

In figure 4.8, the yields of individual coincident Se and C ion channels are shown as a function of FEL pulse energy in a double-logarithmic representation. Figure 4.8(a) provides an overview of channels showing different slopes ranging from $n = 1$ to $n = 4$ including "mixed" channels indicated by non-integer slopes, e.g. $n = 1.5$. The pulse energy changes between 0.1 mJ and 0.6 mJ, corresponding[15] to an FEL intensity of $0.9 \cdot 10^{17}\,\mathrm{W/cm^2}$ to $3.5 \cdot 10^{17}\,\mathrm{W/cm^2}$. The errors in the ion yield are statistical errors, whereas the error in the shot-to-shot pulse energy determination by the GED is unknown but assumed to be small and to only result in an offset rather than to change the slope.

The channels with a slope of $n = 1$ are shown in figure 4.8(b). Those include the methylselenol parent ion $[CH_3SeH]^+$ whose intensity-dependent yield is in good agreement with the function, verifying the linearity of the GED in the pulse energy range discussed here. Other channels that are produced by single-photon absorption, are $Se^{1+}C^{1+}$ and $Se^{2+}C^{1+}$, which represent the heavy-ion charge states with the lowest induced charge in the methylselenol molecule.

For channels with higher charge, such as $Se^{3+}C^{1+}$ to $Se^{4+}C^{2+}$ shown in figure 4.8(c) and 4.8(d), the overall slope can be approximated best assuming $n = 1.5$. In fact, the slope is dependent on the pulse energy, as can be seen from the two solid gray curves in figure 4.8(c) for the $Se^{3+}C^{1+}$ channel. Below a pulse energy of ~ 0.33 mJ, the experimental data points of this channel follow a function with slope $n = 1$ and above this pulse energy, there is an increase in the slope to $n = 2$. This is consistently observed for all channels with heavy-ion charge $q_{\mathrm{SeC}} \leq 4$ with an indication that the change in slope occurs at different pulse energies for individual channels. The explanation for this finding is that there are two different competing pathways leading to the same final state. One route involves the absorption of just

[15] Assuming a pulse length of 5 fs and a focus size of $3 \times 3\,\mu$m, where the latter is based on simulation parameters used in reference [121] to model the charge-state distribution in krypton.

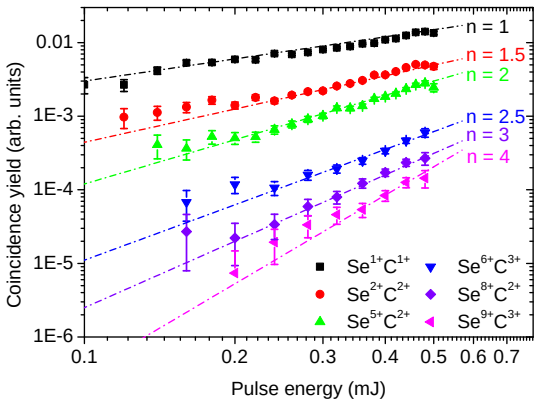

(a) Overview from $n = 1$ to $n = 4$

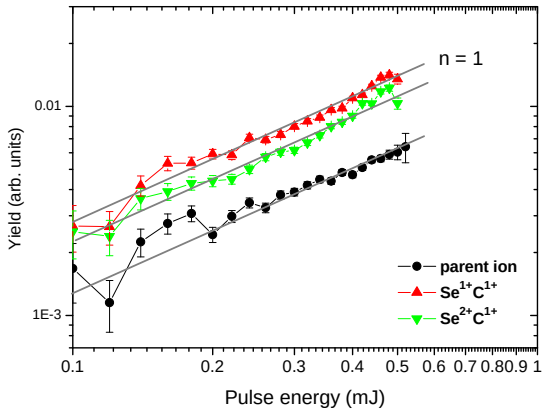

(b) n = 1

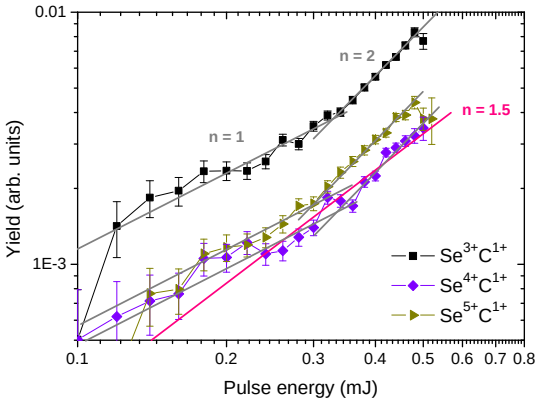

(c) n = 1.5

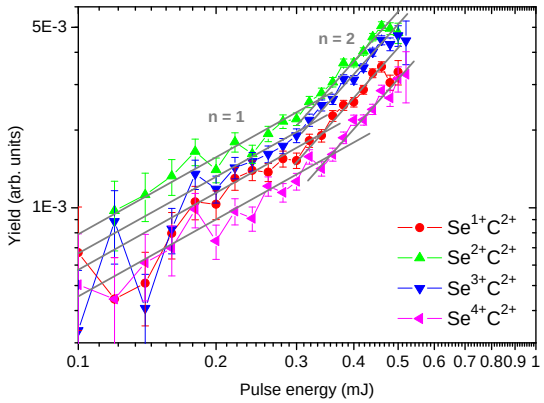

(d) n = 1.5

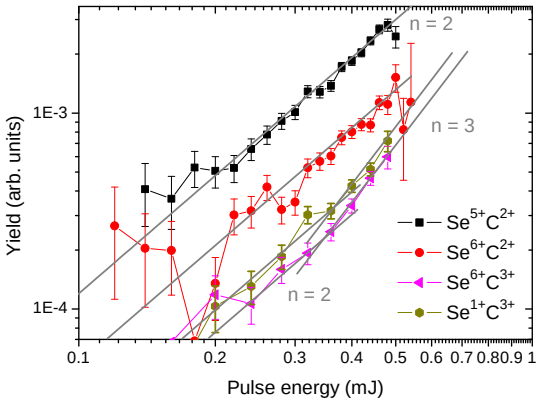

(e) n = 2, n = 2.5

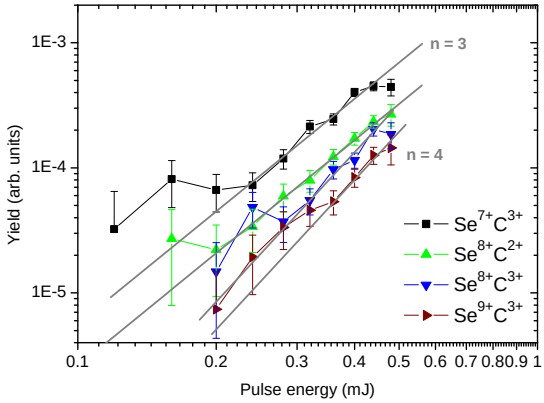

(f) n = 3, n =4

Figure 4.8: Comparison of slopes n for individual coincident Se and C ion channels represented in a double-logarithmic plot of channel yield versus FEL pulse energy. Dashed-dotted color lines in the overview spectrum (a) and solid (gray) lines (b - f) are representations of equation 4.1 for different numbers of absorbed photons n as indicated. Solid gray lines in (c, d) show functions with slopes $n = 1$ and $n = 2$ for two regions of pulse energies for the $Se^{3+}C^{1+}$ to $Se^{4+}C^{2+}$ channels.

one photon, whereas in the other the absorption of a second photon occurs during the Auger cascade triggered by the first one. The two-photon pathway tends to dominate at higher pulse energies E due to its E^2 dependence as compared to the "single photon path" increasing linearly with the pulse energy E.

Channels with larger heavy-ion charges $q_{\mathrm{SeC}} > 6$ and, surprisingly also some with $q_{\mathrm{SeC}} < 6$ but very asymmetric charge distribution involving C^{3+} ions, show slopes of $n = 2$ and higher as can be seen from figure 4.8(e). Here, an increase in the slope, changing form n to $n + 1$, can be observed for the exemplary $Se^{6+}C^{3+}$ and $Se^{1+}C^{3+}$ channels, as indicated by the solid gray lines. For these channels, the statistics for pulse energies below 0.2 mJ become very small, producing large error bars and reducing the signal-to-background ratio. The highest charge states in the molecule (shown in figure 4.8(f)), i.e. $Se^{7+}C^{3+}$ and $Se^{8+}C^{2+}$ show slopes of $n = 3$ or even $n = 4$ for $Se^{8+}C^{3+}$ and $Se^{9+}C^{3+}$. This corresponds to the absorption of up to 4 photons in the course of a pulse of 5 fs duration.

Comparing the slopes discussed above with the measurements for krypton shown in figure 4.2(a), several tendencies are observed. First, it can be noted that the charge states of Kr produced with less than two photons, i.e. up to Kr^{9+}, match with the number of photons absorbed to produce a similar total charge in the molecule, which are the channels with charges lower than $Se^{5+}C^{2+}$ or $Se^{3+}C^{3+}$. However, the krypton slopes show no significant kinks like the ones observed in methylselenol. An explanation of this different behavior could be the afore discussed ambiguity in the total charge state of the molecule due to the fact that multiple coincidences with all hydrogen ions were not considered. For higher charge states, the slopes in Kr increase very rapidly from a slope of $n = 2$ for Kr^{10+} to $n = 5$ for Kr^{16+}, whereas for methylselenol the highest slope observed within the statistical error bars is $n = 4$, for $Se^{9+}C^{3+}$ (corresponding to a total molecular charge state of 16+).

The latter is another indication that a given number of photons can produce higher total charge states in the molecule than in the atom, due to the increased number of valence electrons in the molecule which enhance the contributions of shake-off processes or may allow for ejection of additional electrons during an Auger cascade for example by double Auger decay.

4.2.4 Fragmentation Dynamics: Kinetic Energies and Bond Lengths

The methylselenol molecule consists of three different elements, namely selenium, carbon and hydrogen, with atomic masses of 79, 12 and 1 amu (atomic mass units), respectively. The different masses result in differences in the speed of nuclear motion in the dissociation of the molecule, thus "probing" the dynamics of the photoionization and subsequent Auger decays on different time scales.

4.2.4.1 Selenium and Carbon Energies

Selenium is the heaviest constituent in methylselenol. For the photon energies considered here it also has the highest photoabsorption cross section. As such, it is both, the "static" center in terms of movement compared to the other ions, and the "source" of charge that is induced in the molecular system by photoionization of the Se L-shell. As one of the consequences of its large mass, selenium is the least affected by momentum transfer from hydrogen ions in the dissociation of the molecule.

The *kinetic energy distributions* (KEDs) of the selenium ions for different heavy-ion charge states are shown in figure 4.9(a). The maximum of the KED is shifting towards higher energies for larger q_{SeC} and, at the same time, the width of the KED increases. The measured KEDs are compared to the kinetic energies obtained from the Coulomb explosion simulation presented in section 2.3.2, which are indicated by vertical lines of the same color in figure 4.9(a) with the corresponding channel indicated next to them. Note that for all channels in the simulation, unless specified otherwise, all four hydrogen atoms are assumed to have a charge of 1+.

The measured KEDs are in reasonable agreement with the Coulomb explosion simulation, only for the $Se^{1+}C^{1+}$ and the $Se^{2+}C^{1+}$ channels, assuming equilibrium geometry and equilibrium bond lengths of the methylselenol molecule. For all higher final charge states, however, the simulation tends to overshoot the measured energies, which becomes more and more severe as the charge state of the molecule increases. This is a clear indication for considerable motion of the nuclei taking place on the time scale of the multiple-ionization process itself, i.e. the bond lengths stretch while the molecular charge is still increasing via Auger decay (cascade) and/or absorption of additional photons.

For the carbon ions, which have a smaller mass by a factor of ~ 6.6 as compared

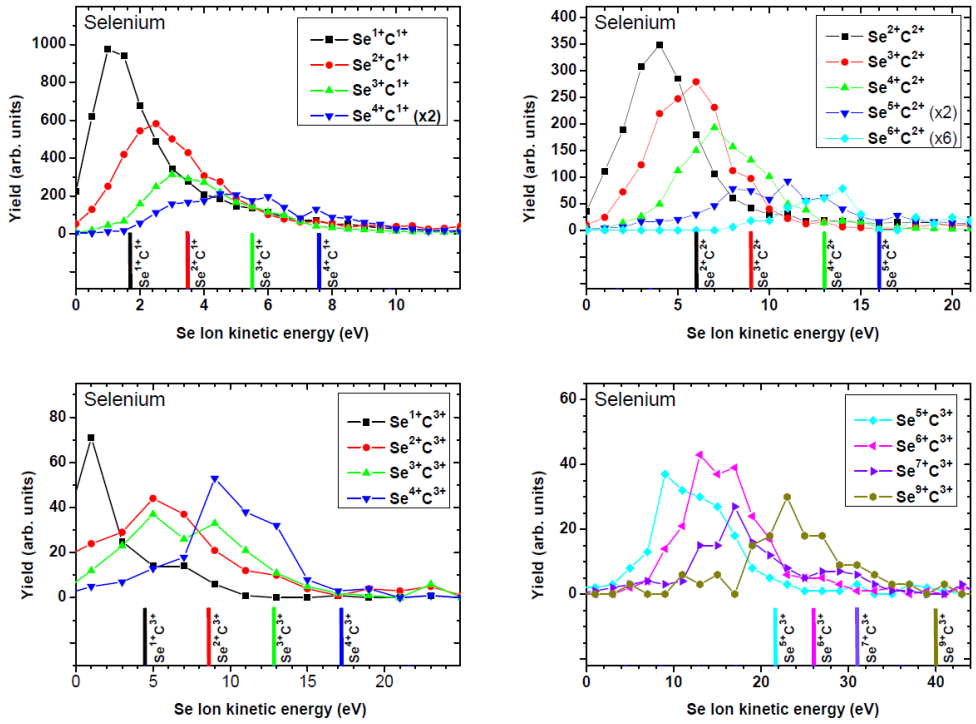

(a) Selenium ion kinetic energy distributions.

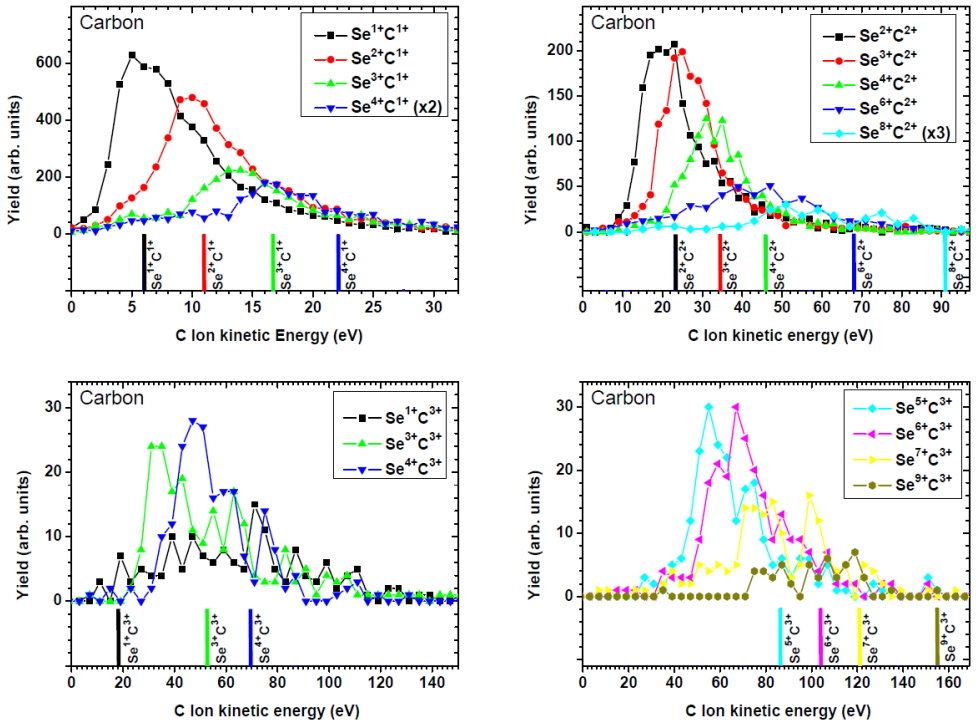

(b) Carbon ion kinetic energy distributions.

Figure 4.9: Overview of selenium and carbon ion kinetic energy distributions for different heavy-ion charge states of methylselenol (Se-C ion coincidences). Simulated kinetic energies for the same charge states are indicted at the bottom by vertical lines of the same color.

to selenium, the discrepancy between measured KEDs and simulated energies is even more severe, as shown in figure 4.9(b). Whereas the energy distributions for $Se^{1+}C^{1+}$, $Se^{2+}C^{1+}$, and $Se^{2+}C^{2+}$ are in good agreement with the simulation the difference between the model calculation and measurement rises rapidly with increasing charge states. For the $Se^{4+}C^{1+}$ channel for example the simulated energy for carbon ions of 22 eV is already 20% larger than the maximum of the measured distribution at 16 eV. Higher charged channels have distributions of carbon ion kinetic energies that are even further away from the simulated values. In most of these cases, especially for channels with carbon 3+, the simulated energy is at the end of the high-energy tail of the measured energy distribution.

According to equation 2.20, for a diatomic molecule that undergoes ionic fragmentation, the total potential energy at t_0, and thus, the final total kinetic energy of the system in eV can be written as

$$E_{\mathrm{kin,final}} = E_{pot,t_0}[\mathrm{eV}] = 14.49 \times \frac{q_1 q_2}{R[\mathrm{\AA}]} \tag{4.2}$$

where q_i are the charges of the two ions and R is the internuclear distance in Ångström. Although, in the case of methylselenol this is not completely true because of the four additional hydrogen atoms present, their relatively small masses and, thus, small momenta, allow to approximate the molecule as a diatomic Se−C system.

In figure 4.10, the sum of the kinetic energies of coincident carbon and selenium ions is shown as a function of their charge state product, i.e. $(q_{\mathrm{Se}} \cdot q_{\mathrm{C}})$. The symbols represent the maximum of the *sum kinetic energy distribution* (sKED), whereas the vertical bars do not depict error bars but the width of each distribution at the half maximum height, which is for most channels a non-symmetrical full width at half maximum (FWHM). The final kinetic energies as a function of the charge-state product, calculated from equation 4.2 for two internuclear distances $R_0 = 1.97\,\mathrm{\AA}$ and $R = 3\,\mathrm{\AA}$, are also shown in figure 4.10 as dashed and solid lines.

To further test whether the assumption of negligible influence of the protons is correct, sum kinetic energies for a few exemplary channels simulated with the Coulomb explosion model for the actual molecule including the protons are indicated by the magenta circles. The agreement between the simulation values and the simple two atom curve for $R_0 = 1.97\,\mathrm{\AA}$ (equilibrium distance) is good, and shows only minor

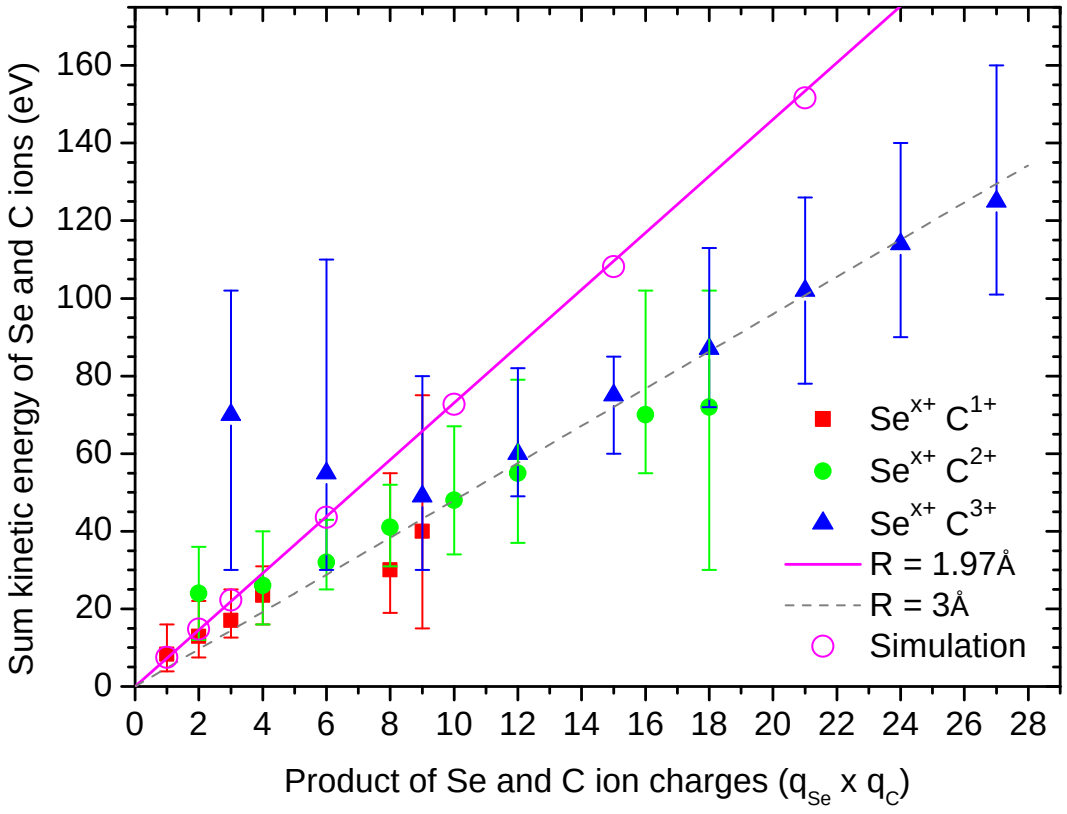

Figure 4.10: Measured (full symbols) and calculated (lines) sum kinetic energy of Se and C ions as a function of the product of their charge states. Open circles represent the results of the CE simulation assuming that all four H atoms are charged. The solid line depicts the total energy of Se and C ions for CE at the equilibrium R, whereas the dashed line corresponds to $R = 3$ Å. Note, that for the experimental data the symbols represent the maximum of the sum energy distribution, while vertical bars indicate the non-symmetrical full width at half maximum, and not the error bars.

differences for large charge-state products (> 15).

Comparing the calculated energies with the measured sKEDs for methylselenol, it can be seen that only the channels with the lowest charges, namely $Se^{1+}C^{1+}$, $Se^{2+}C^{1+}$, $Se^{3+}C^{1+}$, $Se^{4+}C^{1+}$, and $Se^{2+}C^{2+}$ show kinetic energies that are in good agreement with the $R_0 = 1.97\,\text{Å}$ curve. For all other channels with higher charge-state products, the measured sKED is significantly lower than expected for the assumption of instantaneous charge-up of the molecular system, as indicated by the magenta solid line. It is found that the sKED maxima for high charge states can be better represented by equation 4.2 for an internuclear distances of $R = 3\,\text{Å}$, represented by the gray dashed line in figure 4.10.

The reason for this is, as already mentioned above, that the charge of the system further increases via Auger decay and photon absorption as the molecule already begins to fragment, or, in this picture, as R starts to increase. This produces lower final kinetic energies of the fragments compared to the case where the final charge state is already reached at the smaller equilibrium distance R_0. In this context, the gray dashed line in figure 4.10 for a distance of $R = 3\,\text{Å}$ provides an estimate for the average molecular deformation during few-photon absorption and subsequent Auger decay. This means that the molecule is stretched by $\sim 50\%$ of the equilibrium internuclear distance within 5 fs to 20 fs, considering the pulse length and Auger decay lifetimes.

The channels where the final carbon charge is higher than the selenium one, $q_C > q_{Se}$, show a special behavior. In both $Se^{1+}C^{3+}$, $Se^{2+}C^{3+}$, and $Se^{1+}C^{2+}$, the distribution of ion kinetic energies is very broad and extends far beyond the simulated energy. This observation is very surprising since the assumption of instantaneous CE at R_0 normally provides the upper limit for the ion kinetic energies detected upon a breakup of a multiply ionized molecule. The most plausible explanation, going well along with the observed numbers of absorbed photons that is higher than for other channels with the same charge-state product, implies that the whole Se-C complex is initially charged higher than in its final state, resulting in CE at small R with high fragment energies, and, subsequently, sharing the charge with the neighboring protons. As mentioned, according to the measured intensity-dependent yields, the final states which fulfill $q_C > q_{Se}$ correspond to the absorption of 2 or even 3 photons (see figure 4.8). Although one of the photons might be absorbed by the carbon K-shell, two-photon absorption by the carbon atom is extremely unlikely due to the

low cross section. Therefore, the pathways to these final states most likely involve "interatomic" molecular Auger decay, "filling" Se inner-shell vacancies with valence electrons of the C and H atoms, which, as mentioned above, is more probable to happen at small internuclear distances [73]. Thus, the presence of these asymmetric channels along with their anomalously high CE energies most likely reflects ultrafast charge rearrangement involving inner-shell vacancies and occurring before any significant nuclear motion. Considering that two or even three photons are absorbed and that, according to the sKEDs of the channels under discussion would correspond to $q_{\mathrm{Se}} \cdot q_{\mathrm{C}} \sim 10$ to 16, one is lead to conclude that all four hydrogen atoms are ionized. The role of the four hydrogen atoms is addressed in detail in the next section.

4.2.4.2 Proton Kinetic Energies

As the charge generation (subsequent removal of electrons) in the molecule happens on about the same timescale as the FEL pulse duration, namely within a few up to a few tens of femtoseconds (see table 4.2), it is interesting to inspect an observable in the system that exhibits dynamics on a similar time scale. This is the case for the motion of the protons. Thus, by looking at the proton KEDs, which are, in first approximation, inversely proportional to the distance to their next neighbor ions the fast ionization dynamics can be investigated.

In general, the measured proton kinetic energy distributions, which are shown in figure 4.11, only show a weak dependence on the corresponding heavy-ion charge state. The relative increase in kinetic energy of the maxiumum of the KEDs for higher Se charge states is by no means as strong as for the carbon KEDs, where the kinetic energy increases for the $Se^{1+}C^{1+}$, $Se^{4+}C^{2+}$ and $Se^{9+}C^{3+}$ channels like 6 eV, 34 eV to $\sim$ 100 eV, respectively. This is an increase by a factor of 16.7 (for selenium this increase is by a factor of $\sim$ 19), whereas for protons, the kinetic energy increases for the same channels from 15 eV , 30 eV to $\sim$ 40 eV, which is only a factor of 2.7. This trend is in accordance with the simple Coulomb explosion model, where the increase in kinetic energy is $\sim$ 26.5 for carbon, $\sim$ 23.5 for selenium, and $\sim$ 4.0 for protons.

In contrast to the KEDs of the heavy ions, the simulated energies for the protons are in almost all cases even above the high-energy tail of the measured KEDs. This indicates that the protons are starting to fly away in an early stage of the ionization process. As protons have a mass that is $\sim$ 12 times smaller than the one of carbon

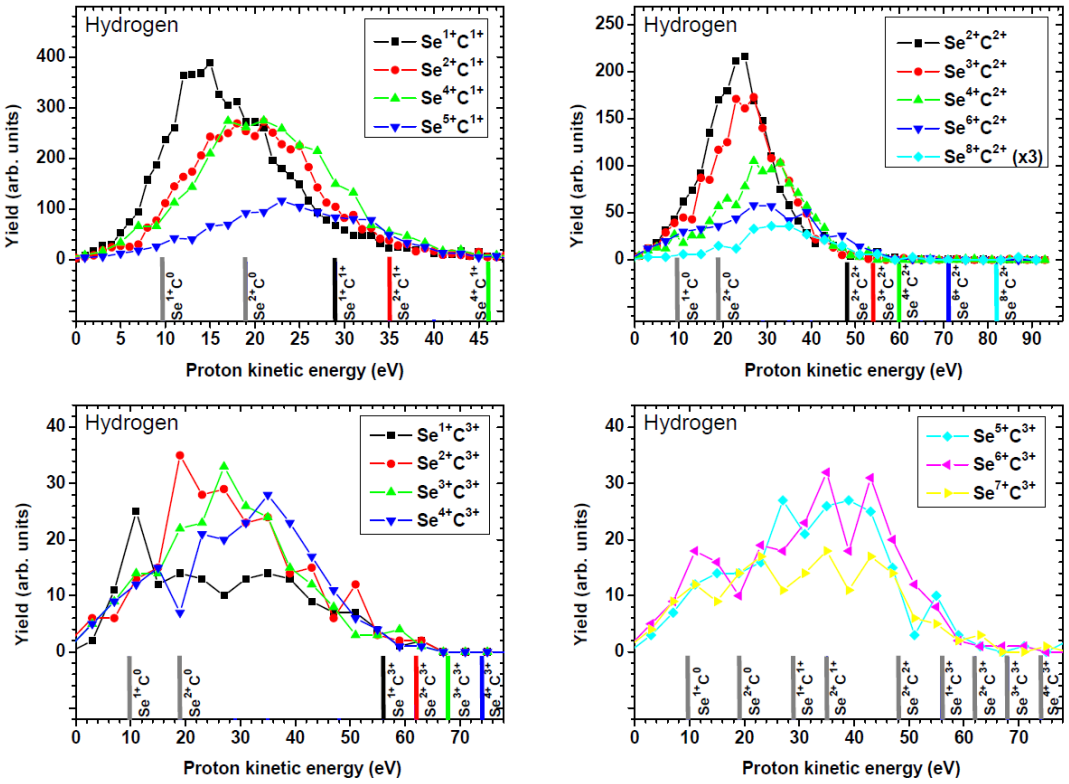

Figure 4.11: Kinetic energy distributions of hydrogen ions for different final states of the molecular system (Se-C ion coincidences). Simulations are indicated by the vertical lines of the same color at the bottom with input charge states next to them. Colors of the simulations correspond to the colors of the measured data points and other channels are denoted by gray lines. Note that the gray lines "$Se^{1+}C^{0}$" and "$Se^{2+}C^{0}$" represent simulations where only the selenium ion and the proton next to selenium was charged and the rest of the molecule remains neutral.

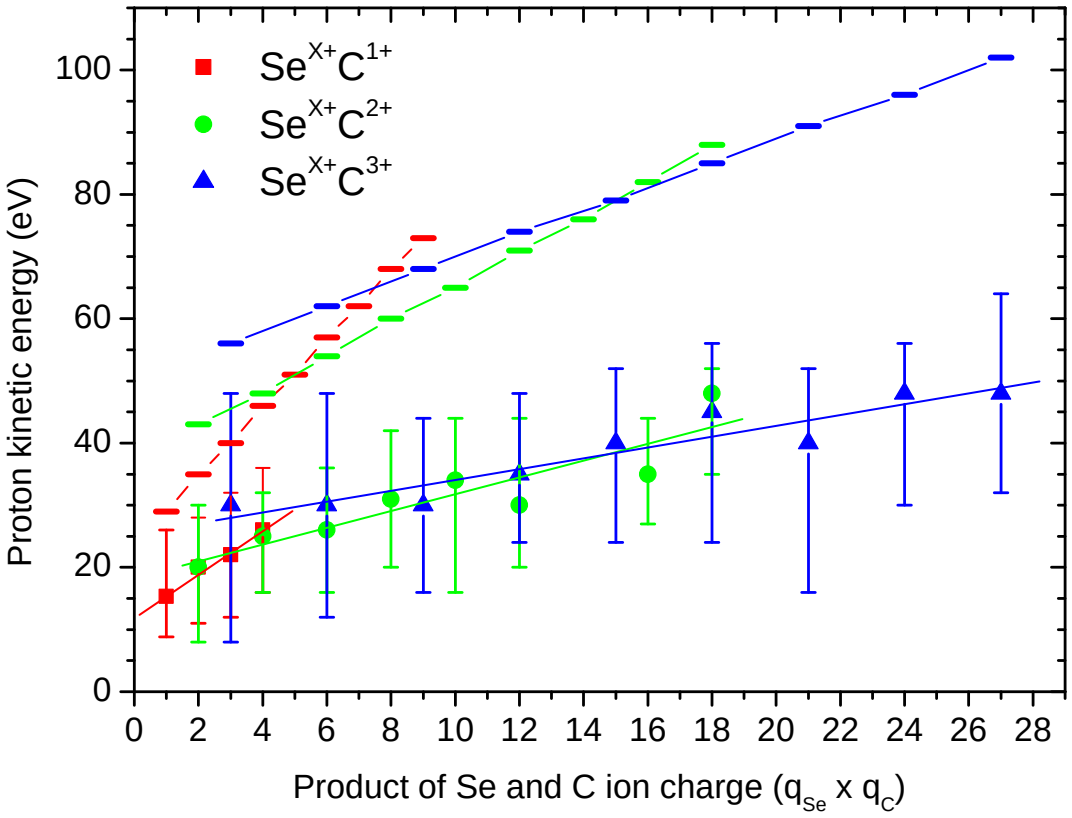

Figure 4.12: Overview of hydrogen ion kinetic energy distributions for different final states of the molecular system (Se-C ion coincidences). Horizontal thick lines indicate the simulated average energies of the four protons assuming equilibrium geometry of methylselenol and that all four protons are charged in addition to the two charges on the heavy ions indicated by the color and the charge-state product. Dots indicate the maximum of the measured proton KEDs and vertical bars indicate the (non-symmetrical) width of the distribution at half height. Thin colored lines are meant as a guide to the eye to emphasize the three different slopes of the dependency of proton KEDs on the charge-state product that is observed for the different carbon charges, in both simulation and measurement.

ions, their distance to the heavy-ion neighbors increases rapidly due to their repulsive Coulomb potential. For example, in one femtosecond, a proton with a kinetic energy of 27.2 eV (one atomic unit of energy, corresponding to the simulated kinetic energy of protons from the $Se^{1+}C^{1+}$ channel at R_0) travels a distance of 3.5Å, which is more than three times the C−H bond length of 1.09Å.

Figure 4.12 shows the measured proton kinetic energies for individual fragmentation channels (symbols indicate the maximum of the KED and the vertical bars the width at half maximum height). It is clear that the simulated energies (shown as thick horizontal lines of the same color) for the same final charge states in the molecule are significantly too high to match the experimental data. Nevertheless, both, experiment and simulation show a similar dependency on the total molecular charge (here represented by the product of the final Se and C charge) with a steeper increase at the beginning, up to $q_{Se} \cdot q_C = 6$, followed by a less steep incline.

This change in slope happens at about the same product charge state, where two-photon absorption becomes a possible pathway in the production of channels such as $Se^{5+}C^{1+}$, $Se^{3+}C^{2+}$, and $Se^{4+}C^{2+}$, which were characterized by non-integer slopes of $n = 1.5$ or a pulse-energy dependent transition for slope $n = 1$ to $n = 2$ (in section 4.2.3, figures 4.8(c) and 4.8(d)). This is an indication that the final proton energies are less influenced by the increased charge states due to multi-photon absorption, as the protons are already further away and feel less force from the Coulomb repulsion at the time when a second photon is absorbed and charges further increase due to (fast) Auger decay(s). The maximum energy measured for protons, i.e. the high-energy tail of the KED, is 65 eV for the $Se^{9+}C^{3+}$ channel (highest resolved charge state), whereas the simulated energy for this channel is $\sim$ 100 eV. Interestingly, one clear trend in the simulation, namely smaller slopes with increasing carbon charge states are clearly visible in the data reflecting the fact that most protons – three out of four – are closer to the carbon ion.

All charge states where the simulation produces energies that are in the range of the measured KEDs, are predominately created by absorption of a single photon. This also gives an upper limit on the timescales on which the protons fly away from the heavy ions that is on the order of less than 5 fs.

The protons with the lowest kinetic energy produced by the simulation for equilibrium geometry are originating from the selenium site assuming that only Se and the neighboring H have a charge of 1+ each. This results in protons with an energy

of 9.7 eV, indicated in figure 4.11 as "$Se^{1+}C^{0}$". Protons of this energy are present in the low-energy part of all measured proton KEDs. For higher charged channels with C^{2+} and C^{3+}, the KED is shifted to higher energies and, thus, a small feature around 10 eV can be distinguished – most prominently for the channels of $Se^{3+}C^{2+}$, $Se^{1+}C^{3+}$, and $Se^{6+}C^{3+}$ in figure 4.11.

In conclusion of this section, it was found that for final charge states that are higher than $Se^{2+}C^{2+}$ and that are produced by absorption of more than one photon, the ionization and the motion of the nuclei happen on comparable timescales leading to significant lower kinetic energies of ions (especially of protons) than predicted by a simple Coulomb explosion model that assumes equilibrium geometry of the methylselenol molecule. In the next section, the question of whether this interplay of nuclear motion and sequential ionization affects the possibility to determine the molecule's orientation in space will be discussed.

4.2.5 Determination of Molecular Geometry and Orientation by Way of Ion Coincidences

One of the motivations of this work was to examine the feasibility of determining the molecular orientation of a polyatomic molecule in the course of multiple inner-shell photoionization by an intense X-ray FEL pulse. The idea behind is to measure the 3D momentum vectors of (fast) ionic fragments, in particular, protons, which then might provide information on the molecular orientation in the spectrometer (lab) space. This was partly triggered by findings in molecular dynamics simulations on the response of larger bio-molecules on intense X-ray FEL irradiation finding fast protons and other highly charged fast ions [12]. If true, this could provide the long-sought-after possibility to determine the orientation of biomolecule in a single FEL shot desperately needed to sum up the respective photon (coherent) scattering patterns for extracting 3D structure information of individual large biomolecules [139].

The knowledge of molecular orientation for a single molecule in the FEL focus would allow for a multitude of other spectroscopic measurements, and is a well established tool in X-ray synchrotron[16] experiments [140, 141, 142, 143, 144]. Some measurements can only be done in a fixed molecular frame, because averaging over a broad distribution of molecular orientations washes out any anisotropy in the

[16]Here the repetition rate of the light pulses is a few MHz compared to 120 Hz at the LCLS.

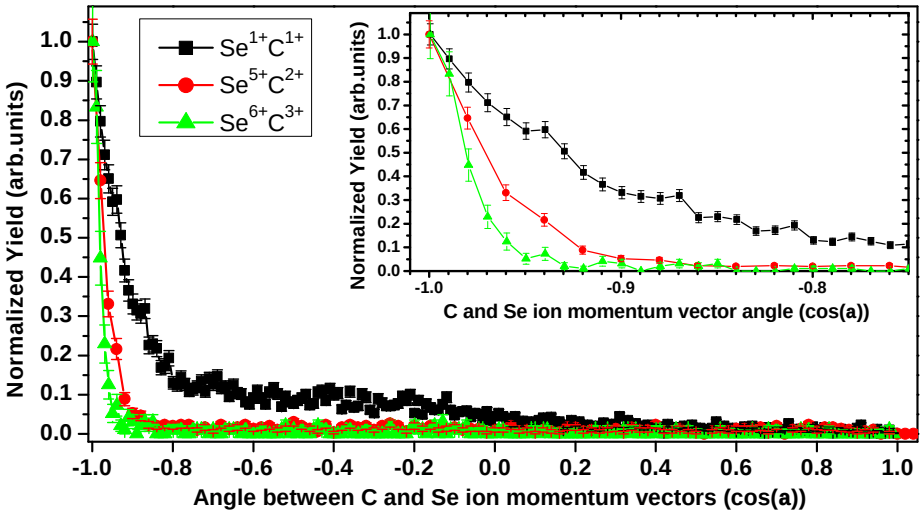

Figure 4.13: Measured relative angular distributions of the momentum vectors of C and Se ions detected in coincidence. The distributions are peaked around cos(α)= -1.0 corresponding to 180° between the momentum vectors of the ions ("back-to-back" motion).

angular distribution of ions and electrons.

For the study of molecular orientation by inspecting fragment momentum vectors, methylselenol represents an ideal benchmark molecule as it has both, a heavy atom site, allowing for increased X-ray absorption, a hydrogen atom attached to the Se that is ejected after Se ionization, and a hydrocarbon group which "represents" the main constituents of a larger biomolecule, eventually producing a proton "background".

Technologically, this is achieved by the 3D-momentum imaging technique, where the full 3D momentum of multiple fragments is determined as introduced in chapter 3. The technique of structural determination of small molecules by ways of fast fragmentation is also called Coulomb explosion imaging (CEI) and was described in section 2.3.1.

As can be seen from figure 4.3, the methylselenol molecule contains three hydrogen atoms adjacent to the carbon, with identical angles with respect to the Se-C axis, and only one H attached to the selenium site. In order to determine the molecular orientation, channel-selective angular distributions of the ionic fragments are investigated.

The molecule has a figure or pseudo-symmetry axis defined by its two heavy atoms – the Se−C bond. Since proton momenta are typically considerably smaller

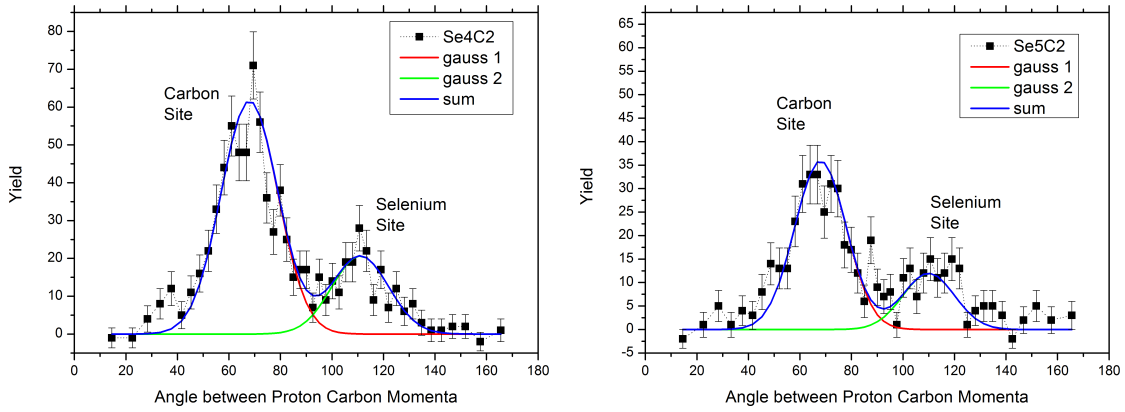

Figure 4.14: Angles between proton momentum vectors and carbon ion momentum vector for $Se^{4+}C^{2+}$ and $Se^{5+}C^{2+}$ coincidences. Both channels show a clear two-peak structure that can be fitted by a superposition (blue) of two Gaussian curves (red and green) of a width of 20° (FWHM) each. The relation of the areas under the two fits is in both cases is three to one.

than those of the heavy fragments, Se and C fragments are emitted almost strictly "back-to-back" such that the carbon or selenium momentum vectors indicate the orientation of the Se−C axis. The measured distribution of angles between C and Se ion momentum vectors, detected in coincidence, are shown in figure 4.13 for some channels. From the angular distributions for three exemplary heavy-ion charge states depicted, one can see that the assumption of Se and C ions flying back-to-back is more valid for higher charge states, showing a very sharp peak corresponding to 180° between the Se and C momentum vectors, allowing for a clear determination of the Se−C axis by the carbon momentum vector alone.

For dissociation channels with low Se and C charge, such as $Se^{1+}C^{1+}$, the angular correlation is rather broad which leads to the conclusion that for this channel the Se and C ions are not always flying back to back but are influenced by proton momentum contributions. This is only significant for low-charged channels where dissociation happens more slowly.

Exemplary distributions of emission angles between the carbon and proton momentum vectors for $Se^{4+}C^{2+}$ and $Se^{5+}C^{2+}$ coincidences are shown in figure 4.14. The distribution manifests two distinct features centered around 70° and 110°. The width of the peaks is defined by the width of the Se-C angle distribution and angular motion of the proton en route to multiple ionization. It was determined by a Gaussian fit to have a full width at half maximum of 20°, and the ratio of the areas

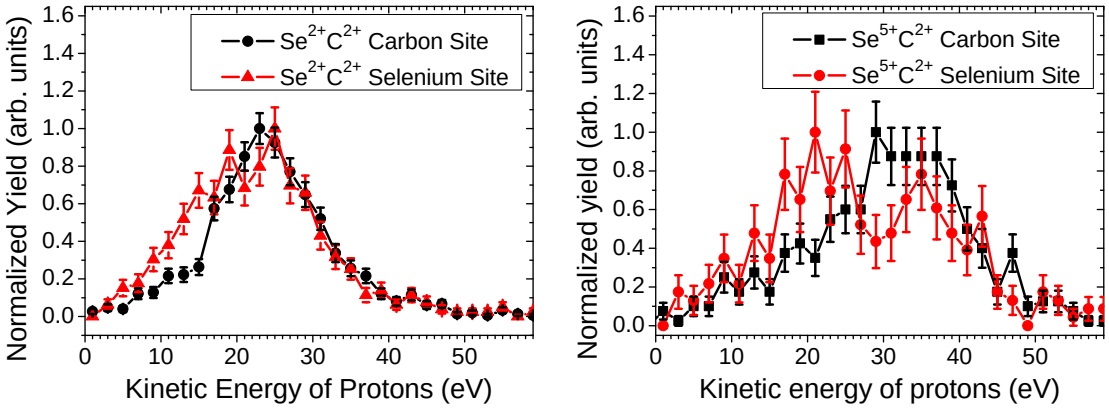

Figure 4.15: Kinetic energy distributions for protons with C and Se neighbors, respectively. In both channels, the protons corresponding to the selenium site show increased yields compared to the carbon site at low KE around $\sim$ 10 to 20 eV, corresponding to the simulated energies of protons that result from a system of $Se^{1+/2+}$ and H^+ and an otherwise neutral molecule.

under the respective fits is 3 : 1, corresponding to the three hydrogens next to the carbon and the one next to the selenium. This finding also represents a verification for the assumption of four charged protons is justified for the two channels shown (and possibly also for channels with higher charge states).

Considering the angles from literature [145] in the equilibrium geometry of methylselenol, which are 70.0° for the protons next to carbon and 95.5° for the protons next to selenium, it is clear that the measured angles for the carbon-site protons are in good agreement with the equilibrium geometry, whereas the measured angles for the protons from the selenium-site are larger than expected. This is due to the nature of the Coulomb explosion, where each charged particle interacts with all its charged neighbors. Because of the geometry of the molecule, with a $\sim 90°$ bond angle of the C−Se−H site and bond lengths of $d_{\mathrm{H-Se}} = 1.53$Å and $d_{\mathrm{C-Se}} = 1.97$Å, the distance between the Se proton and the carbon is only 2.49Å. This leads to a significant contribution from the carbon charge, producing a larger "selenium" proton angle. This is also discussed in UV-photo dissociation studies on H_2S [146].

The KEDs for protons corresponding to the selenium- and carbon-sites are shown in figure 4.15. In the symmetrically charged $Se^{2+}C^{2+}$ channel (left), the high-energy side of the KEDs are very similar. Even the more asymmetric channel of $Se^{5+}C^{2+}$ shows the same maximum kinetic energy for both, the selenium and the carbon site protons.

In contrast, a clear difference between the "carbon" and "selenium" protons can

be observed for both channels in the low-energy part of the spectra, namely, considerable enhancement of low-energy features around 10 eV to 20 eV are found for the Se site protons. According to the simulation, this would correspond to the proton originating from the vicinity of a singly or doubly charged Se atom, with the rest of the molecule remaining neutral, that was simulated to result in protons of energies 9.7 eV and 19.3 eV (as shown in figure 4.11). This distinct feature, which can be observed for essentially all final charge-state combinations, suggests that the low-energy part of the proton KED reflects the initial step in the sequential build-up of the total charge of the molecule, whereas the high-energy tail is due to reaction channels where the molecule is charged fast (before significant nuclear displacement occurs), and is strongly influenced by the charge rearrangement dynamics.

4.3 Ionization and Fragmentation in Ethylselenol

The multi-photon ionization of ethylselenol, presented in this section, represents the extension of the studies described above towards larger systems. In terms of the molecular constituents, another methylene group ($-CH_2-$) is added, resulting in CH_3CH_2SeH – a molecule with three heavy constituents and six hydrogen atoms (see figure 4.19(d)). The two carbons are attached to the selenium in the form of a chain (ethyl group).

In ethylselenol, the decay of the L-shell vacancy in Se can now involve two carbon and six hydrogen atoms. The multiple ionization and charge redistribution dynamics discussed in the last section for the case of methylselenol, are studied in the following for this more complex system, employing very similar methods and tools. The data for ethylselenol were taken at a photon energy of 1.7 keV.

4.3.1 Charge Distribution

The heavy-ion charge states of the molecule are identified in the same way as described for the case of methyselenol in section 4.2.2. The FEL shots where three ions originate from the same molecule, such as $[Se^{2+}C^{1+}C^{1+}]$, are identified by using a gate-window in the time-of-flight spectrum corresponding to the individual arrival times of the ion species. After the three ions are identified, their momenta are calculated from the corresponding time and position signals.

The resulting yields of all identified heavy-ion charge states produced from ethylselenol after irradiation with 5 fs, 1700 eV, 0.4 mJ FEL pulses is shown in figure 4.16. The channels with $[Se^{x+}C^{2+}C^{1+}]$ and $[Se^{x+}C^{1+}C^{1+}]$ have the overall highest abundances. Higher charges of the carbon ions are produced less likely as can be seen from the significant drop in abundance for $[Se^{x+}C^{3+}C^{1+}]$, $[Se^{x+}C^{2+}C^{2+}]$, and $[Se^{x+}C^{3+}C^{2+}]$ channels. These channels show a plateau-like abundance, all having comparable similar yields with respect to each other. The statistics for the $[Se^{x+}C^{3+}C^{3+}]$ channels is insignificant and does not allow for any further interpretation. Note that the channels of $[Se^{7+}C^{1+}C^{1+}]$, $[Se^{7+}C^{2+}C^{1+}]$, and $[Se^{7+}C^{3+}C^{1+}]$ were omitted from the analysis[17] and are, thus, not present in figure 4.16.

For high selenium charges, namely Se^{8+} and Se^{9+}, the channels with different

[17] Similar to methylselenol, the overlap of C^+ and Se^{7+} in the ToF because of their same mass to charge ratio did not allow for their clear distinction and did not allow further analysis.

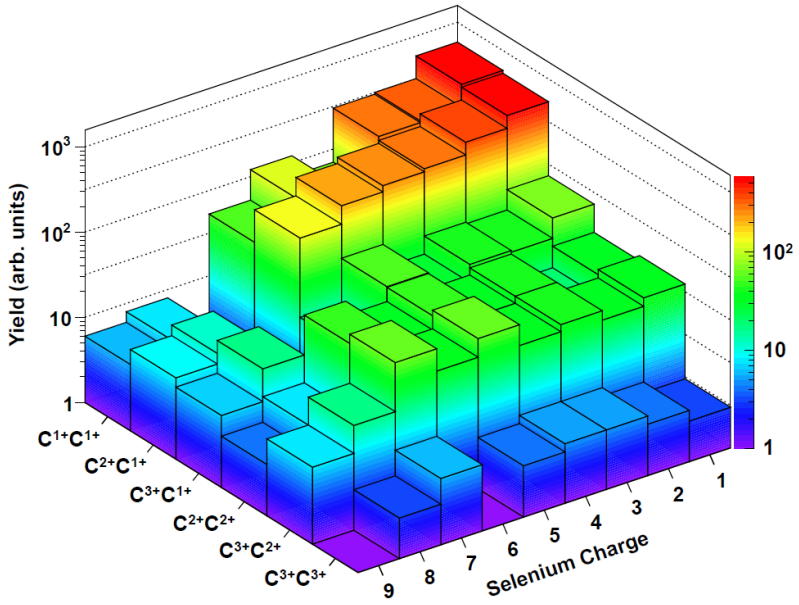

Figure 4.16: Overview of the yield of the heavy-ion coincidence channels of ethylselenol. Note that channels of $[Se^{7+}C^{1+}C^{1+}]$, $[Se^{7+}C^{2+}C^{1+}]$, and $[Se^{7+}C^{3+}C^{1+}]$ are omitted because of hard-to-quantify contributions of false coincidences between Se^{7+} and C^{1+}.

charge states on the two carbon ions (non-symmetric) show higher abundances than those with symmetric charge. This can be attributed to the charge redistribution mechanism of inter-atomic Auger decay that involves the carbon next to the initial Se core-vacancy more than the carbon atom at a larger distance. However, a conclusive proof cannot be provided for all channels, as the two carbon ions detected could not be clearly attributed to their initial position in the ethylselenol molecule, as will be further discussed in sections 4.3.2 and 4.3.3.

For channels with higher carbon charges, the yield as a function of selenium-ion charge shows a maximum that is not at Se^{1+} but at Se^{5+} to Se^{7+}. This is another indication for redistribution of the charges in the course of an inner-shell vacancy decay initially located at the selenium site. The average charge state for individual single ions from ehylselenol is $\bar{q}_C = 1.33$ for carbon ions and $\bar{q}_{Se} = 2.97$ for selenium ions, as calculated considering all coincident ion channels.

Figure 4.17 shows the heavy-ion charge measured for ethylselenol fragmentation (gray bars), in comparison with the charge induced in atomic krypton at a photon energy of 2000 eV (red bars). Here, the heavy-ion charge distribution without taking into account the charges carried by the hydrogen fragments closely resembles the

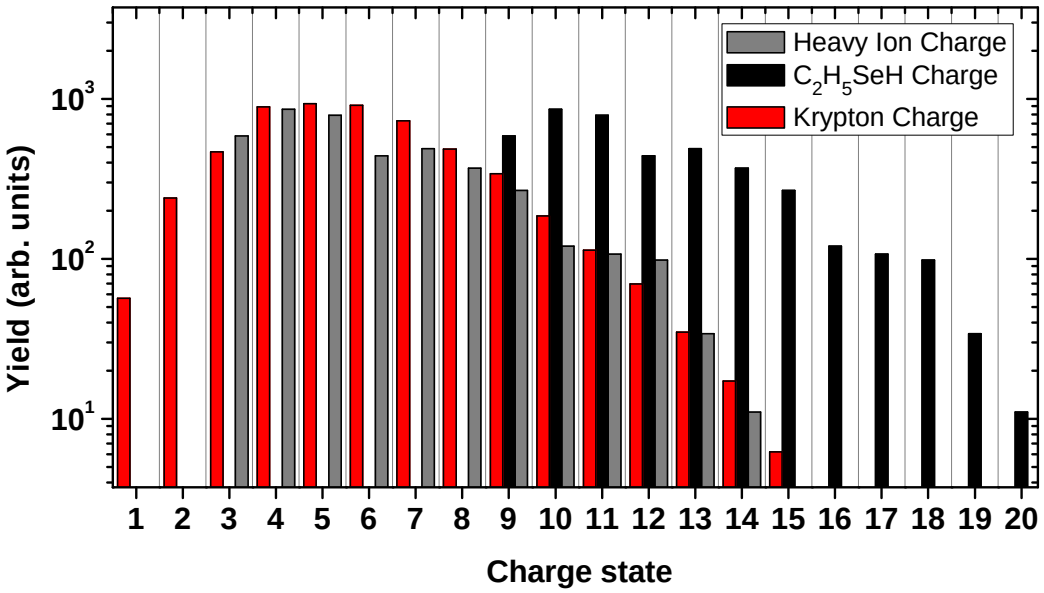

Figure 4.17: Measured abundance of total heavy-ion charge states in ethylselenol after irradiation with an FEL pulse (5 fs; 1700 eV; 0.4 mJ) compared to the charge-state abundance in atomic krypton (5 fs; 2000 eV; 0.4 mJ).

data for krypton, which might seem surprising on first glance. The average charge state induced in Kr, is $\bar{q}_{\mathrm{Kr}} = 5.92$, whereas for ethylselenol the average heavy-ion charge is $\bar{q}_{\mathrm{Se+C+C}} = 5.93$. If all the hydrogen atoms are considered to be charged as well, as was found to be a good assumption for the case of methylselenol, six charges would have to be added to the distribution (black bars). This obviously leads to much higher charge states than those observed for krypton. Although for the case of ethylselenol, where three hydrogen atoms are situated far away from the absorbing Se atom, the assumption of all six protons being charged does not seem realistic, the data presented in figure 4.17 do indicate that the total charge of the ethylselenol molecule is higher than that of krypton atoms. Possible reasons for this are the higher absorption cross section at the lower photon energy used for the ethylselenol measurement, and a considerably larger number of electrons available for Auger cascades and other secondary ionization channels.

4.3.2 Fragment Kinetic Energies

The kinetic energies measured for Se and C ions are shown in figure 4.18. The KEDs represent two exemplary groups of channels, namely $[\mathrm{Se}^{2+}\mathrm{C}^{2+}\mathrm{C}^{x+}]$ and $[\mathrm{Se}^{4+}\mathrm{C}^{2+}\mathrm{C}^{x+}]$,

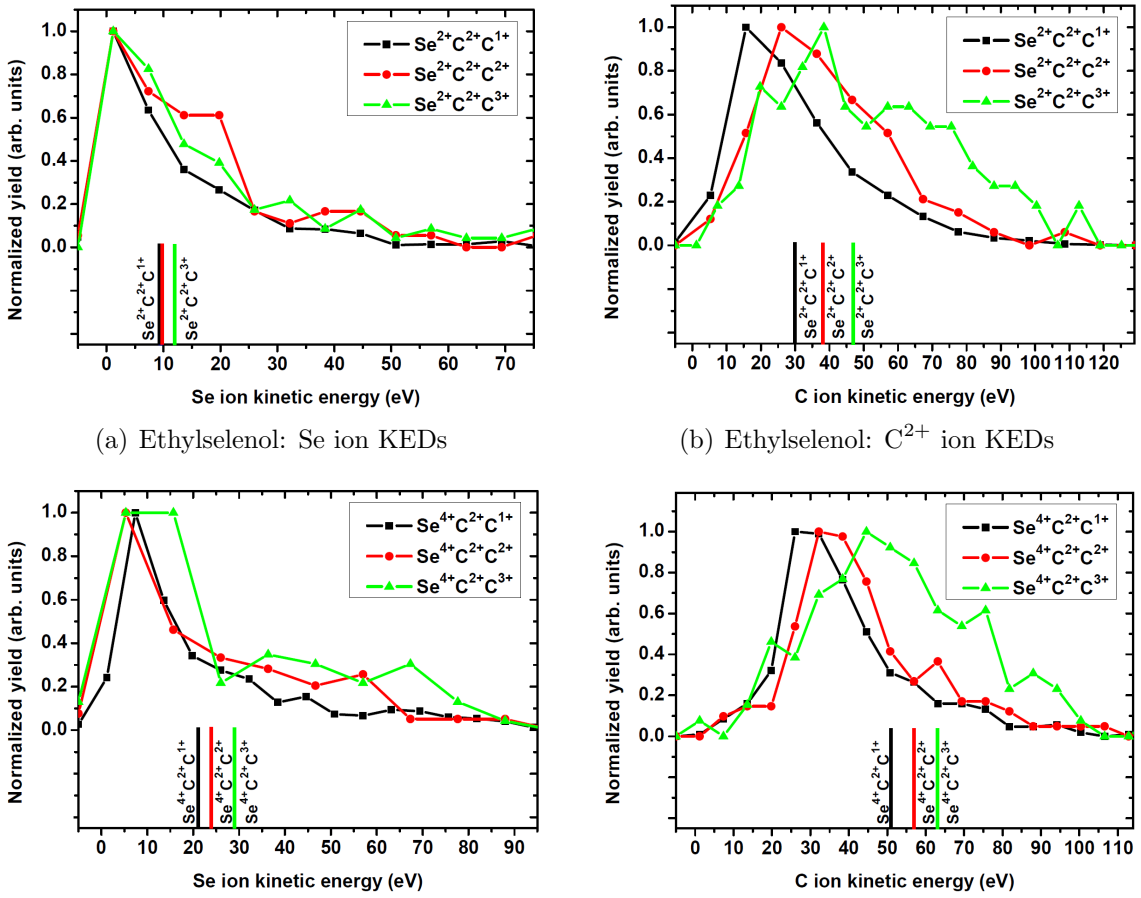

(a) Ethylselenol: Se ion KEDs

(b) Ethylselenol: C^{2+} ion KEDs

(c) Ethylselenol: Se ion KEDs

(d) Ethylselenol: C^{2+} ion KEDs

Figure 4.18: Kinetic energy distributions for ionic fragments of ethylselenol irradiated with a 5 fs, 0.4 mJ FEL pulse of 1700 eV photons. Simulated energies are indicated as vertical lines of the same color.

where only the charge on one of the two carbon atoms varies.

The selenium KEDs do not significantly change for the different channels shown in figures 4.18(a) and 4.18(c). The KEDs peak at 1 eV for the $[Se^{2+}C^{2+}C^{x+}]$ channels and at around 5 eV for the $[Se^{4+}C^{2+}C^{x+}]$ channels. The output values for Se ions of the Coulomb explosion simulation, assuming equilibrium distances, are shown as vertical lines of the same color in figures 4.18(a) and 4.18(c), always producing energies that are larger than the values of the maxima of the measured KEDs. For the $[Se^{4+}C^{2+}C^{x+}]$ channels, this discrepancy between measurement and the simulation is even larger.

The measured KEDs for carbon 2+ ions for the groups of channels of $[Se^{2+}C^{2+}C^{x+}]$

and $[Se^{4+}C^{2+}C^{x+}]$ are shown in figures 4.18(b) and 4.18(d) , respectively. The C^{2+} KEDs show a dependence on the charge of the C^{x+} (second carbon constituent) that is more pronounced than for the selenium ions, where the measured kinetic energies shift towards higher energies for increasing C^{x+} charge. In comparison to the simulation, however, the two groups of channels show a different behavior. Those of $[Se^{2+}C^{2+}C^{1+}]$, $[Se^{4+}C^{2+}C^{1+}]$, $[Se^{4+}C^{2+}C^{2+}]$ produce C^{2+} ions with kinetic energies that are lower than the simulated energies for the same channels (vertical lines of same color shown in figures 4.18(b) and 4.18(d)). However, the channels of $[Se^{2+}C^{2+}C^{3+}]$, $[Se^{2+}C^{2+}C^{2+}]$, and $[Se^{4+}C^{2+}C^{3+}]$ show broad KEDs that are exceeding the simulated kinetic energies for C^{2+} ions.

This, most likely, has the same reasons as discussed for the case of $q_C > q_{Se}$ in methylselenol. In ethylselenol, however, these "asymmetric" channels have the form $(q_{C,1} + q_{C,2}) \geq q_{Se}$, which is fulfilled by all three cases discussed above. In order to reproduce the measured high-energy tail of the distribution, charge states of the heavy fragments higher, than those finally detected, have to be put into the simulation.

4.3.3 Three-Body Breakup

Figure 4.19 shows angular correlations between the selenium and the two carbon ions for the three channels $[Se^{1+}C^{2+}C^{1+}]$, $[Se^{2+}C^{2+}C^{1+}]$, and $[Se^{3+}C^{2+}C^{1+}]$. The asymmetric channels with $(q_{C,1} + q_{C,2}) \geq q_{Se}$ in figures 4.19(a) and 4.19(b) show broad angular distributions as well as some features of carbon-carbon angles around 90° ($\cos(\alpha) = 0$), 80° ($\cos(\alpha) = -0.2$), and even smaller angles. This is different for the $[Se^{3+}C^{2+}C^{1+}]$ channel shown in figure 4.19(c) where the angular distribution has a rather narrow peak around $\cos(\alpha) = -0.29$ corresponding to a selenium-carbon angle of 107° (in good agreement with the equilibrium angle of 110°) and a carbon-carbon angle of about 130° ($\cos(\alpha) \approx -0.64$). This corresponding geometric arrangement is illustrated in figure 4.19(d).

The good agreement with expected angles for higher Se charges suggests that the determination of the molecular orientation and, consequently, the distinction between the two carbons ions, one next to selenium and the one further away, is in general possible, given the short, intense 5 fs FEL pulses used. However, the low statistics of the measurement presented here, that in particular affects channels with higher selenium charges, does not allow for precise determination of the angles

because of broad distributions. In addition to that, the momentum vectors of all three fragments lie roughly in the same plane and have angles of about 130° with respect to each other, making an unambiguous assignment of the carbon ions even more challenging. Detailed, angular-resolved analysis of ion yields as well as studies of bending motion in the molecule upon multiple ionization is, thus, not further pursued in this work.

Nevertheless, for the $[Se^{3+}C^{2+}C^{1+}]$ channel shown in figure 4.19(c), the angular distributions give a hint, that the C^{2+} ion is originating from the site close to the selenium and the C^{1+} ion is from the site further away. This supports the earlier hypothesis that in "asymmetric" channels the carbon ions with higher charge states are the ones closer to the selenium site having a larger overlap for inter-atomic Auger decay.

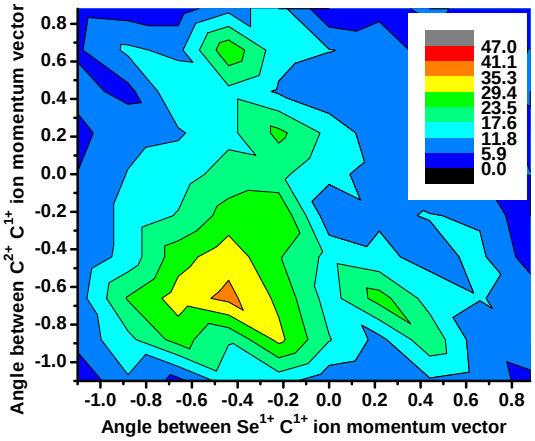

(a) Ethylselenol: $[Se^{1+}C^{2+}C^{1+}]$

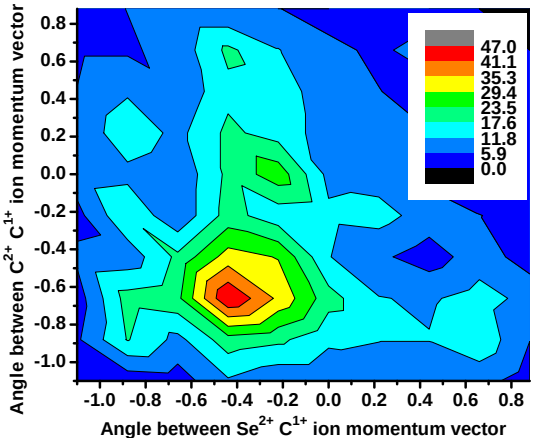

(b) Ethylselenol: $[Se^{2+}C^{2+}C^{1+}]$

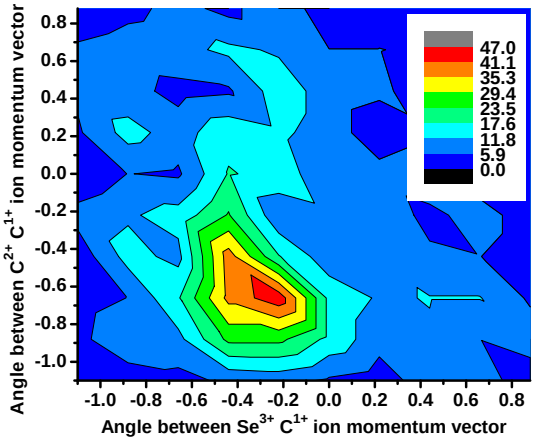

(c) Ethylselenol: $[Se^{3+}C^{2+}C^{1+}]$

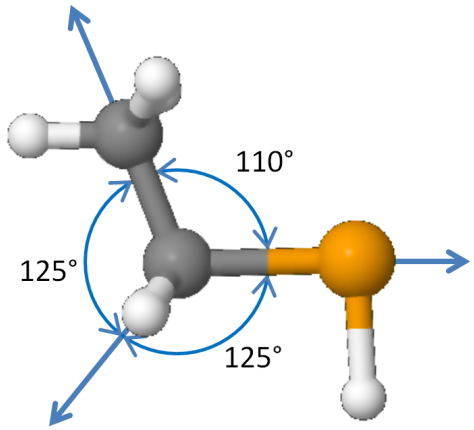

(d) Ethylselenol: Fragmentation geometry

Figure 4.19: Angular correlations between the three heavy-ion fragments for three different channels (a - c). Angles are given in values of $\cos(\alpha)$. For the $[Se^{3+}C^{2+}C^{1+}]$ channel a schematic of the measured angles is given (d), indicating the directions of the measured momentum vectors (blue arrows).

4.4 Iodine Chloride

In this section, experimental results on multiple ionization and fragmentation of the iodine chloride (ICl) molecule are presented. The main goal of this study is to extend the experiments on selenium-containing compounds described in the previous sections towards chemically different molecular systems with even heavier atomic constituents. The interhalogen molecule, iodine chloride, is composed of iodine and chlorine atoms forming a highly polar covalent bond because of their difference in the electronegativity. The molecule has an average mass of 162.4 amu and contains 70 electrons. The high-Z of the iodine constituent results in an increased photoabsorption cross sections and, thus, in the production of even higher charge levels compared to the studies presented so far in this thesis. The study of iodine-containing molecules is further motivated by earlier results on atomic xenon [24, 121], a system with similar absorption cross sections and inner-shell electronic structure to iodine. In xenon, ultra-efficient ionization at 1500 eV photon energy, leading to the production of extremely high charge states up to Xe^{36+}, was observed for a pulse energy of 2.5 mJ and a (nominal) pulse duration of 120 fs. Furthermore, the fact that ICl is a diatomic molecule removes the uncertainties in the determination of the final charge states, discussed in sections 4.2.2 and 4.3.1, allowing for the clear separation of different fragmentation channels.

In order to compare the data with the earlier results on xenon [24, 121], charge-state distributions for the fragmentation of ICl were measured at two different photon energies, 1500 eV and 2000 eV. The analysis of the kinetic energies of ionic fragments is performed only for the photon energy of 1500 eV, where considerably higher ionization levels are achieved.

4.4.1 Charge Distribution: A Half-Stripped Molecule

To determine the total charge produced in the ICl molecule upon multiple photoionization by an intense 120 fs FEL pulse, coincident detection of the iodine and chlorine ions is employed. In the present case of a diatomic molecule, the identification of different fragmentation channels is much simpler than for the polyatomic molecules discussed before. First, it is now possible to measure all fragments in coincidence without requiring very large statistics (relative to the molecules presented before). This removes the uncertainties introduced by incomplete measurement of all ionic

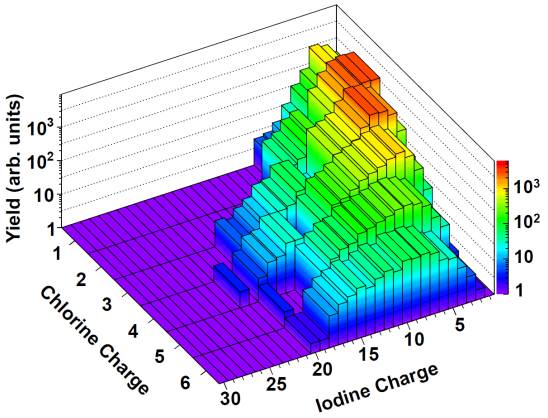

(a) Iodine chloride: Channel yields for $\hbar\omega$ = 2000 eV; 120 fs; 3.6 mJ

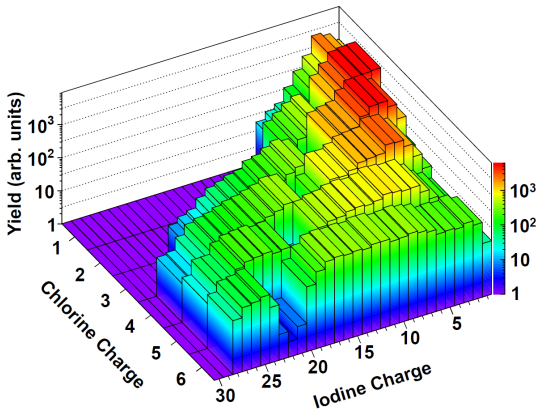

(b) Iodine chloride: Channel yields for $\hbar\omega$ = 1500 eV; 120 fs; 2.5 mJ

Figure 4.20: Yield of individual coincident ion channels for iodine chloride for two different photon energies. Prominent "dips" in the distributions such as the one around $I^{22+}Cl^{6+}$ are artifacts from the analysis which result from the suppression of false coincidences between two chlorine ions which are dominating at channels where iodine and chlorine ions have very similar mass to charge ratios and, thus, a similar time-of-flight.

fragments. Second, the ICl molecule is almost monoisotopic, with iodine having only a single isotope and chlorine having only two isotopes with a ratio of about 3 to 1. This results in the reduction of ambiguous assignment of mass due to isotopes and, thus, improves the precision of coincidence determination.

The abundances of the measured final charge states, as determined by coincidence detection of both ionic fragments, for iodine chloride irradiated by an 120 fs FEL pulse for the two photon energies of 1500 eV and 2000 eV are shown in figure 4.20.

From figure 4.20(a) it can be seen that the charges of the Cl and the I ions are correlated. The iodine charge state having the highest yield is changing as a function of the coincident chlorine charge state.

Comparing figure 4.20(a) and figure 4.20(b), it is obvious that at 1500 eV, much higher charge states are created, at an even lower total pulse energy of 2.5 mJ (2 keV 3.6 mJ) corresponding however, to similar numbers of photons in the pulses. While for 2000 eV, the highest charge states observed with statistical significance are $I^{20+}Cl^{6+}$ and $I^{21+}Cl^{5+}$, charge-state combinations up to $I^{28+}Cl^{6+}$ are measured at 1500 eV photon energy. The latter represents a final state where the molecule has lost almost half of its 70 electrons.

For the case of 2000 eV, the average charge state measured for chlorine ions is

$\bar{q}_{\mathrm{Cl}} = 2.87$ and for iodine $\bar{q}_{\mathrm{I}} = 4.96$. The average total charge induced in the ICl molecule is $\bar{q}_{\mathrm{Cl+I}} = 7.83$ ($\bar{q}_{\mathrm{Xe}} = 7.22$). At 1500 eV, the average charge state measured for chlorine ions is $\bar{q}_{\mathrm{Cl}} = 3.25$ and for iodine $\bar{q}_{\mathrm{I}} = 6.62$. The average total charge induced in the ICl molecule is $\bar{q}_{\mathrm{Cl+I}} = 9.87$ ($\bar{q}_{\mathrm{Xe}} = 9.75$). Note that the Xe data were taken under the same experimental conditions of pulse duration, pulse energy, and focus size. These numbers prove that the overall charge induced in ICl is increased significantly for 1500 eV photon energy, compared to 2000 eV. This can be understood qualitatively by considering the larger cross section for the iodine M-shell ionization at 1500 eV, compared to 2000 eV, where the L-shell of iodine is still out of reach. The difference is further enhanced by the effect of *resonance-enabled X-ray multiple ionization* (REXMI) [24], which for the case of atomic Xe was shown to play an important role in the present intensity regime at 1500 eV, but not at 2000 eV, leading to a difference in the charge-state distributions for these two photon energies similar to the one observed in this work for ICl.

To compare the present results with the measurements for atomic Xe[18], the abundances of the total charge states in ICl are deduced from figure 4.20 by adding the yields of channels with same sum charge $q_{\mathrm{I}} + q_{\mathrm{Cl}}$. These yields are shown in figure 4.21 as a function of the sum-charge for the two photon energies of 1500 eV and 2000 eV.

From the comparison of ICl and Xe at 1500 eV (figure 4.21(b)), it is apparent that for both distributions, the maximum charge state is around 34+, and the overall distribution is very similar for both targets. The shapes of the distributions, however, exhibit some minor differences for charge states above 22+. The distribution of ICl shows a smooth monotonic decrease towards higher charge states, whereas Xe shows a "hump", at around 27+.

In the case of 2000 eV photon energy, the charge distributions of Xe and ICl are very similar. In both cases the charge state up to 26+ are observed.

Going back to figure 4.20, another feature that can be found in the channel yields for 1500 eV, besides the much higher total charge states, is the increase in channels with high chlorine but low iodine charge, such as $I^{3+}Cl^{6+}$ and $I^{3+}Cl^{5+}$, which are almost absent in the 2000 eV photon energy measurement.

The production of high chlorine charge states, however, can happen differently

[18]For detailed information on the multi-photon ionization of xenon see reference [24] and the dissertation of Benedikt Rudek [121]

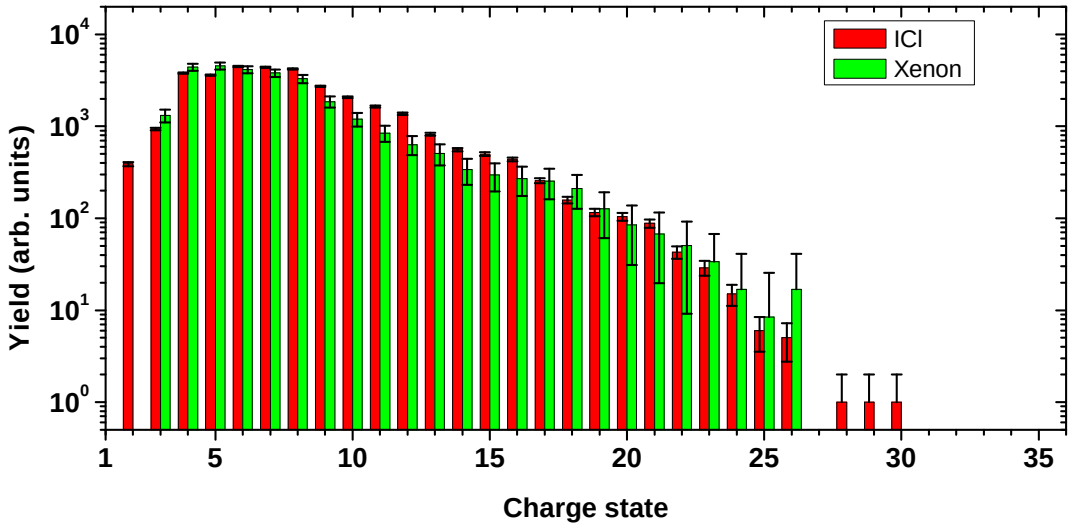

(a) Iodine chloride: Charge-state abundance for $\hbar\omega = 2000\,\mathrm{eV}$; 120 fs; 3.6 mJ

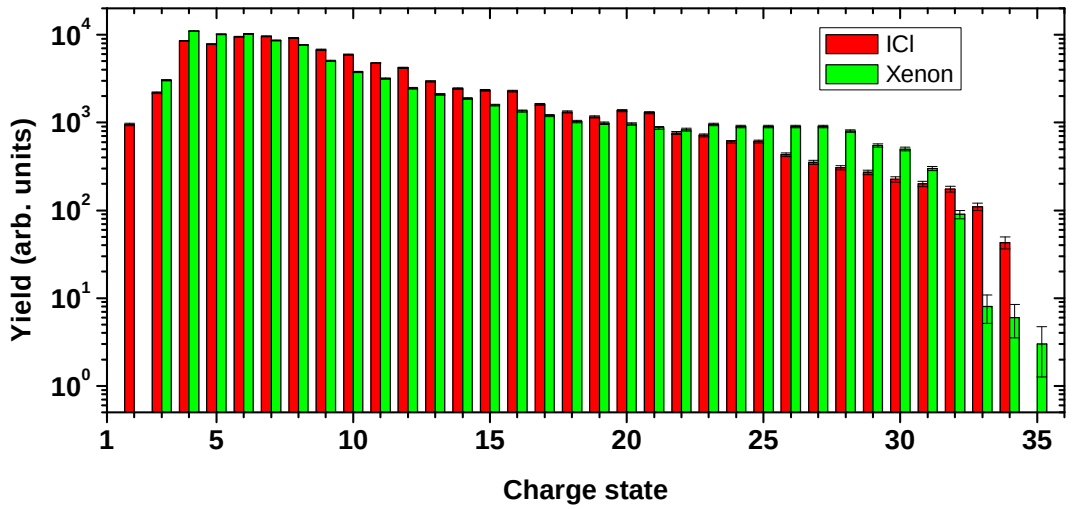

(b) Iodine chloride: Charge-state abundance for $\hbar\omega = 1500\,\mathrm{eV}$; 120 fs; 2.5 mJ

Figure 4.21: Charge-state abundances of iodine chloride ($q_\mathrm{I} + q_\mathrm{Cl}$) and xenon for two different photon energies of 2000 eV and 1500 eV. The ICl and Xe data were taken with the same beam parameters.

than for the afore discussed asymmetric channels in selenols, with high carbon charge states. This is because of the relative magnitude of the photoabsoption cross sections between the two heavy constituents in each of these molecules. Whereas the ratio in cross sections are more than 60 to 1 between selenium and carbon in methylselenol, the ratio between iodine and chlorine[19] is about 14 to 1 only.

In order to estimate the effect of the photoabsorption by the chlorine atom, one can consider single-photon ionization of the Ar L-shell at $\sim 1500\,\mathrm{eV}$ studied in reference [46], since Ar has an absorption cross sections and electronic structure similar to Cl. There, charge states up to Ar^{6+} are produced, and the highest abundances were observed for Ar^{2+} (47%) and Ar^{3+} (37%). Expecting similar ionization level of the chlorine atom, one can assume that the asymmetric channels with $q_{\mathrm{Cl}} > q_{\mathrm{I}}$ in the case of ICl are produced by single or two-photon absorption by the chlorine L-shell rather than by sequential multi-photon absorption of the iodine M-shell and subsequent inter-atomic molecular Auger decay.

4.4.2 Kinetic Energies of Iodine and Chlorine Ionic Fragments

For the study of the ionization dynamics in iodine chloride, the kinetic energies of the two fragment ions are investigated. In comparison to methylselenol, the two atoms in ICl have both relatively high masses of $m_{\mathrm{Cl}} = 35.5\,\mathrm{amu}$ and $m_{\mathrm{I}} = 126.9\,\mathrm{amu}$. This suggests ion motion to be slower for the same kinetic energies. On the other hand, as shown above, total charge states produced in ICl are considerably higher.

The kinetic energy distributions for iodine and chlorine ions, measured in coincidence, are shown in figure 4.22 for a few exemplary final charge states. Note that yields of some channels are scaled as indicated in the figure to give a better overview.

Both, iodine and chlorine KEDs show very good agreement with simulated energies for the lowest channel that is shown, i.e $I^{3+}Cl^{1+}$. Similar to the case of methylselenol discussed in section 4.2.4, the KEDs of the higher charge-state channels show a maximum at an energy that is smaller than that of the simulation. This discrepancy increases with higher total charge state. For the $I^{9+}Cl^{6+}$ channel the simulated energies are beyond the high-energy tail of the measured KEDs. Similar to the case of Se containing compounds, the deviations of the maxima of the mea-

[19] Total photoabsorption cross sections: At 1500 eV: 824 kBarn for iodine, 57.4 kBarn for chlorine; At 2000 eV: 419 kBarn for iodine, 26.5 kBarn for chloride (values calculated using XCOM, NIST)

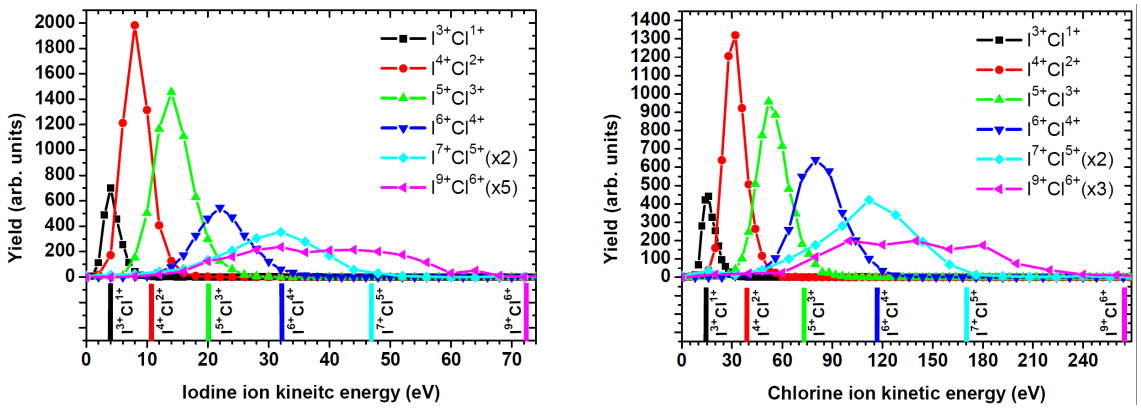

(a) Iodine ion kinetic energies for $\hbar\omega = 1500\,\mathrm{eV}$

(b) Chlorine ion kinetic energies for $\hbar\omega = 1500\,\mathrm{eV}$

Figure 4.22: Kinetic energy distributions of iodine (a) and chlorine (b) ions for a representative set of final charge states. Kinetic energies produced by the Coulomb explosion simulation are shown as vertical lines of the same color with respective channel names next to them. Note that the yield of some channels was multiplied by a factor (as indicated in the legend) to allow for a better contrast.

sured KEDs from the simulated CE values originate from the motion of the nuclei on the time scale of multiple ionization.

By adding the kinetic energies of both fragments measured in coincidence on a shot-to-shot basis, the sum kinetic energy (sKED) is produced. These sKEDs are shown as a function of the charge-state product $q_\mathrm{I} \times q_\mathrm{Cl}$ in figure 4.23.

The maxima of the sKEDs for individual charge-state combinations are indicated by respective symbols; the vertical bars give the (non-symmetrical) widths of the distribution at half maximum height. The red curve in figure 4.23 indicates the calculated Coulomb-repulsion energy for the respective charge-state product, using the equilibrium internuclear distance $R = 2.32\mathring{\mathrm{A}}$.

It can be seen that the measured energies are in agreement with the calculated curve for channels up to a charge-state product of ~ 10 (see zoomed view). For higher charge products, as well as for the asymmetric channels $I^{1+}Cl^{6+}$, $I^{2+}Cl^{5+}$, and $I^{2+}Cl^{6+}$ (further discussed later), the calculated energies are much higher than the measured sKEDs. This is, again, caused by the fact that significant nuclear motion happens en route to multiple ionization of the molecule. As a consequence, the two ionic fragments reach their final charge states at internuclear distances considerably larger than the equilibrium value. First, photoionization and subsequent

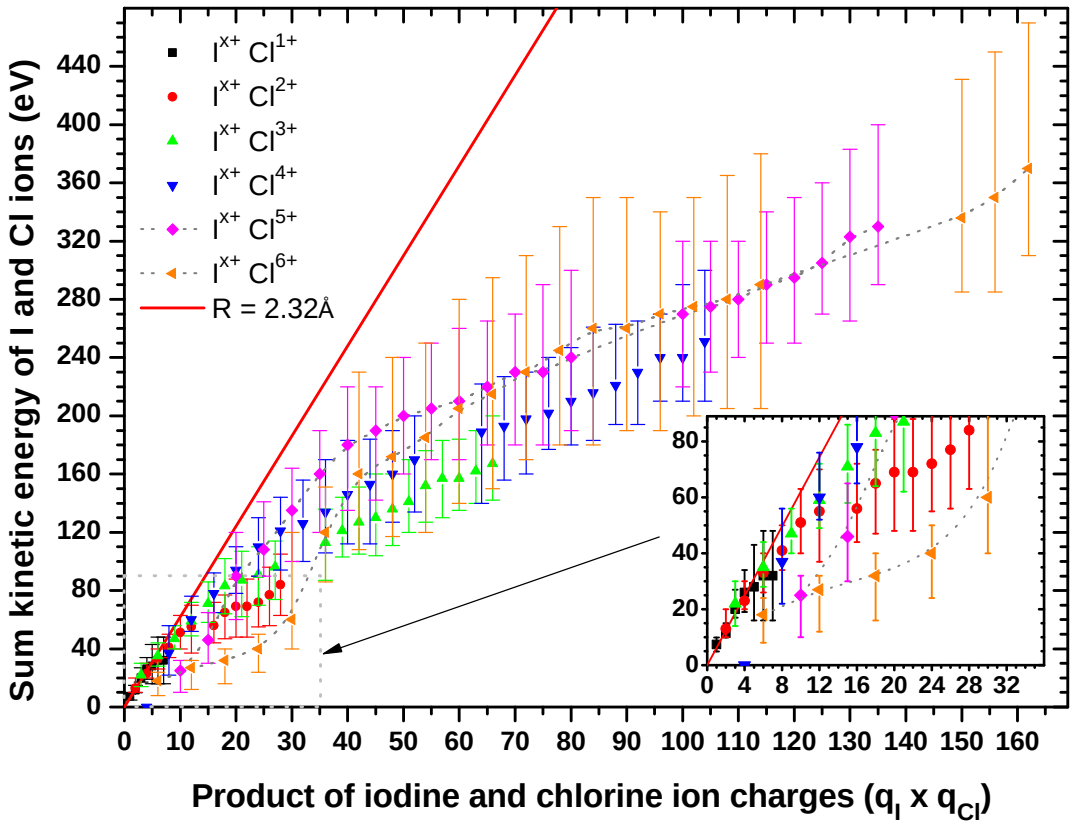

Figure 4.23: Summed kinetic energies of iodine and chlorine ions, measured in coincidence as a function of the charge-state product $q_{\mathrm{I}} \cdot q_{\mathrm{Cl}}$.

Auger decay trigger the dissociation of the molecule, and the internuclear distance begins to increase. As the charge state is further increased by slower Auger decays, and possibly, by the absorption of a second (third, fourth,...) X-ray photon, the internuclear distance has already increased and, thus, the Coulomb repulsion force is less than for the case of the same charge states at smaller (equilibrium) distance. This leads to a final kinetic energy of the fragments that is (significantly) lower than expected for vertical or instantaneous ionization at close to equilibrium internuclear distance.

Another interesting feature shown in figure 4.23 are the low sKEDs for the asymmetric channels $I^{X+}Cl^{6+}$ and $I^{X+}Cl^{5+}$ with $X < 6$. The maxima (symbols) of the sKEDs can be traced by an "S-shaped" trend, as indicated by the dotted lines connecting the $I^{X+}Cl^{5+}$ and $I^{X+}Cl^{6+}$ channel groups. The $I^{X+}Cl^{6+}$ channels with low iodine charge state have a very low sum kinetic energy that shows a steep increase at the transition from $I^{5+}Cl^{6+}$ to $I^{7+}Cl^{6+}$. As discussed above, these channels are likely

produced by photoabsorption at the chlorine atom. If this is the case, rather low sKED values can be explained by considering longer Auger lifetimes for the chlorine L-shell vacancy compared to the iodine M-shell ($\sim 6\,\mathrm{fs}$ and $\sim 0.2\,\mathrm{fs}$, respectively). This increases the average time required to reach a given final charge state, and, as explained above, results in lower kinetic energies of the fragments. The steep increase of the sKEDs for $I^{5+}Cl^{6+}$, $I^{6+}Cl^{6+}$, and $I^{7+}Cl^{6+}$ channels can then be interpreted as the transition to the pathways where absorption by the iodine M-shell starts to dominate.

4.5 Methyl Iodide

Methyl iodide is bridging the gap between the measurements on selenol compounds and iodine chloride. It allows one to study the fragmentation dynamics of a polyatomic molecule containing few hydrogen atoms in the regime of higher charge states reached by efficient iodine M-shell ionization with 1500 eV photon energy that was demonstrated for ICl.

4.5.1 Charge Distribution

The charge-state distribution induced in methyl iodide exposed to 100 fs, 1500 eV LCLS pulses is shown in figure 4.24. Charge states of up to iodine 22+ and carbon 4+ are observed in coincidence. The coincidence channels show a similar correlation between the carbon and the iodine charge than the one observed in iodine chloride.

The average charge state measured for carbon ions is $\bar{q}_{\mathrm{C}} = 1.80$ and for iodine $\bar{q}_{\mathrm{I}} = 4.10$. The average total charge induced in the ICl molecule is $\bar{q}_{\mathrm{C+I}} = 5.90$ ($\bar{q}_{\mathrm{Xe}} = 7.31$; under same experimental conditions).

The measured heavy-ion charge-state distribution for methyl iodide is shown in figure 4.25 (as indicated by the red bars). Assuming the three hydrogen atoms at the carbon site to be charged, a total molecular charge state (blue bars) can be deduced in a similar way as for the case of methylselenol (section 4.2.2). Comparing the charge-state abundance with the one measured for atomic xenon under the same experimental conditions (green bars), it can be seen that the distributions are similar. However, the maximum charge state observed as well as the shape of the xenon distribution for charge states higher than 10 do follow the methyl iodine heavy-ion charge distribution rather than the one assuming three additional charged hydrogen fragments.

4.5.2 Kinetic Energies of Ions

Similar to the methylselenol molecule, discussed in section 4.2, methyl iodide is also composed of atoms with three very different masses. In this case, the ratio in mass between I:C:H is about 127:12:1, so differences are even more pronounced than for methylselenol.

The kinetic energy distribution of iodine and carbon ions for an exemplary set of heavy-ion charge state channels are shown in figure 4.26(a) and figure 4.26(b),

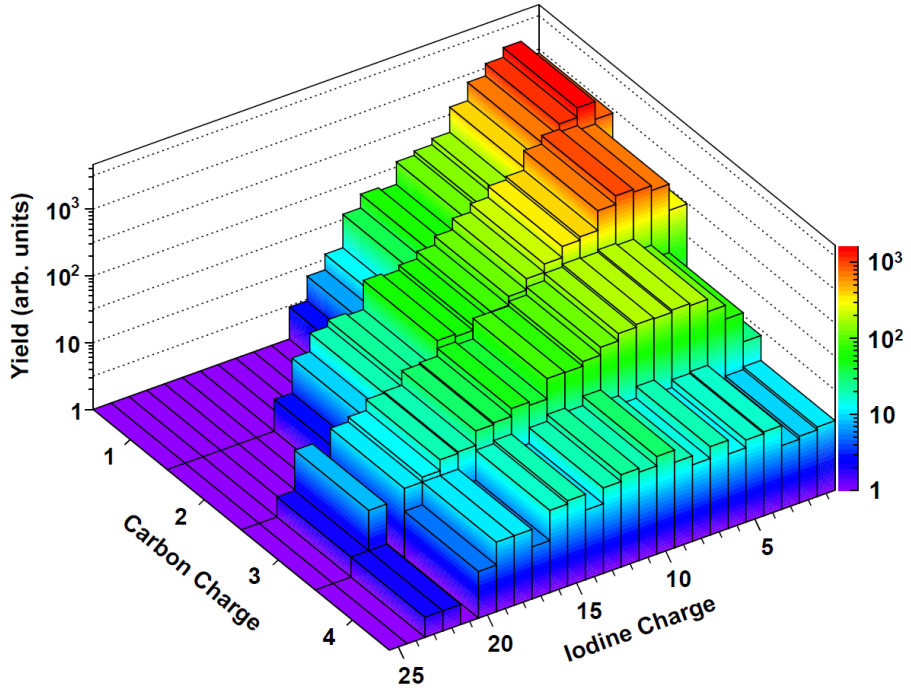

Figure 4.24: Yield of heavy-ion-fragment coincident channels for methyl iodide as a function of charge states at $\hbar\omega = 1500\,\text{eV}$, 100 fs pulse length and 0.7 mJ average pulse energy.

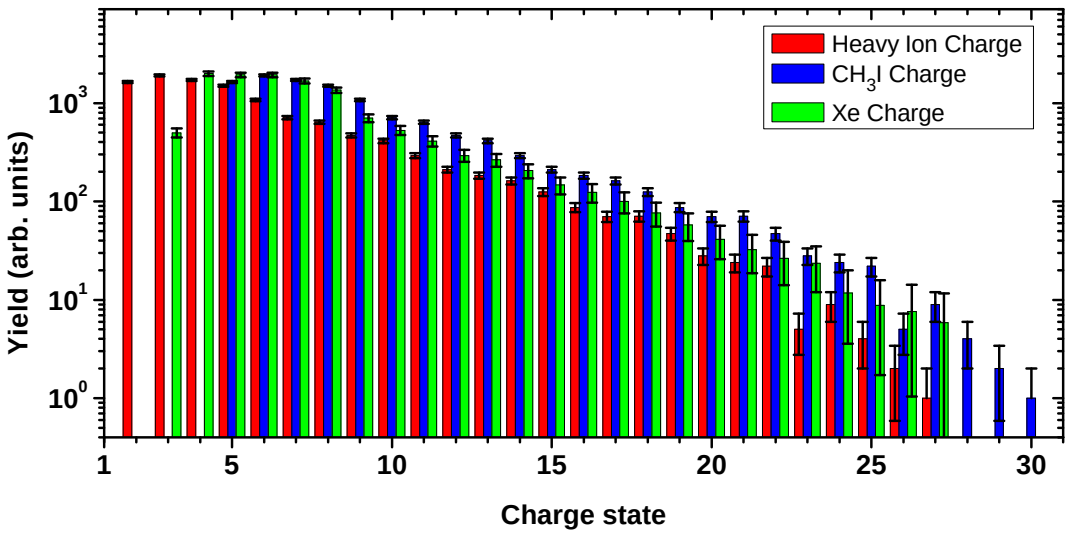

Figure 4.25: Abundances of heavy-ion and total molecular charge for methyl iodide at $\hbar\omega = 1500\,\text{eV}$, 100 fs pulse length and 0.7 mJ average pulse energy compared to the abundance of atomic xenon under the same experimental conditions.

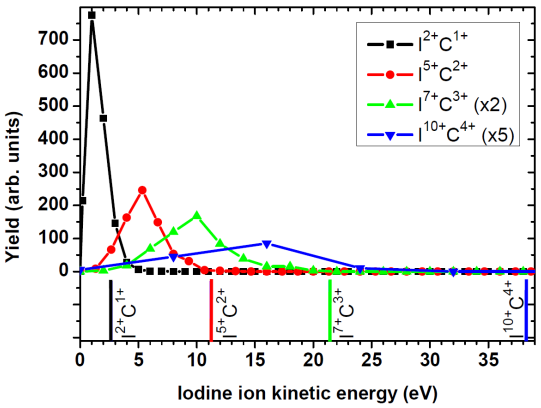

(a) Methyl iodide: Iodine KEDs

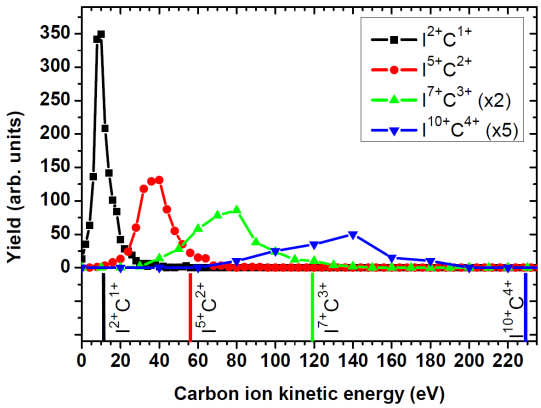

(b) Methyl iodide: Carbon KEDs

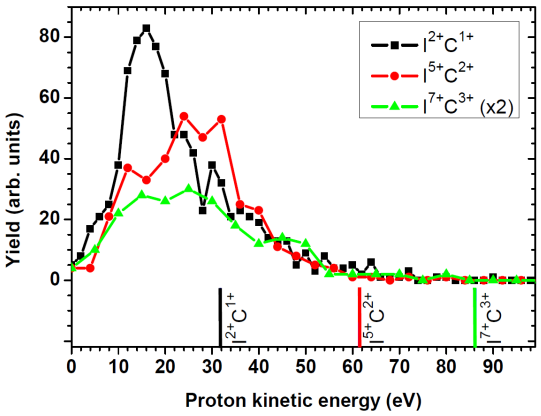

(c) Methyl iodide: Proton KEDs

Figure 4.26: Kinetic energy distributions of iodine (a), carbon (b), and hydrogen (c) ions for a representative set of final charge-state channels. Kinetic energies produced by the Coulomb explosion simulation are shown as vertical lines of the same color with respective channel names next to them. Note that the yield of some channels was multiplied by a factor (as indicated in the legend) for better visibility.

respectively. For the lowest shown charge state, i.e. $I^{2+}C^{1+}$, the simulated energy, indicated by the vertical lines of the same color with the channel name next to it, fits well to the maximum of the measured KED. Similar to the afore-discussed molecules, for higher charge states the simulation increasingly overestimates the measured kinetic energies. The simulated energies for I and C ions for the higher charged channels, shown in figures 4.26(a) and 4.26(b), are actually at the end of the high-energy tail of the measured KEDs. This discrepancy between the Coulomb model and the measurement is more severe than observed for the case of methylselenol in chapter 4.2 and is a consequence of the longer pulse duration of 100 fs, which increases the possible delay between the absorption of individual photons.

Looking at the measured KEDs for the protons for the same channels, shown in figure 4.26(c), it can be seen that the differences in the KEDs of the individual channels are subtle. For all depicted channels, even for the lowest charge state of $I^{2+}C^{1+}$, the measured kinetic energies are substantially lower than the simulated ones. However, in the $I^{2+}C^{1+}$ channel, there is a small peak at the high-energy end of the KED that is in good agreement with the simulation, suggesting that these protons come from a fast de-excitation pathway, that outruns any significant nuclear motion.

The sum kinetic energy distributions of the heavy ionic fragments, iodine and carbon, are shown in figure 4.27 as a function of the product of their charge states. Considering a diatomic complex I−C, and neglecting the hydrogens, the final kinetic energy can be estimated from the initial potential energy of the system at the equilibrium internuclear distance $R_0 = 2.14\,\text{Å}$ using equation 4.2. This is indicated by the red solid line in figure 4.27. It can be stated that this line is only in accordance with the sKEDs measured for the low charge states up to a product of 5. For higher charges, the sKEDs show a deviation towards lower energies that increases with a higher charge-state product. Here, the measured KED values can be reasonably approximated by the line corresponding to $R = 4\,\text{Å}$, which, gives an estimate for the lower limit of the stretching in the I−C bond.

For asymmetric channels, $q_C > q_I$, such as $I^{1+}C^{2+}$ and $I^{1+}C^{3+}$, the measured KEDs are significantly higher than expected by calculations assuming the measured final charge states and the equilibrium geometry of the methyl iodine molecule. This resembles the observations that were made for methyselenol for the same type of asymmetric channels in section 4.2.4.1.

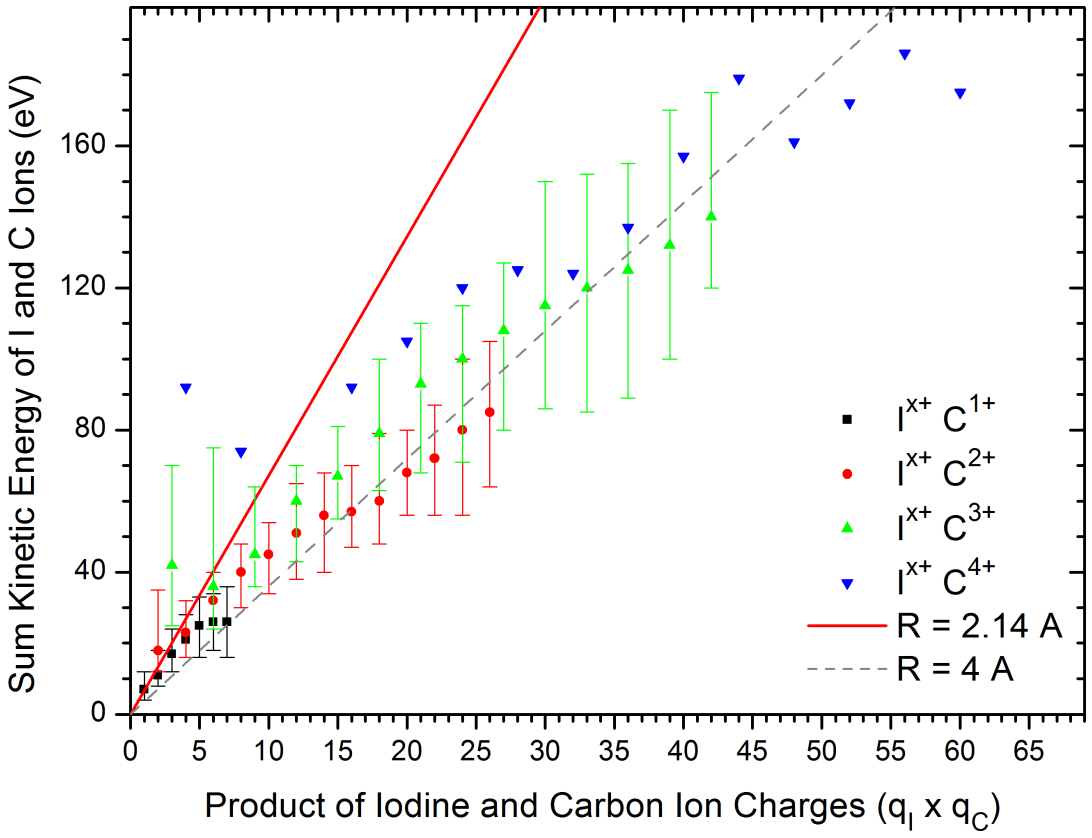

Figure 4.27: Summed kinetic energies of heavy-ion-fragment coincident channels as a function of charge-state product at $\hbar\omega = 1500\,\text{eV}$. $I^{X+}C^{4+}$ channels only show the mean of the sKED for the individual channels due to low statistics for those channels (see text).

Note that the $I^{X+}C^{4+}$ channels in figure 4.27 are represented differently than the other channels with lower carbon ion charge. The symbols represent the average of the sum kinetic energies measured for the respective channel, rather than the position of the maximum of the KED. The width of the distribution is not given, as it could not be reliably determined, because of a very broad spread in energy and low count rates for individual energy bins. The lower statistics of these channels prohibit a more detailed analysis that is employed for the other channels.

The anomalously high fragment energies for the channels where the predominantly absorbing heavy atom is charged less than the carbon fragment most likely result from the same charge redistribution process that was discussed for methylselenol in section 4.2.4.1. The I−C complex is initially charged higher than indicated by its final charge states, resulting in a Coulomb explosion at small R producing high fragment energies, and, subsequently sharing the charge with the neighboring

protons. This assumption is further supported by the fact that the sum energy of I and C fragments measured for the $I^{1+}C^{4+}$ channel is very close to the value observed for the $I^{4+}C^{4+}$ final state, i.e., the one which differs in charge by the number of hydrogen constituents in the methyl iodide molecule. Note that a similar trend can be also observed in figure 4.10 for methylselenol, where the sum energy for $Se^{1+}C^{3+}$ resembles the value of the $Se^{5+}C^{3+}$ channel. Finally, this hypothesis can be verified using the data presented in figure 4.23 for the ICl molecule, which does not contain H constituents. There, all measured kinetic energies lie on or well below the line corresponding to the CE at the equilibrium distance of the neutral molecule.

Chapter 5

Conclusions and Outlook

Within this thesis, the dynamics of multiple ionization and fragmentation of several small molecules containing single high-Z atoms, namely selenium or iodine, induced by intense X-ray FEL pulses has been investigated in detail by employing coincident ion momentum spectroscopy. Pulse intensities ranging up to $3.5 \cdot 10^{17}$ W cm^{-2}, significantly larger than in previous studies at synchrotrons, resulting in considerable contributions of multi-photon absorption within one pulse, never investigated in a coincident fragment measurement before. This work aimed at bridging the gap between experiments on isolated atoms and extended polyatomic systems, such as clusters and biomolecules, by understanding the role of the environment in multiple inner-shell ionization and unveiling accompanying charge redistribution processes. Such processes are expected to be of considerable importance for imaging of biological samples, nanocrystals or individual viruses, since the sample might suffer significant damage, localized around specific sites containing high-Z elements, that cannot be accounted for by scaling factors [20]. Moreover, this study should answer the question, whether a shot-to-shot orientation of (large) molecules by inspecting the momentum vectors of (fast) protons being emitted along the bond direction with a neighboring heavy-ion that might be attached at the rim of a large biomolecules. If so, the method would have significant potential impact on FEL-based imaging of biological samples.

The molecules selected for this work, methylselenol, ethylselenol, iodine chloride and methyl iodide, represent insightful prototype systems for addressing these issues. The large absorption cross section of the heavy atom constituent enhances the overall ionization level, and localizes the initial photoabsorption, enabling the investigation

of subsequent charge rearrangement phenomena under well-defined initial conditions. Moreover, the data can be directly compared with the results on the isolated atomic counterparts with similar electronic structure, i.e. krypton and xenon atoms for selenium- and iodine-containing molecules, respectively.

The coincident 3D ion momentum studies on small molecules (CH_3SeH, CH_3I, ICl) show that the total charge produced in such molecular systems is very close to the charge created in an isolated atom with similar number of electrons and absorption cross sections as the heavier constituent in the molecule, although the individual charge states observed for the heavy atom embedded in a molecular environment are significantly lower than for the case of an isolated atom. This indicates that efficient (and fast) electron rearrangement mechanisms are at work in polyatomic systems. Very high levels of ionization are found for iodine-containing molecules at 1.5 keV, e.g. the ICl molecules looses nearly half of its initial 70 electrons. This suggests that the mechanism of resonantly-enhanced X-ray ionization (REXMI) discovered in [24, 121] for Xe atoms does also significantly enhance ionization for iodine in the molecular environment. This is further substantiated by a lower degree of ionization observed at 2 keV photon energy, where lower cross sections do not allow for reaching the charge states at which REXMI pathways starting from the M-shell are energetically possible for present pulse intensities.

For the larger molecule C_2H_5SeH, the charge-state distribution is shifted to higher values compared to its atomic counterpart, krypton, although a larger uncertainty in the exact final charge state of the molecule and a difference in photon energy (1.7 keV vs. 2 keV for krypton) prevent an exact quantitative comparison. The reason for the observed discrepancy most likely results from the larger total number of electrons available to participate in the Auger cascades and shake-off processes in ethylselenol as well as from the existence of an additional carbon atom in the molecule.

Further information on the ionization and fragmentation dynamics could be obtained from the kinetic energies of the fragments measured for each final charge state of the molecule and from their comparison with the outcome of a Coulomb explosion model which assumes instantaneous removal of all ionized electrons and subsequent Coulomb explosion at the equilibrium geometry of the neutral molecule. In addition, the number of X-ray photons involved in the ionization processes for a given channel could be deduced from the measured intensity dependence of the corresponding

ion yield in the case of methylselenol. For channels produced by single-photon absorption, the measured kinetic energies of the carbon, selenium, iodine and chlorine fragments are in good agreement with the simulated values, suggesting that there is no significant motion of the (heavy) nuclei on the time scale of the first Auger steps (typically sub-fs for Se and I atoms at keV photon energies). However, for higher charge states which are reached after absorption of two or more photons, the measured kinetic energies are significantly lower than the simulated ones. This can be understood by considering the following sequence of events: The first photoionization and subsequent Auger decays trigger an elongation of the bonds or the dissociation of the molecule, and, as a result the internuclear distance begins to grow. As the charge state is further increased by slower Auger decays, and possibly, by the absorption of a second (3rd, 4th,...) X-ray photon, the internuclear distance has already increased, and ionic fragments reach their final charge states at internuclear distances considerably higher than those in the equilibrium geometry of the molecule. As a consequence, the Coulomb repulsion force is much less than for the case of the same charge states reached at the equilibrium distance, resulting in final kinetic energies of the fragments that are (significantly) lower than expected for vertical ionization at the equilibrium geometry. The estimated lower limit for the stretching of the bond lengths ranges from $\sim 3\,\text{Å}$ in methylselenol with nominally 5 fs pulses to $\sim 4\,\text{Å}$ in methyl iodide with nominally 80 fs pulses.

In contrast to the heavier ions, the lightest ionic fragments – protons – appear to be considerably displaced even within the very short time of the FEL pulse (in 1 fs, a proton with one atomic unit of energy (27.2 eV) moves about 3.5 Å, i.e. more than a bond length). Therefore, the measured protons never exhibit the simulated CE energies corresponding to the equilibrium internuclear distances. The broad kinetic energy distributions for protons point towards the co-existence of pathways where the protons leave the system at a very early stage of ionization, and of those where the protons "see" a significant portion of the final molecular charge at small internuclear distances, resulting in a high-energy tail in their kinetic energy distribution. Although for most of the cases, the assumption of instantaneous multi-electron removal and Coulomb explosion at the equilibrium internuclear distance typically yields the upper limit for the measured kinetic energies of the fragments, this is not the case for channels where carbon atoms are charged higher than selenium or iodine atoms (observed in methylselenol and methyl iodide, respectively). These channels,

whose charge distribution represents an indication for charge redistribution within the molecular systems, exhibit broad kinetic energy distributions with their maxima well beyond the predictions of the Coulomb explosion model. These anomalously high kinetic energies exceeding the values expected for Coulomb explosion at equilibrium distances might be explained by a shortening of the bonds prior to dissociation. A more likely interpretation, however, is that for these channels, the heavy atoms in the molecule are initially charged significantly higher than the final-state sum charge of the two heavy fragments, and that the excess charge is transferred to the protons only after the heavy fragments have reached high kinetic energies. This hypothesis is further corroborated by the fact that this effects is not present in the diatomic ICl molecule, which does not contain protons.

Finally, this work demonstrated that coincident CE imaging can provide useful information about the spatial orientation of the molecule even for the case of sequential few-photon induced fragmentation. This has been proven by revealing three-particle angular correlation in the fragmentation of methylselenol and ethylselenol. For the larger molecule, the carbon fragment initially located next to the selenium atom could be identified for some channels, while for methylselenol, the protons originating from the selenium and carbon sites could be distinguished. The angular distribution of the protons is rather broad, whereas the selenium and carbon atoms are essentially emitted back to back, and exhibit angular correlations which become sharper with increasing charge states.

The results described above have direct implications for coherent diffractive imaging. The comparison between measured kinetic energies of the fragments with the Coulomb explosion model yields a direct estimate of the atomic displacement on the time scale of the ionization processes, thus, defining the extent of radiation-induced damage on the atomic length scale. The results clearly indicate that all imaging schemes aimed to "outrun" damage effects require ultrashort pulses of only a few femtoseconds duration, and that local "hot spots" of increased radiation damage in the vicinity of high-Z atoms (e.g., iron or sulfur constituents in some biological systems) have to be taken into account for the interpretation of corresponding imaging data. Although the idea to retrieve orientation of larger, nanoscale systems from the emission angles of the fast protons [139] seems to be, to a large extent, unfeasible because of the ultrafast charge redistribution observed, the ion angular patterns of the heavier fragments can be exploited to determine the molecular orientation for

further applications, e.g., photoelectron spectroscopy in the molecular frame.

The techniques of coincident ion momentum imaging spectroscopy, described in this work, as well as the related ion-electron coincidence spectroscopy, which enables measurements in the molecular frame, were initially developed at ion-accelerator and synchrotron facilities operating at megahertz repetition rates. This allows to collect significant statistics on processes with low cross sections in a reasonable time window. In contrast, at today's X-FELs such as the LCLS operating at 120 Hz repetition rate, the accumulation of significant statistics for the class of coincidence experiments presented in this work is a challenging task given the fact that beamtime at these facilities is limited and highly competitive. As a result, taking multi-particle coincidence data sets for a larger variety of FEL parameters such as different photon energies or pulse lengths is extremely challenging.

However, this will change dramatically with the advent of new XFELs such as the European X-FEL in Hamburg, where the FEL design is based on superconducting accelerator technology and will offer repetition rates of up to 27 kHz. This will open up completely new dimensions for the techniques described in this work, enabling, in particular, photoelectron diffraction, holography, or fluorescence experiments on molecules "fixed in space" by coincident angle-resolved detection of emitted ionic fragments.

New ways to control the pulse length of the electron bunch and, consequently, the length of the photon pulse were developed [111] and recently successfully tested in rare-gas cluster experiments [28], allowing the study of the ionization processes described in this work as a function of pulse length. Thus, radiation damage mechanisms can be further investigated in view of the question of how short the pulse has to be in order to fulfill the requirements for the successful realization of the "diffract before destroy" approach [12].

On the other hand, recent improvements on the timing control between an optical (IR) laser and the FEL pulse at the LCLS AMO beamline [147] now allow to perform detailed studies of time-dependent processes on a sub 100 fs timescale. This capability can be efficiently used for a variety of time-resolved laser pump – X-ray probe techniques [85]. In particular, in the light of this work, this enables the study of molecules that undergo dynamics triggered by the IR laser (so-called pump pulse) using the FEL pulses as a probe. With respect to the results on charge transfer presented in this work, the dissociation of the molecule, that is triggered by

the IR laser can be seen as a transition from an intact molecule towards two separate atoms. A proof-of-principles experiment of this kind was recently performed using the setup described in this work with only minor changes to include the pump laser. Here, methyliodide was first dissociated using the AMO IR laser, and after a certain time delay t interacted with the FEL. Investigating the kinetic energies of the molecular fragments as a function of the delay between the IR and the FEL pulses, the dynamics of the dissociation triggered by the IR pulse can be mapped.

This is illustrated in figure 5.1, where part of the time-of-flight spectrum, resulting from the LCLS-induced fragmentation of the CH_3I molecule dissociated by an 800 nm IR laser pulse is shown as a function of IR/X-ray pump-probe delay. Here, each of the ionic species results in a group of lines symmetric with respect to the TOF of the ion with zero momentum along the TOF axis due to the ions initially flying towards or away from the detector. Delay-dependent structures indicated by the arrows reflect the decreasing kinetic energy of the fragments with increasing internuclear distance (in the case of figure 5.1, the distance between the iodine atom and the methyl group) as the molecule dissociates over two pathways with different dissociation energies. For each dissociation channel, the measured kinetic energy of the fragments can be recalculated into the internuclear distance using the Coulomb law. Using this approach, the key processes studied in this work can be investigated as a function of the internuclear distance. This will enable an unambiguous determination of the role of molecular partners in the X-ray ionization, and disentangle the contributions from intra- and interatomic electronic relaxation channels. As a next step in the same direction, Auger electron energies from the dissociating molecules can be measured as a function of the internuclear distance, resolving a long-standing discussion of "atomic" and "molecular" contributions in molecular Auger spectra [148].

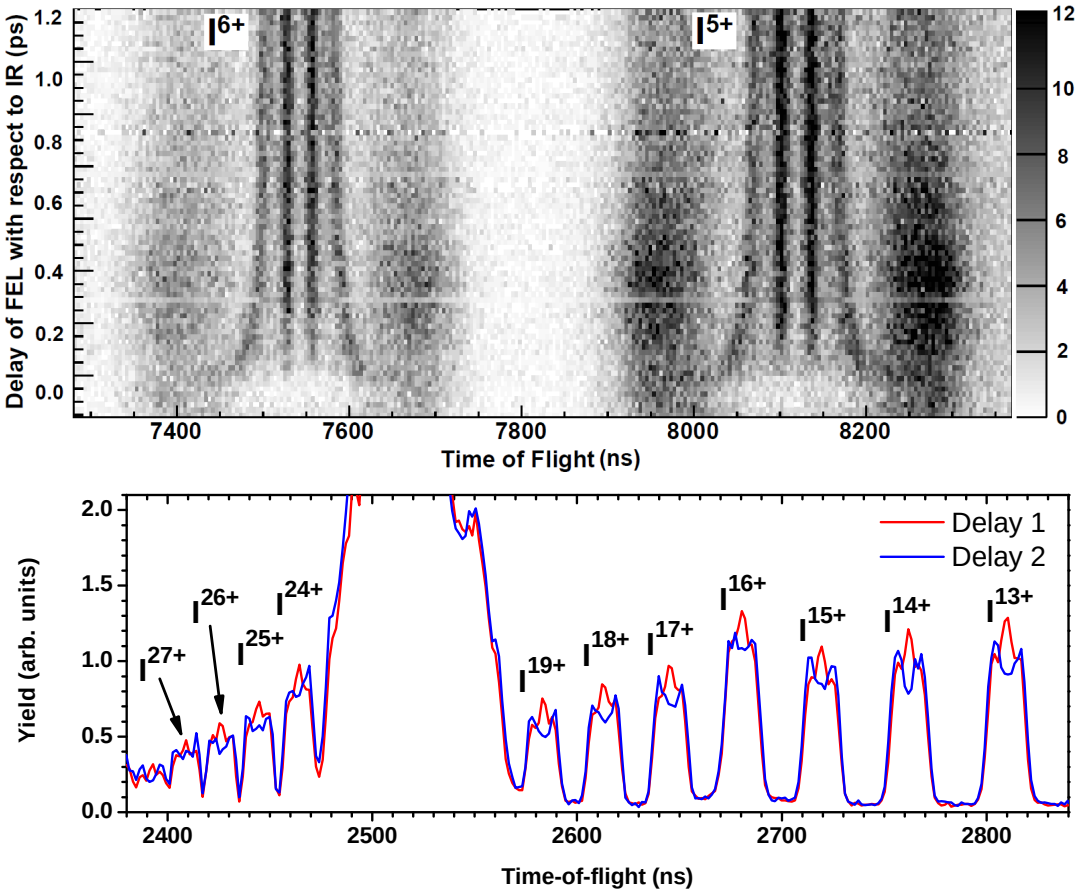

Figure 5.1: (a) Time-of-flight spectrum of I^{5+} and I^{6+} ions resulting from the LCLS-induced fragmentation of CH_3I molecules dissociated by an 800 nm IR laser pulse, shown as a function of IR/ X-ray pump-probe delay. (b) Time-of-flight spectrum for two respective delays between the IR pump pulse and the 1500 eV X-ray probe pulse. The red curve shows the spectrum where the IR pulse arrives 1 ps before the FEL pulse; the blue curve shows the spectrum where the IR pulse arrives 0.1 ps before the FEL pulse. The change of the shape of the TOF peaks reflects large internuclear distance and, thus, decreased Coulomb explosion energy at large IR/X-ray delays.

Appendix A

More Experiment Parameters

Overview of General LCLS Parameters

Gain length:	3.5 m for hard X-rays 1.5 Å 1.6 m for soft X-rays 15 Å
Saturation length:	60 m for 1.5 Å
Length of total undulator system:	132 m (with 3.4 m single undulator length)
Undulator period:	$\lambda_U = 3\,\mathrm{cm}$
Undulator gap height:	6.8 mm
Deflection Parameter:	$K = 3.5$
Undulator magnetic field:	$B_0 = 1.5\,\mathrm{T}$

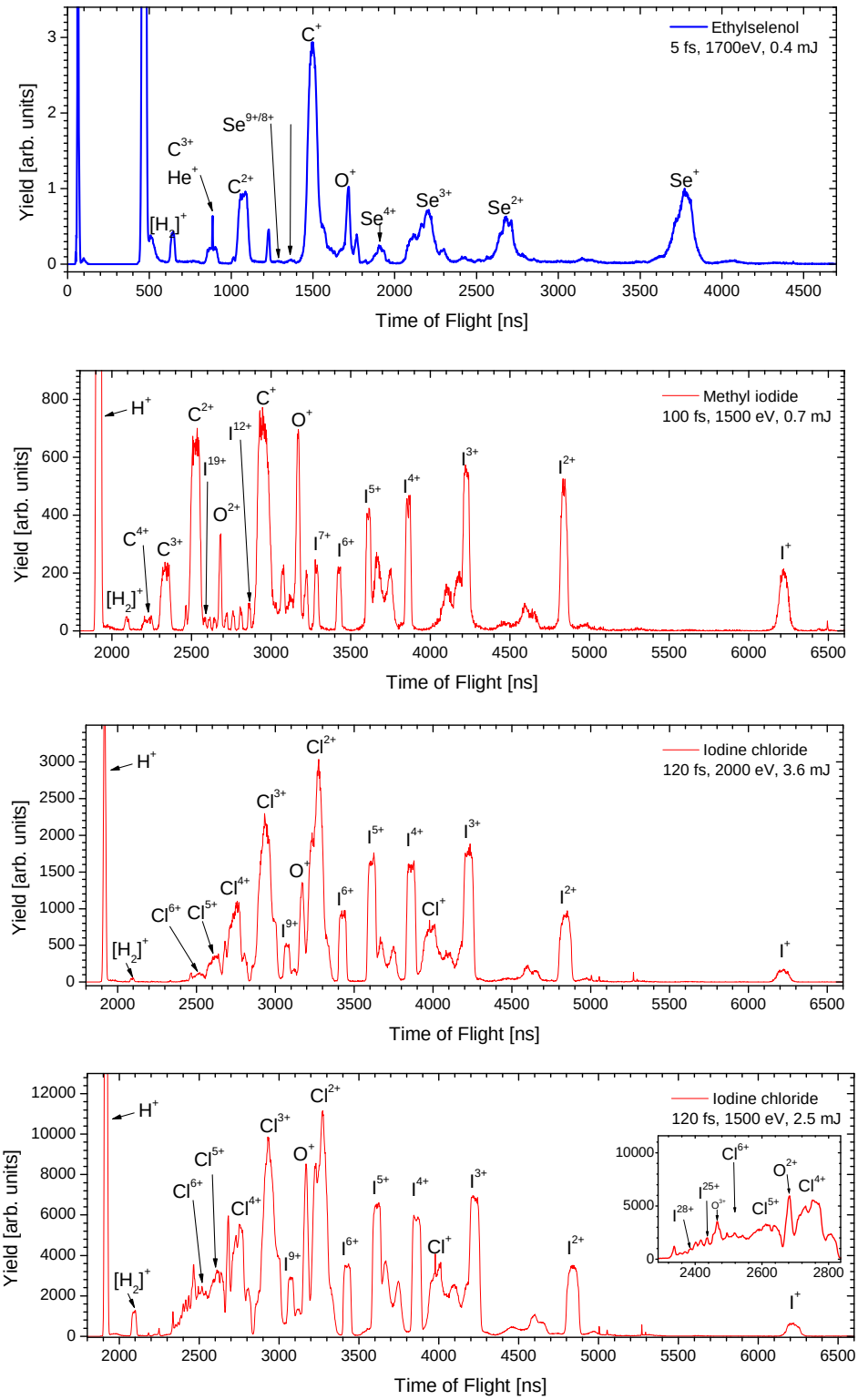

Figure A.1: Time-of-flight spectra measured with FEL parameters as indicated in the legends.

Appendix B

Coulomb Explosion Simulations

Fragmentation Channel	Simulated Energy	Proton next neighbor
$Se^+ + H^+$	9.7 eV	Se
$Se^{2+} + H^+$	19.3 eV	Se
$Se^+ + C^+ + H^+$	14.4 eV	Se
$Se^+ + C^+ + H^+$	18.1 eV	C
$Se^{2+} + C^+ + H^+$	24.1 eV	Se
$Se^{2+} + C^+ + H^+$	23.9 eV	C
$Se^{2+} + C^{2+} + H^+$	28.5 eV	Se
$Se^{2+} + C^{2+} + H^+$	36.5 eV	C
$Se^{3+} + C^+ + H^+$	33.9 eV	Se
$Se^{3+} + C^+ + H^+$	29.7 eV	C
$Se^{3+} + C^{2+} + H^+$	38.2 eV	Se
$Se^{3+} + C^{2+} + H^+$	42.4 eV	C

Table B.1: Table of charge state configurations and their respective simulated proton energies. Note that for these calculations only the fragments listed in the left of the table were considered and the rest of the atoms remained neutral.

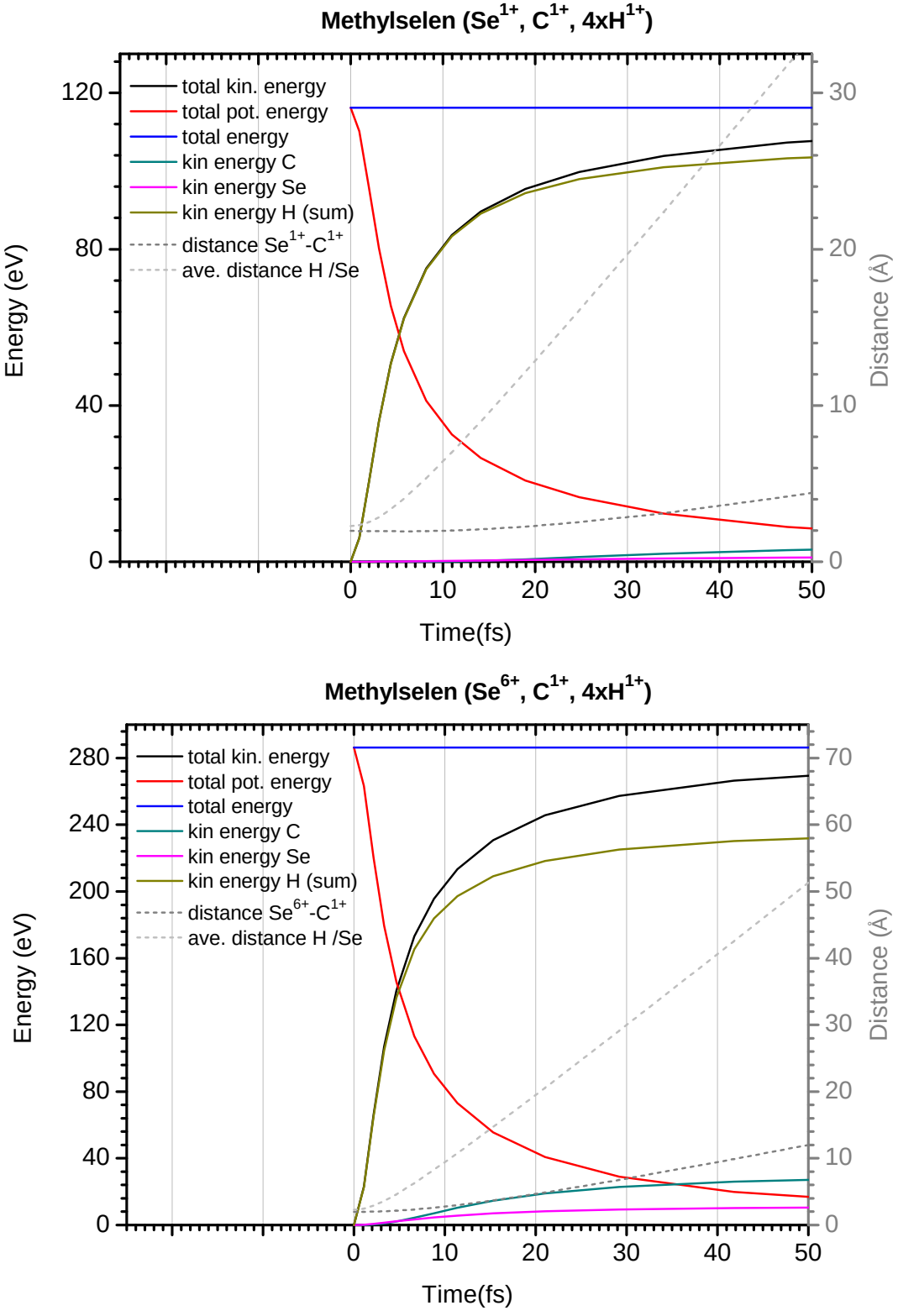

Figure B.1: Simulated time dependence of kinetic energies and internuclear distances for two Se-C charge states. Charges of ions are indicated above the figures and the equilibrium geometry of the molecule is used.

Appendix C

Momentum Sums

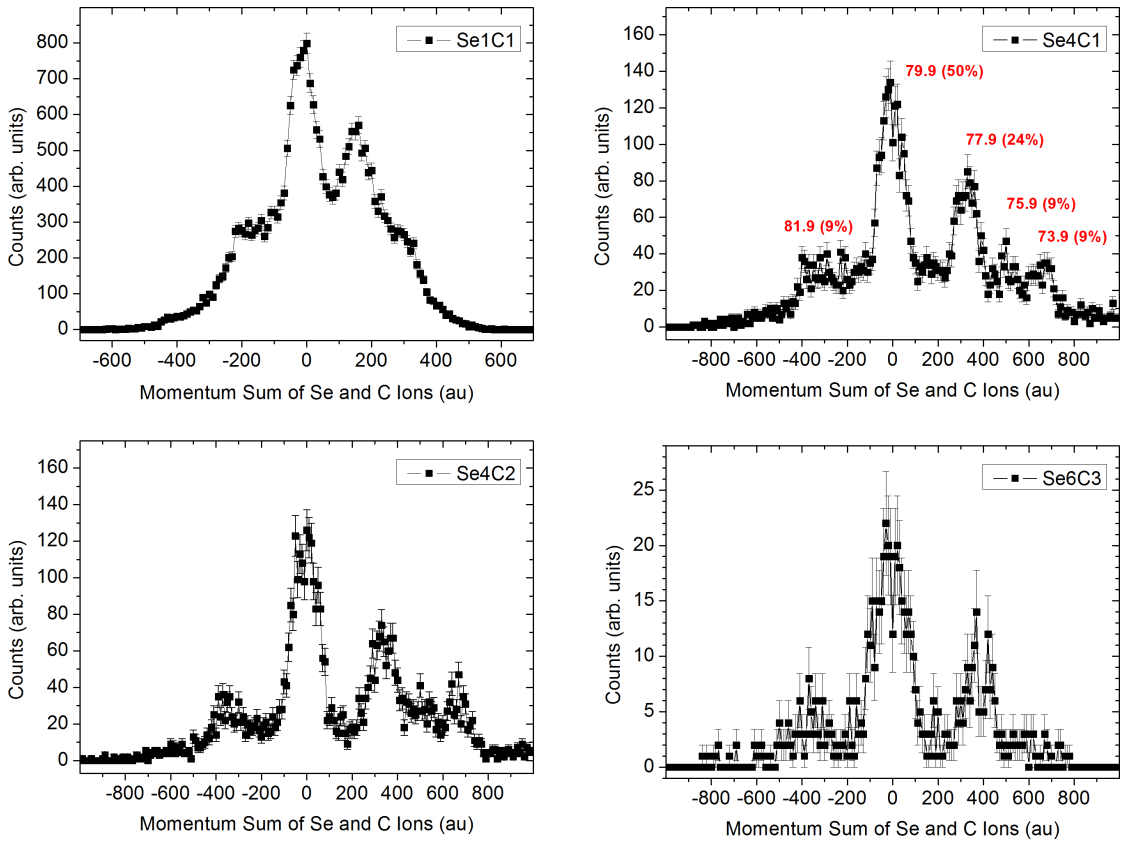

Figure C.1: Sum of selenium and carbon ion momenta in the Z-component, along the spectrometer axis (time of flight axis) for 4 different channels. The momentum-sum distribution shows 5 peaks corresponding to the 5 (most abundant) isotopes of selenium.

Bibliography

[1] Röntgen, W. C. Ueber eine neue Art von Strahlen. *Annalen der Physik* **300**, 12–17 (1898). URL http://dx.doi.org/10.1002/andp.18983000103.

[2] Mould, R. F. The early history of X-ray diagnosis with emphasis on the contributions of physics 1895-1915. *Physics in Medicine and Biology* **40**, 1741 (1995). URL http://stacks.iop.org/0031-9155/40/i=11/a=001.

[3] Friedrich, W., Knipping, P. & Laue, M. Interferenzerscheinungen bei Röntgenstrahlen. *Annalen der Physik* **346**, 971–988 (1913). URL http://dx.doi.org/10.1002/andp.19133461004.

[4] Debye, P. & Scherrer, P. Interferenzen an regellos orientierten Teilchen im Röntgenlicht. *Physikalische Zeitschrift* **17**, 277 (1916). URL http://gdz.sub.uni-goettingen.de/index.php?id=resolveppn&PPN=GDZPPN002504294.

[5] Watson, J. D. & Crick, F. H. Molecular structure of nucleic acids; a structure for deoxyribose nucleic acid. *Nature* **171**, 737–738 (1953). URL http://www.nature.com/nature/dna50/watsoncrick.pdf.

[6] Wikipedia. Electromagnetic spectrum — Wikipedia, The Free Encyclopedia (2012). URL http://en.wikipedia.org/wiki/Electromagnetic_spectrum. [Online; accessed 18-October-2012].

[7] Ament, L. J. P., van Veenendaal, M., Devereaux, T. P., Hill, J. P. & van den Brink, J. Resonant inelastic x-ray scattering studies of elementary excitations. *Rev. Mod. Phys.* **83**, 705–767 (2011). URL http://link.aps.org/doi/10.1103/RevModPhys.83.705.

[8] Rehr, J. J. & Albers, R. C. Theoretical approaches to x-ray absorption fine structure. *Rev. Mod. Phys.* **72**, 621–654 (2000). URL `http://link.aps.org/doi/10.1103/RevModPhys.72.621`.

[9] de Groot, F. High-Resolution X-ray Emission and X-ray Absorption Spectroscopy. *Chemical Reviews* **101**, 1779–1808 (2001). URL `http://pubs.acs.org/doi/abs/10.1021/cr9900681`.

[10] Siegbahn, K. Electron spectroscopy for atoms, molecules, and condensed matter. *Rev. Mod. Phys.* **54**, 709–728 (1982). URL `http://link.aps.org/doi/10.1103/RevModPhys.54.709`.

[11] Elder, F. R., Gurewitsch, A. M., Langmuir, R. V. & Pollock, H. C. Radiation from electrons in a synchrotron. *Phys. Rev.* **71**, 829–830 (1947). URL `http://link.aps.org/doi/10.1103/PhysRev.71.829.5`.

[12] Neutze, R., Wouts, R., van der Spoel, D., Weckert, E. & Hajdu, J. Potential for biomolecular imaging with femtosecond X-ray pulses. *Nature* **406**, 752–757 (2000). URL `http://dx.doi.org/10.1038/35021099`.

[13] Hau-Riege, S. P., London, R. A. & Szoke, A. Dynamics of biological molecules irradiated by short x-ray pulses. *Phys. Rev. E* **69**, 051906 (2004). URL `http://link.aps.org/doi/10.1103/PhysRevE.69.051906`.

[14] Seibert, M. M. *et al.* Single mimivirus particles intercepted and imaged with an X-ray laser. *Nature* **470**, 78–81 (2011). URL `http://www.nature.com/doifinder/10.1038/nature09748`.

[15] Gorkhover, T. *et al.* Nanoplasma Dynamics of Single Large Xenon Clusters Irradiated with Superintense X-Ray Pulses from the Linac Coherent Light Source Free-Electron Laser. *Phys. Rev. Lett.* **108**, 245005 (2012). URL `http://link.aps.org/doi/10.1103/PhysRevLett.108.245005`.

[16] Loh, N. D. *et al.* Fractal morphology, imaging and mass spectrometry of single aerosol particles in flight. *Nature* **486**, 513–517 (2012). URL `http://dx.doi.org/10.1038/nature11222`.

[17] Kassemeyer, S. *et al.* Femtosecond free-electron laser x-ray diffraction data sets for algorithm development. *Opt. Express* **20**, 4149–4158 (2012). URL http://www.opticsexpress.org/abstract.cfm?URI=oe-20-4-4149.

[18] Chapman, H. N. *et al.* Femtosecond X-ray protein nanocrystallography. *Nature* **470**, 73–77 (2011). URL http://www.nature.com/doifinder/10.1038/nature09750.

[19] Barty, A. *et al.* Self-terminating diffraction gates femtosecond X-ray nanocrystallography measurements. *Nature Photonics* **6**, 35 – 40 (2012). URL http://dx.doi.org/10.1038/nphoton.2011.297.

[20] Lomb, L. *et al.* Radiation damage in protein serial femtosecond crystallography using an x-ray free-electron laser. *Phys. Rev. B* **84**, 214111 (2011). URL http://link.aps.org/doi/10.1103/PhysRevB.84.214111.

[21] Barty, A. *et al.* Predicting the coherent X-ray wavefront focal properties at the Linac Coherent Light Source (LCLS) X-ray free electron laser. *Opt. Express* **17**, 15508–15519 (2009). URL http://www.opticsexpress.org/abstract.cfm?URI=oe-17-18-15508.

[22] Young, L. *et al.* Femtosecond electronic response of atoms to ultra-intense X-rays. *Nature* **466**, 56–61 (2010). URL http://dx.doi.org/10.1038/nature09177.

[23] Doumy, G. *et al.* Nonlinear Atomic Response to Intense Ultrashort X Rays. *Phys. Rev. Lett.* **106**, 083002 (2011). URL http://link.aps.org/doi/10.1103/PhysRevLett.106.083002.

[24] Rudek, B. *et al.* Ultra-Efficient Ionization of Heavy Atoms by Intense X-Ray Free-Electron Laser Pulses. *Nature Photonics* (2012). URL http://dx.doi.org/10.1038/nphoton.2012.261.

[25] Hoener, M. *et al.* Ultraintense X-Ray Induced Ionization, Dissociation, and Frustrated Absorption in Molecular Nitrogen. *Phys. Rev. Lett.* **104**, 253002 (2010). URL http://link.aps.org/doi/10.1103/PhysRevLett.104.253002.

[26] Cryan, J. P. *et al.* Auger Electron Angular Distribution of Double Core-Hole States in the Molecular Reference Frame. *Phys. Rev. Lett.* **105**, 083004 (2010). URL http://link.aps.org/doi/10.1103/PhysRevLett.105.083004.

[27] Berrah, N. *et al.* Double-core-hole spectroscopy for chemical analysis with an intense X-ray femtosecond laser. *Proceedings of the National Academy of Sciences* **108**, 16912–16915 (2011). URL http://www.pnas.org/content/108/41/16912.abstract.

[28] Schorb, S. *et al.* Size-Dependent Ultrafast Ionization Dynamics of Nanoscale Samples in Intense Femtosecond X-Ray Free-Electron-Laser Pulses. *Phys. Rev. Lett.* **108**, 233401 (2012). URL http://link.aps.org/doi/10.1103/PhysRevLett.108.233401.

[29] Göppert-Mayer, M. Über Elementarakte mit zwei Quantensprüngen. *Annalen der Physik* **401**, 273–294 (1931). URL http://dx.doi.org/10.1002/andp.19314010303.

[30] Voronov, G. S. & Delone, N. B. Ionization of the xenon atom by the electric field of ruby laser emission. *Journal of Experimental and Theoretical Physics (JETP) Letters* **1**, 66–68 (1965).

[31] Jurek, Z. & Faigel, G. The effect of inhomogenities on single-molecule imaging by hard XFEL pulses. *EPL (Europhysics Letters)* **86**, 68003 (2009). URL http://stacks.iop.org/0295-5075/86/i=6/a=68003.

[32] Schrödinger, E. Quantisierung als Eigenwertproblem. *Annalen der Physik* **385**, 437–490 (1926). URL http://dx.doi.org/10.1002/andp.19263851302.

[33] Simon, M. C. *et al.* Resonant and Near-Threshold Photoionization Cross Sections of Fe^{14+}. *Phys. Rev. Lett.* **105**, 183001 (2010). URL http://link.aps.org/doi/10.1103/PhysRevLett.105.183001.

[34] Hartree, D. R. The Wave Mechanics of an Atom with a Non-Coulomb Central Field. Part I. Theory and Methods. *Mathematical Proceedings of the Cambridge Philosophical Society* **24**, 89–110 (1928). URL http://dx.doi.org/10.1017/S0305004100011919.

[35] Amusia, M. Y. *VUV and Soft X-Ray Photoionization (Chapter 1)* (Springer, 1996), 1. edn.

[36] Stöhr, J. *NEXAFS Spectroscopy (Chapter 2)*, vol. 1 (Springer, 1992).

[37] Berger, M. *et al.* XCOM: Photon Cross Sections Database (1998). URL `http://www.nist.gov/pml/data/xcom/index.cfm`.

[38] Teo, B. *EXAFS: basic principles and data analysis*. Inorganic chemistry concepts (Springer-Verlag, 1986).

[39] Demtröder, W. *Experimentalphysik 3 (Chapter 7)* (Springer, 2005), 3 edn.

[40] Mehlhorn, W. Atomic Auger spectroscopy: Historical perspective and recent highlights. *AIP Conference Proceedings* **506**, 33–56 (2000). URL `http://link.aip.org/link/?APC/506/33/1`.

[41] Wentzel, G. Über strahlungslose Quantensprünge. *Zeitschrift für Physik* **43**, 524–530 (1927). URL `http://www.springerlink.com/content/r314483276n54207/`.

[42] Thompson, A. C. (ed.) *X-ray Data Booklet* (Lawrence Berkeley National Laboratory, University of California, 2009), third edn.

[43] Saito, N. & Suzuki, I. H. Shake-off processes in photoionization and Auger transition for rare gases irradiated by soft X-rays. *Physica Scripta* **49**, 80 (1994). URL `http://stacks.iop.org/1402-4896/49/i=1/a=011`.

[44] Kochur, A. G. & Popov, V. A. Shake up and shake off probabilities for L-, M-, and N-electrons in atoms with $Z = 3$ to 60. *Radiation Physics and Chemistry* **75**, 1525 – 1528 (2006). URL `http://www.sciencedirect.com/science/article/pii/S0969806X06002118`.

[45] Armen, G. B., Aksela, H., Aberg, T. & Aksela, S. The resonant Auger effect. *Journal of Physics B: Atomic, Molecular and Optical Physics* **33**, R49 (2000). URL `http://stacks.iop.org/0953-4075/33/i=2/a=201`.

[46] Carlson, T. A. & Krause, M. O. Atomic Readjustment to Vacancies in the K and L Shells of Argon. *Phys. Rev.* **137**, A1655–A1662 (1965). URL `http://link.aps.org/doi/10.1103/PhysRev.137.A1655`.

[47] Levin, J. C. *et al.* Argon-photoion–Auger-electron coincidence measurements following K-shell excitation by synchrotron radiation. *Phys. Rev. Lett.* **65**, 988–991 (1990). URL http://link.aps.org/doi/10.1103/PhysRevLett.65.988.

[48] Popov, V. S. Tunnel and multiphoton ionization of atoms and ions in a strong laser field (Keldysh theory). *Physics-Uspekhi* **47**, 855 (2004). URL http://stacks.iop.org/1063-7869/47/i=9/a=R01.

[49] Rohringer, N. & Santra, R. X-ray nonlinear optical processes using a self-amplified spontaneous emission free-electron laser. *Phys. Rev. A* **76**, 033416 (2007). URL http://link.aps.org/doi/10.1103/PhysRevA.76.033416.

[50] Sytcheva, A., Pabst, S., Son, S.-K. & Santra, R. Enhanced nonlinear response of Ne^{8+} to intense ultrafast x rays. *Phys. Rev. A* **85**, 023414 (2012). URL http://link.aps.org/doi/10.1103/PhysRevA.85.023414.

[51] Son, S.-K. & Santra, R. Monte Carlo calculation of ion, electron, and photon spectra of xenon atoms in x-ray free-electron laser pulses. *Phys. Rev. A* **85**, 063415 (2012). URL http://link.aps.org/doi/10.1103/PhysRevA.85.063415.

[52] Nenner, I. & Morin, P. *VUV and Soft X-Ray Photoionization (Chapter 9)* (Springer, 1996), 1. edn.

[53] Lennard-Jones, J. E. The electronic structure of some diatomic molecules. *Trans. Faraday Soc.* **25**, 668–686 (1929). URL http://dx.doi.org/10.1039/TF9292500668.

[54] Eberhardt, W. *et al.* Site-Specific Fragmentation of Small Molecules Following Soft-X-Ray Excitation. *Phys. Rev. Lett.* **50**, 1038–1041 (1983). URL http://link.aps.org/doi/10.1103/PhysRevLett.50.1038.

[55] Aksela, S., Tan, K. H., Aksela, H. & Bancroft, G. M. Si(LVV) Auger and resonance Auger spectra of SiF_4 molecules with the use of synchrotron radiation. *Phys. Rev. A* **33**, 258–263 (1986). URL http://link.aps.org/doi/10.1103/PhysRevA.33.258.

[56] Tarantelli, F. & Cederbaum, L. S. Foreign imaging in Auger spectroscopy: The Si 2p spectrum of silicon tetrafluoride. *Phys. Rev. Lett.* **71**, 649–652 (1993). URL http://link.aps.org/doi/10.1103/PhysRevLett.71.649.

[57] Förstel, M., Mucke, M., Arion, T., Bradshaw, A. M. & Hergenhahn, U. Autoionization Mediated by Electron Transfer. *Phys. Rev. Lett.* **106**, 033402 (2011). URL http://link.aps.org/doi/10.1103/PhysRevLett.106.033402.

[58] Sakai, K. *et al.* Electron-Transfer-Mediated Decay and Interatomic Coulombic Decay from the Triply Ionized States in Argon Dimers. *Phys. Rev. Lett.* **106**, 033401 (2011). URL http://link.aps.org/doi/10.1103/PhysRevLett.106.033401.

[59] Cederbaum, L. S., Zobeley, J. & Tarantelli, F. Giant Intermolecular Decay and Fragmentation of Clusters. *Phys. Rev. Lett.* **79**, 4778–4781 (1997). URL http://link.aps.org/doi/10.1103/PhysRevLett.79.4778.

[60] Marburger, S., Kugeler, O., Hergenhahn, U. & Möller, T. Experimental Evidence for Interatomic Coulombic Decay in Ne Clusters. *Phys. Rev. Lett.* **90**, 203401 (2003). URL http://link.aps.org/doi/10.1103/PhysRevLett.90.203401.

[61] Mucke, M. *et al.* A hitherto unrecognized source of low-energy electrons in water. *Nature Physics* **6**, 143–146 (2010). URL http://www.nature.com/doifinder/10.1038/nphys1500.

[62] Jahnke, T. *et al.* Ultrafast energy transfer between water molecules. *Nature Physics* **6**, 139–142 (2010). URL http://www.nature.com/doifinder/10.1038/nphys1498.

[63] Zobeley, J., Santra, R. & Cederbaum, L. S. Electronic decay in weakly bound heteroclusters: Energy transfer versus electron transfer. *The Journal of Chemical Physics* **115**, 5076 (2001). URL http://link.aip.org/link/JCPSA6/v115/i11/p5076/s1&Agg=doi.

[64] Buth, C., Santra, R. & Cederbaum, L. S. Impact of Interatomic Electronic Decay Processes on Xe 4d Hole Decay in the Xenon Fluorides. *The Journal of*

Chemical Physics **119**, 11 (2003). URL `http://link.aip.org/link/?JCP/119/10575/1`.

[65] Hergenhahn, U. Vibrational structure in inner shell photoionization of molecules. *Journal of Physics B: Atomic, Molecular and Optical Physics* **37**, R89 (2004). URL `http://stacks.iop.org/0953-4075/37/i=12/a=R01`.

[66] Hollander, J. M. & Jolly, W. L. X-ray photoelectron spectroscopy. *Accounts of Chemical Research* **3**, 193–200 (1970). URL `http://pubs.acs.org/doi/abs/10.1021/ar50030a003`.

[67] Campbell, J. L. & Papp, T. Widths of the atomic K–N7 levels. *Atomic Data and Nuclear Data Tables* **77**, 1 – 56 (2001). URL `http://www.sciencedirect.com/science/article/pii/S0092640X00908489`.

[68] Coville, M. & Thomas, T. D. Molecular effects on inner-shell lifetimes: Possible test of the one-center model of Auger decay. *Phys. Rev. A* **43**, 6053–6056 (1991). URL `http://link.aps.org/doi/10.1103/PhysRevA.43.6053`.

[69] Moribayashi, K., Sasaki, A. & Tajima, T. Ultrafast x-ray processes with hollow atoms. *Phys. Rev. A* **58**, 2007–2015 (1998). URL `http://link.aps.org/doi/10.1103/PhysRevA.58.2007`.

[70] Fang, L. *et al.* Double Core-Hole Production in $\mathbf{N}_2$: Beating the Auger Clock. *Phys. Rev. Lett.* **105**, 083005 (2010). URL `http://link.aps.org/doi/10.1103/PhysRevLett.105.083005`.

[71] Salén, P. *et al.* Experimental Verification of the Chemical Sensitivity of Two-Site Double Core-Hole States Formed by an X-Ray Free-Electron Laser. *Phys. Rev. Lett.* **108**, 153003 (2012). URL `http://link.aps.org/doi/10.1103/PhysRevLett.108.153003`.

[72] Jiang, Y. H. *et al.* Ultrafast Extreme Ultraviolet Induced Isomerization of Acetylene Cations. *Phys. Rev. Lett.* **105**, 263002 (2010). URL `http://link.aps.org/doi/10.1103/PhysRevLett.105.263002`.

[73] Carlson, T. A. & White, R. M. Measurement of the Relative Abundances and Recoil-Energy Spectra of Fragment Ions Produced as the Initial Consequences

of X-Ray Interaction with CH_3I, HI, and DI. *The Journal of Chemical Physics* **44**, 4510–4520 (1966). URL http://link.aip.org/link/?JCP/44/4510/1.

[74] Carlson, T. A. & White, R. M. Measurement of the Relative Abundances and Recoil Energy Spectra of Fragment Ions Produced as the Initial Consequences of X-Ray Interaction with C_2H_5I, CH_3CD_2I, and $Pb(CH_3)_4$. *The Journal of Chemical Physics* **48**, 5191–5194 (1968). URL http://link.aip.org/link/?JCP/48/5191/1.

[75] Kanter, E. P. *et al.* Role of excited electronic states in the interactions of fast (MeV) molecular ions with solids and gases. *Phys. Rev. A* **20**, 834–854 (1979). URL http://link.aps.org/doi/10.1103/PhysRevA.20.834.

[76] Hishikawa, A., Iwamae, A., Hoshina, K., Kono, M. & Yamanouchi, K. Mass-resolved two-dimensional momentum imaging of the Coulomb explosion of N_2 and SO_2 in an intense laser field. *Chemical Physics Letters* **282**, 283–291 (1998). URL http://www.sciencedirect.com/science/article/B6TFN-3WF7NPK-D/2/bbd0bdf93d87480c1af4d2c1fae9fa22.

[77] Sanderson, J. H. *et al.* Geometry modifications and alignment of H_2O in an intense femtosecond laser pulse. *Phys. Rev. A* **59**, R2567–R2570 (1999). URL http://link.aps.org/doi/10.1103/PhysRevA.59.R2567.

[78] Stapelfeldt, H., Sakai, H., Constant, E. & Corkum, P. B. Formation and measurement of molecular quantum picostructures. *Phys. Rev. A* **55**, R3319–R3322 (1997). URL http://link.aps.org/doi/10.1103/PhysRevA.55.R3319.

[79] Rudenko, A. *et al.* Real-time observation of vibrational revival in the fastest molecular system. *Chemical Physics* **329**, 193 – 202 (2006). URL http://www.sciencedirect.com/science/article/pii/S0301010406003545.

[80] Ergler, T. *et al.* Spatiotemporal Imaging of Ultrafast Molecular Motion: Collapse and Revival of the D_2^+ Nuclear Wave Packet. *Phys. Rev. Lett.* **97**, 193001 (2006). URL http://link.aps.org/doi/10.1103/PhysRevLett.97.193001.

[81] Légaré, F. *et al.* Laser Coulomb-explosion imaging of small molecules. *Phys. Rev. A* **71**, 013415 (2005). URL http://link.aps.org/doi/10.1103/PhysRevA.71.013415.

[82] Jiang, Y. H. *et al.* Investigating two-photon double ionization of D_2 by XUV-pump–XUV-probe experiments. *Phys. Rev. A* **81**, 051402 (2010). URL `http://link.aps.org/doi/10.1103/PhysRevA.81.051402`.

[83] Magrakvelidze, M. *et al.* Tracing nuclear-wave-packet dynamics in singly and doubly charged states of N_2 and O_2 with XUV-pump–XUV-probe experiments. *Phys. Rev. A* **86**, 013415 (2012). URL `http://link.aps.org/doi/10.1103/PhysRevA.86.013415`.

[84] Rudenko, A. *et al.* Exploring few-photon, few-electron reactions at FLASH: from ion yield and momentum measurements to time-resolved and kinematically complete experiments. *Journal of Physics B: Atomic, Molecular and Optical Physics* **43**, 194004 (2010). URL `http://stacks.iop.org/0953-4075/43/i=19/a=194004`.

[85] Ullrich, J., Rudenko, A. & Moshammer, R. Free-Electron Lasers: New Avenues in Molecular Physics and Photochemistry. *Annual Review of Physical Chemistry* **63**, 635–660 (2012). URL `http://www.annualreviews.org/doi/abs/10.1146/annurev-physchem-032511-143720`.

[86] Erk, B. *et al.* Observation of shells in Coulomb explosions of rare-gas clusters. *Phys. Rev. A* **83**, 043201 (2011). URL `http://link.aps.org/doi/10.1103/PhysRevA.83.043201`.

[87] Dormand, J. R. & Prince, P. J. A family of embedded Runge-Kutta formulae. *Journal of Computational and Applied Mathematics* **6**, 19 – 26 (1980). URL `http://www.sciencedirect.com/science/article/pii/0771050X80900133`.

[88] Galassi, M. *et al. Gnu Scientific Library: Reference Manual* (Network Theory Ltd., 2003). URL `http://www.gnu.org/software/gsl/`.

[89] Hsieh, S. & Eland, J. H. D. Reaction dynamics of three-body dissociations in triatomic molecules from single-photon double ionization studied by a time- and position-sensitive coincidence method. *Journal of Physics B: Atomic, Molecular and Optical Physics* **30**, 4515 (1997). URL `http://stacks.iop.org/0953-4075/30/i=20/a=015`.

[90] Emma, P. *et al.* First lasing and operation of an angstrom-wavelength free-electron laser. *Nature Photonics* **4**, 641–647 (2010). URL `http://www.nature.com/doifinder/10.1038/nphoton.2010.176`.

[91] Ackermann, W. *et al.* Operation of a free-electron laser from the extreme ultraviolet to the water window. *Nature Photonics* **1**, 336–342 (2007). URL `http://dx.doi.org/10.1038/nphoton.2007.76`.

[92] Shintake, T. *et al.* A compact free-electron laser for generating coherent radiation in the extreme ultraviolet region. *Nature Photonics* **2**, 555–559 (2008). URL `http://dx.doi.org/10.1038/nphoton.2008.134`.

[93] Ishikawa, T. *et al.* A compact X-ray free-electron laser emitting in the sub-angstrom region. *Nature Photonics* **6**, 540 – 544 (2012). URL `http://dx.doi.org/10.1038/nphoton.2012.141`.

[94] Geloni, G. *et al.* Coherence properties of the European XFEL. *New Journal of Physics* **12**, 035021 (2010). URL `http://stacks.iop.org/1367-2630/12/i=3/a=035021`.

[95] Madey, J. M. J. Stimulated Emission of Bremsstrahlung in a Periodic Magnetic Field. *Journal of Applied Physics* **42**, 1906 (1971). URL `http://link.aip.org/link/?JAP/42/1906/1&Agg=doi`.

[96] Elias, L. R., Fairbank, W. M., Madey, J. M. J., Schwettman, H. A. & Smith, T. I. Observation of Stimulated Emission of Radiation by Relativistic Electrons in a Spatially Periodic Transverse Magnetic Field. *Phys. Rev. Lett.* **36**, 717–720 (1976). URL `http://link.aps.org/doi/10.1103/PhysRevLett.36.717`.

[97] Milton, S. V. *et al.* Exponential Gain and Saturation of a Self-Amplified Spontaneous Emission Free-Electron Laser. *Science* **292**, 2037–2041 (2001). URL `http://www.sciencemag.org/content/292/5524/2037.abstract`.

[98] Emma, P., Frisch, J. & Krejcik, P. A Transverse RF Deflecting Structure for Bunch Length and Phase Space Diagnostics. *Proceedings 2001 Particle Accelerator Conference* (2001). URL `http://www-ssrl.slac.stanford.edu/lcls/technotes/lcls-tn-00-12.pdf`.

[99] Ding, Y. *et al.* Measurements and simulations of ultralow emittance and ultrashort electron beams in the linac coherent light source. *Physical Review Letters* **102**, 254801 (2009). URL `http://link.aps.org/doi/10.1103/PhysRevLett.102.254801`.

[100] McNeil, B. W. J. & Thompson, N. R. X-ray free-electron lasers. *Nature Photonics* **4**, 814–821 (2010). URL `http://dx.doi.org/10.1038/nphoton.2010.239`.

[101] Kincaid, B. M. A short-period helical wiggler as an improved source of synchrotron radiation. *Journal of Applied Physics* **48**, 2684–2691 (1977). URL `http://link.aip.org/link/?JAP/48/2684/1`.

[102] Khan, S. Free-electron lasers. *Journal of Modern Optics* **55**, 3469 – 3512 (2008). URL `http://www.tandfonline.com/doi/abs/10.1080/09500340802521175`.

[103] Kondratenko, A. M. & Saldin, E. L. Generation of coherent radiation by a relativistic electron beam in an ondulator. *Particle Accelerators* **10**, 207 – 216 (1980).

[104] Saldin, E. L., Schneidmiller, E. A. & Yurkov, M. V. Statistical properties of radiation from VUV and X-ray free electron laser. *Optics Communications* **148**, 383 – 403 (1998). URL `http://www.sciencedirect.com/science/article/pii/S0030401897006706`.

[105] Bonifacio, R., De Salvo, L., Pierini, P., Piovella, N. & Pellegrini, C. Spectrum, temporal structure, and fluctuations in a high-gain free-electron laser starting from noise. *Phys. Rev. Lett.* **73**, 70 – 73 (1994). URL `http://link.aps.org/doi/10.1103/PhysRevLett.73.70`.

[106] Huang, Z. & Kim, K.-J. Review of x-ray free-electron laser theory. *Phys. Rev. ST Accel. Beams* **10**, 034801 (2007). URL `http://link.aps.org/doi/10.1103/PhysRevSTAB.10.034801`.

[107] DiMauro, L. *et al.* First SASE and seeded FEL lasing of the NSLS DUV FEL at 266 and 400 nm. *Nuclear Instruments and Methods in Physics Research Section A: Accelerators, Spectrometers, Detectors and Associated Equipment* **507**, 15

– 18 (2003). URL http://www.sciencedirect.com/science/article/pii/S0168900203008258.

[108] Togashi, T. *et al.* Extreme ultraviolet free electron laser seeded with high-order harmonic of Ti:sapphire laser. *Opt. Express* **19**, 317–324 (2011). URL http://www.opticsexpress.org/abstract.cfm?URI=oe-19-1-317.

[109] Geloni, G., Kocharyan, V. & Saldin, E. A novel self-seeding scheme for hard X-ray FELs. *Journal of Modern Optics* **58**, 1391 – 1403 (2011). URL http://www.tandfonline.com/doi/abs/10.1080/09500340.2011.586473.

[110] Amann, J. *et al.* Demonstration of self-seeding in a hard-X-ray free-electron laser. *Nature Photonics* **6**, 693 – 698 (2012). URL http://dx.doi.org/10.1038/nphoton.2012.180.

[111] Emma, P. *et al.* Femtosecond and Subfemtosecond X-Ray Pulses from a Self-Amplified Spontaneous-Emission–Based Free-Electron Laser. *Phys. Rev. Lett.* **92**, 074801 (2004). URL http://link.aps.org/doi/10.1103/PhysRevLett.92.074801.

[112] Schoenlein, R. W. *et al.* Generation of Femtosecond Pulses of Synchrotron Radiation. *Science* **287**, 2237–2240 (2000). URL http://www.sciencemag.org/content/287/5461/2237.abstract.

[113] Khan, S., Holldack, K., Kachel, T., Mitzner, R. & Quast, T. Femtosecond Undulator Radiation from Sliced Electron Bunches. *Phys. Rev. Lett.* **97**, 074801 (2006). URL http://link.aps.org/doi/10.1103/PhysRevLett.97.074801.

[114] Beaud, P. *et al.* Spatiotemporal Stability of a Femtosecond Hard–X-Ray Undulator Source Studied by Control of Coherent Optical Phonons. *Phys. Rev. Lett.* **99**, 174801 (2007). URL http://link.aps.org/doi/10.1103/PhysRevLett.99.174801.

[115] Seres, J. *et al.* Laser technology: source of coherent kiloelectronvolt X-rays. *Nature* **433**, 596 (2005). URL http://dx.doi.org/10.1038/433596a.

[116] Jiang, Y. H. *et al.* Temporal coherence effects in multiple ionization of N_2 via XUV pump-probe autocorrelation. *Phys. Rev. A* **82**, 041403 (2010). URL http://link.aps.org/doi/10.1103/PhysRevA.82.041403.

[117] Düsterer, S. *et al.* Femtosecond x-ray pulse length characterization at the Linac Coherent Light Source free-electron laser. *New Journal of Physics* **13**, 093024 (2011). URL `http://stacks.iop.org/1367-2630/13/i=9/a=093024`.

[118] Hau-Riege, S. P., Bionta, R. M., Ryutov, D. D. & Krzywinski, J. Measurement of x-ray free-electron-laser pulse energies by photoluminescence in nitrogen gas. *Journal of Applied Physics* **103**, 053306 (2008). URL `http://link.aip.org/link/JAPIAU/v103/i5/p053306/s1&Agg=doi`.

[119] Hau-Riege, S. P. *et al.* Near-Ultraviolet Luminescence of $\mathbf{N}_2$ Irradiated by Short X-Ray Pulses. *Phys. Rev. Lett.* **105**, 043003 (2010). URL `http://link.aps.org/doi/10.1103/PhysRevLett.105.043003`.

[120] Moeller, S. *et al.* Photon beamlines and diagnostics at LCLS. *Nuclear Instruments and Methods in Physics Research Section A: Accelerators, Spectrometers, Detectors and Associated Equipment* **635**, S6 – S11 (2011). URL `http://www.sciencedirect.com/science/article/pii/S0168900210024101`.

[121] Rudek, B. *Multiple Ionization of Heavy Atoms by Intense X-Ray Free-Electron Laser Pulses*. Ph.D. thesis, Ruperto-Carola-University of Heidelberg, Germany (2012). URL `http://www.ub.uni-heidelberg.de/archiv/13340`.

[122] Chalupsky, J. *et al.* Comparing different approaches to characterization of focused X-ray laser beams. *Nuclear Instruments and Methods in Physics Research Section A: Accelerators, Spectrometers, Detectors and Associated Equipment* **631**, 130 – 133 (2011). URL `http://www.sciencedirect.com/science/article/pii/S0168900210027816`.

[123] Loh, N. D. *et al.* Profiling structured beams using injected aerosols. *Proc. SPIE 8504, X-Ray Free-Electron Lasers: Beam Diagnostics, Beamline Instrumentation, and Applications* 850403 (2012). URL `http://proceedings.spiedigitallibrary.org/proceeding.aspx?articleid=1381227`.

[124] Gorkhover, T. *et al.* Nanoplasma Dynamics of Single Large Xenon Clusters Irradiated with Superintense X-Ray Pulses from the Linac Coherent Light Source Free-Electron Laser. *Phys. Rev. Lett.* **108**, 245005 (2012). URL `http://link.aps.org/doi/10.1103/PhysRevLett.108.245005`.

[125] Strüder, L. *et al.* Large-format, high-speed, X-ray pnCCDs combined with electron and ion imaging spectrometers in a multipurpose chamber for experiments at 4th generation light sources. *Nuclear Instruments and Methods in Physics Research Section A: Accelerators, Spectrometers, Detectors and Associated Equipment* **614**, 483–496 (2010). URL `http://linkinghub.elsevier.com/retrieve/pii/S0168900209023900`.

[126] Hau-Riege, S. P. *et al.* Ultrafast Transitions from Solid to Liquid and Plasma States of Graphite Induced by X-Ray Free-Electron Laser Pulses. *Phys. Rev. Lett.* **108**, 217402 (2012). URL `http://link.aps.org/doi/10.1103/PhysRevLett.108.217402`.

[127] Wales, B. *et al.* A coincidence detection algorithm for improving detection rates in coulomb explosion imaging. *Nuclear Instruments and Methods in Physics Research Section A: Accelerators, Spectrometers, Detectors and Associated Equipment* **667**, 11 – 15 (2012). URL `http://www.sciencedirect.com/science/article/pii/S0168900211021528`.

[128] Bergmann, L., Schaefer, C. & Kleinermanns, K. *Lehrbuch der Experimentalphysik 5. Gase, Nanosysteme, Flüssigkeiten*. Bd. 5 (De Gruyter, 2005).

[129] Moshammer, R., Unverzagt, M., Schmitt, W., Ullrich, J. & Schmidt-Böcking, H. A 4π recoil-ion electron momentum analyzer: a high-resolution "microscope" for the investigation of the dynamics of atomic, molecular and nuclear reactions. *Nuclear Instruments and Methods in Physics Research Section B: Beam Interactions with Materials and Atoms* **108**, 425 – 445 (1996). URL `http://www.sciencedirect.com/science/article/pii/0168583X95012591`.

[130] Ullrich, J. *et al.* Recoil-ion and electron momentum spectroscopy: reaction-microscopes. *Reports on Progress in Physics* **66**, 1463–1545 (2003). URL `http://stacks.iop.org/0034-4885/66/i=9/a=203?key=crossref.4f0ed0c11253bbad6096727290d95871`.

[131] Ali, I. *et al.* Multi-hit detector system for complete momentum balance in spectroscopy in molecular fragmentation processes. *Nuclear Instruments and Methods in Physics Research Section B: Beam Interactions with Materials*

and Atoms **149**, 490 – 500 (1999). URL http://www.sciencedirect.com/science/article/pii/S0168583X98009161.

[132] RoentDek Handels GmbH. URL http://www.roentdek.com/.

[133] Foucar, L. *et al.* CASS–CFEL-ASG software suite. *Computer Physics Communications* **183**, 2207 – 2213 (2012). URL http://www.sciencedirect.com/science/article/pii/S0010465512001622.

[134] Abdullah, A. H., El-Shemi, A. M. & Ghoneim, A. A. Yields of multiply charged ions produced from inner-shell ionization in neutral Ne, Ar and Kr atoms. *Radiation Physics and Chemistry* **68**, 697 – 705 (2003). URL http://www.sciencedirect.com/science/article/pii/S0969806X0300433X.

[135] Carlson, T. A., Hunt, W. E. & Krause, M. O. Relative Abundances of Ions Formed as the Result of Inner-Shell Vacancies in Atoms. *Phys. Rev.* **151**, 41–47 (1966). URL http://link.aps.org/doi/10.1103/PhysRev.151.41.

[136] Krause, M. O. & Carlson, T. A. Vacancy Cascade in the Reorganization of Krypton Ionized in an Inner Shell. *Phys. Rev.* **158**, 18–24 (1967). URL http://link.aps.org/doi/10.1103/PhysRev.158.18.

[137] Morishita, Y. *et al.* Formation mechanisms of multi-charged Kr ions through 2p shell photoionization using a coincidence technique. *Journal of Physics B: Atomic, Molecular and Optical Physics* **39**, 1323 (2006). URL http://stacks.iop.org/0953-4075/39/i=6/a=005.

[138] Shigemasa, E. *et al.* Ionic fragmentation of SiH_4 following the K -shell excitation. *Physica Scripta* **41**, 67 (1990). URL http://stacks.iop.org/1402-4896/41/i=1/a=017.

[139] Rudenko, A. *et al.* AMO L172: From Small to Large: Coulomb Explosion Imaging of Molecular Fragmentation and its Implications for Coherent Diffractive Imaging. *LCLS Proposal* (2010).

[140] Golovin, A. V., Cherepkov, N. A. & Kuznetsov, V. V. Photoionization of oriented molecules in a gas phase. *Zeitschrift für Physik D Atoms, Molecules and Clusters* **24**, 371–375 (1992). URL http://dx.doi.org/10.1007/BF01426686. 10.1007/BF01426686.

[141] Rolles, D. *et al.* Molecular-Frame Angular Distributions of Resonant CO:C($1s$) Auger Electrons. *Phys. Rev. Lett.* **101**, 263002 (2008). URL `http://link.aps.org/doi/10.1103/PhysRevLett.101.263002`.

[142] Heiser, F. *et al.* Demonstration of Strong Forward-Backward Asymmetry in the $C1s$ Photoelectron Angular Distribution from Oriented CO Molecules. *Phys. Rev. Lett.* **79**, 2435–2437 (1997). URL `http://link.aps.org/doi/10.1103/PhysRevLett.79.2435`.

[143] Downie, P. & Powis, I. Molecule-Frame Photoelectron Angular Distributions from Oriented CF_3I Molecules. *Phys. Rev. Lett.* **82**, 2864–2867 (1999). URL `http://link.aps.org/doi/10.1103/PhysRevLett.82.2864`.

[144] Fukuzawa, H. *et al.* Site-selective ion pair production via normal Auger decay of free CH_3F molecules studied by electron-ion-ion coincidence spectroscopy. *Chemical Physics Letters* **436**, 51 – 56 (2007). URL `http://www.sciencedirect.com/science/article/pii/S0009261407000619`.

[145] Thomas, C. H. Microwave spectrum, barrier to internal rotation, structure, and dipole moment of methane selenol. *The Journal of Chemical Physics* **59**, 70–76 (1973). URL `http://link.aip.org/link/?JCP/59/70/1`.

[146] Weiner, B. R., Levene, H. B., Valentini, J. J. & Baronavski, A. P. Ultraviolet photodissociation dynamics of H_2S and D_2S. *The Journal of Chemical Physics* **90**, 1403–1414 (1989). URL `http://link.aip.org/link/?JCP/90/1403/1`.

[147] Schorb, S. *et al.* X-ray–optical cross-correlator for gas-phase experiments at the Linac Coherent Light Source free-electron laser. *Applied Physics Letters* **100**, 121107 (2012). URL `http://link.aip.org/link/?APL/100/121107/1`.

[148] Svensson, S. Soft x-ray photoionization of atoms and molecules. *Journal of Physics B: Atomic, Molecular and Optical Physics* **38**, S821 (2005). URL `http://stacks.iop.org/0953-4075/38/i=9/a=024`.

Selbständigkeitserklärung

Erklärung gemäß §8(3b) der Promotionsordnung darüber, dass die Doktorarbeit auf selbständiger Arbeit beruht.

"Ich versichere hiermit, dass ich die vorliegende Arbeit selbstständig verfasst, keine anderen als die angegebenen Hilfsmittel verwendet und sämtliche Stellen, die benutzten Werken im Wortlaut oder dem Sinne nach entnommen sind, mit Quellen- bzw. Herkunftsangaben kenntlich gemacht habe."

Hamburg, November 22, 2012

Benjamin Erk